ISSN 0915-6348

NATIONAL INSTITUTE FOR FUSION SCIENCE

JSPS-CAS Core University Program Seminar
Proceedings of Japan-China Joint Seminar on Atomic and Molecular Processes in Plasma

March 6-11, 2004, Lanzhou, China

F. Koike and D. Chenzhong (Eds.)

(Received - Jan. 24, 2005)

NIFS-PROC-59 Feb. 2005

RESEARCH REPORT
NIFS-PROC Series

TOKI, JAPAN

Proceedings of Japan-China Joint Seminar on Atomic and Molecular Processes in Plasma

March 6 – 11, 2004, Lanzhou, China

Edited by

Fumihiro Koike and Dong Chenzhong

Abstract

As one of the activities of JSPS-CAS Core University Program, Japan-China Joint Seminar on Atomic and Molecular Processes in Plasma was held on March 6 – 11, 2004 in Lanzhou, China. The total number of the officially registered participants was 29, in which 17 from Japan, 10 from China, and 2 from Germany.

In the nuclear fusion plasma, there are quite a variety of atomic processes such as ionization, excitation, radiative recombination, non-radiative recombination (di-electronic recombination, collisional electron transfer), cascade radiation, and cascade Auger decay over the wide range of plasma temperature. The knowledge of such the processes is indispensable for the evaluation and improvement of the plasma properties, which is desirable to be investigated by international collaboration groups. The present Japan-China Joint Seminar constitutes one of such the activities to realize the above stated aim.

Key words:

atomic processes, plasma spectroscopy, excitation, ionization, recombination, charge transfer, X-ray, polarization spectroscopy, atomic database, tokamak, divertor, LHD, molecular processes, atomic structures, radiative recombination, di-electronic recombination

Preface

As one of the activities of the Core University Program (CUP) entitled “atomic and molecular processes in plasma”, a seminar “China-Japan Joint Seminar on Atomic and Molecular Processes in Plasma” was held from the 6’th to 10’th March 2004 at Northwest Normal University, Lanzhou, China. This is the seminar that was organized under the CUP agreement between Chinese Academy of Science (CAS) and Japan Society for the Promotion of Science (JSPS), which was initiated in 2000 and will last 10 years.

During the past four years, the researchers from both Japan and China carried out a number of significant studies in atomic and molecular processes in relation to the fusion plasma. The proposal of the present joint seminar has placed its intention not only on the presentations of the collaborative studies, but also on offering an opportunity for the wide range of researchers from both countries to be acquainted with each other, who would have made an extensive exchange of information about the recent progress of the research activities, and also would have made an extensive discussion about the plan of the future collaborations.

In the present seminar, the total number of 28 oral talks was presented by experts from Japan, China and Germany. The total number of the audience was about 80; the seminar had attracted the attendance of about 50 people from inside the Northwest Normal University and its neighboring institutions. In the opening remarks, firstly, Professor Takako Kato, who is the chairperson of the seminar, the coordinator of CUP, and the director of the data and planning center at National Institute for Fusion Science, gave a brief introduction to CUP. She is followed by Professor Hualin Deng, vice president of Northwest Normal University, who presented a warm address. Professor Jiaming Li, academician of CAS, sent a cordial greeting to the seminar on behalf of the Chinese Society of Atomic and Molecular Physics.

The seminar was in always a friendly and active atmosphere. As of the intermission of the seminar, participants visited the Museum of Northwest Normal University. They enjoyed many kinds of tasty Chinese foods and also a famous dance drama “The Silk Road dotted with flower”. On the last day of the seminar, many of the participants visited Ta'er Monastery in Xining city. During the seminar, the participants exchanged their new research results, discussed about the outlook for new research fields. They tried to promote further developments in mutual collaborations between the countries and the experts. It has given an atmosphere that a subsequent meeting should be desirable to be planned in the near future.

The present issue of the proceedings has collected 24 oral talks that are presented in the seminar. They covers the spectroscopic properties of atoms and ions in the plasma, the collisions of electrons or ions with atoms or ions in the plasma, the analysis and diagnostics of the confinement fusion plasma, the atomic data compilations and the database constructions, and, further, the molecular processes in the confinement fusion plasma. The present issue also includes the scientific program of the seminar, the group photo as well as the list of participants.

On behalf of the organizing committee, we would like to express our sincerest thanks to all the participants who made active contributions not only in the formal presentations but also in the fruitful discussions. We would like to acknowledge everybody who devoted very hard work for preparing the seminar. We also would like to express our special thanks to Professor Takako Kato and Professor Jianming Li; it was beyond our competence to prepare a nice seminar without their help.

Finally, we would like to acknowledge the administrative as well as the financial supports from the Northwest Normal University and the National Institute for Fusion Science.

Chenzhong Dong
Local Chairperson,
Northwest Normal University, Lanzhou, China

Fumihiro Koike
Organizing Committee,
Kitasato University

Contents

Talks

OF MULTI-CHARGED IONS

Hajime Tanuma

Elastic and inelastic processes in $H^+ + CH_2$ collisions below the 1.5 keV regime

Hiroya Suno, Sachchida N. Rai, Heinz-Peter Liebermann, Robert J. Buenker,
Mineo Kimura, R.K. Janev

Recent Progress of Atomic and Molecular Database in IAPCM

Jun Yan

PLASMA POLARIZATION SPECTROSCOPY

Anisotropic electron velocity distribution in an ECR helium plasma

Atsushi Iwamae and Takashi Fujimoto

Improved density functional calculations for atoms, molecules and surfaces

B. Fricke, J. Anton, S. Fritzsche, C. Sarpe-Tudoran

ELECTRONIC STRUCTURE OF ATOMS IN LASER PLASMA:
THE DEBYE SHIELDING MODEL

Tokuei Sako, Hiroshi Okutsu, Kaoru Yamanouchi

Superexcited states studied by angle-resolved electron energy loss spectroscopy

Zhi-Ping Zhong, Jian-Min Sun, Lan-Lan Fan, Lin-Fan Zhu,
Xiao-Jing Liu, Zhen-Sheng Yuan, Ke-Zun Xu

(e,2e) ionization-excitation experiment with fixed-in-space H_2 molecules

M. Takahashi, N. Watanabe, Y. Khajuria, Y. Udagawa, and J.H.D. Eland

ELECRON AND MOLECULAR ION COLLISIONS RELEVANT
TO DIVERTOR PLASMA

H. Takagi

Calculations of ATI and HHG spectrum of one-dimensional atom in the intense laser field

Xiao-xin Zhou, Song-feng Zhao

MULTIPLE IONIZATION DYNAMICS OF MOLECULES IN INTENSE LASER FIELDS

Atsushi Ichimura and Tomoko Ohyama-Yamaguchi

GEOMETRY EFFECTS ON THE (e,2e) CROSS SECTION OF IONIC TARGETS

Y. Khajuria

THE MOMENTUM TRANSFER DEPENDENCE OF DOUBLE
EXCITATIONS OF HELIUM

Lin-Fan Zhu, Xiao-Jing Liu, Zhen-Sheng Yuan, and Ke-Zun Xu

Abstracts:

Dielectronic recombination in Highly charged ion-electron collision

X. Ma, P. Mokler

Atomic Processes in Ultra-Short Pulse Laser Interaction

Richard M. More, H. Yoneda, H. Morikami

Generalized oscillator strengths of nitric oxide for the valence shell excitations

Yasuhiro Sakai

Agenda

Participants List

China-Japan joint Symposium on AMPP　March 6-11, 2004, Lanzhou, China

中日等离子体中的原子分子过程研讨会　中国 兰州　2004. 3. 6-11

RELATIVISTIC ATOMIC CALCULATIONS FOR MULTIPLE AND HIGHLY–CHARGED IONS

S. Fritzsche
Institut für Physik, Universität Kassel, D–34132 Kassel, Germany,
s.fritzsche@physik.uni-kassel.de

The need for accurate atomic data can hardly be overestimated as they are required in an increasing number of research areas. Today, reliable predictions about the properties and the level structures of free atoms and ions are requested not only in astro and plasma physics (the two traditional fields for applying atomic structure theory) but also in a variety of other, only recently emerging research programs such as the laser–induced fusion program, the search for efficient x–ray laser schemes, or the generation of nanostructures. In addition, accurate structure calculations are among the basic requirements if a better understanding of the *fundamental* interactions in nature and of the role of *correlations* in quantum many–particle systems is to be achieved.

For a long time, atomic *ab–initio* theory has therefore aimed for providing fast and reliable predictions on the energies and properties of atoms. Till today, however, this goal still remains much as a 'challenge' owing to the complexity of most atoms and ions and because of the large variety of the required data. Apart from those systems with just a very few electrons (as, for instance, the hydrogen– and helium–like ions), in fact, helpful spectroscopic predictions on the behaviour of of multiple charged ions are often not so easily feasible. The main difficulties in describing complex systems usually arise from their shell structure and the need to properly describe the *relativistic motion* of the electrons for all medium and heavy systems, in particular, if inner–shell electrons become involved in the atomic processes.

For these reasons, a significant progress in providing accurate data cannot be expected without that new theoretical techniques and computer programs are developed. Although the steady increase of the computer ressources during the last few decades has facilitated many electronic structure calculations, equally important — for sure — is the development of (computational) tools which are able to support both, accurate (and systematically improveable) computations as well as the *mass production* of data as often required in fusion research and at many places elsewhere. The request for improved (atomic) codes becomes particularly crucial if — beside of a single open valence shell — one or several inner–shell vacancies occur. For such open–shell structures, the multiconfiguration Hartree–(Dirac–)Fock (MCDF) model [1] has been found helpful to treat a rather wide range of applications. Based on the (many–electron) Dirac Hamiltonian, this computational model allows to incorporate the dominant effects of relativity and correlations within the same framework. For atomic transitions, moreover, it enables one to include the *relaxation* of the electron density. But although several programs are now available for providing approximate (bound–state) wave functions and energies in this model [2, 3], much less attention so far has been paid to the applications of these wave functions for calculating atomic transition, capture, or ionization properties.

To fill this *gap* in the computation of (relativistic atomic) transition and ionization properties for open–shell atoms and ions, we have developed — and lately re–designed — the Ratip package [4, 5] during the last decade. This program, which utilizes the wave functions from the Grasp92 code [2], now supports accurate computations for a variety of atomic properties, including the radiative excitation and decay of atoms or atomic processes with one electron in the continuum. In this contribution, therefore, I shall briefly summarize its present capabilities and the recent improvements on the code. Below, moreover, I mention also a few applications where Ratip were found helpful in the interpretation and the analysis of experiments. Figure 1 displays an overview about the Ratip package as whole. As seen from this figure, it is divided into several components, which have been either published before or for which a long 'write–up' will be prepared in the future. Further details about Ratip's recent (and potential future) development has been given in Ref. [5].

At present, Ratip supports computations on quite a number of different atomic properties including:

(i) the set–up and diagonalization of large Hamiltonian matrices [6],

(ii) the derivation of the LSJ spectroscopic notations of atomic levels as obtained from relativistic computations in $jj-$coupling [7],

(iii) the computation of Einstein coefficients, transition probabilities and (radiative) lifetimes, taking into account the rearragment of the electron density [8],

(iv) the calculation of Auger rates and angular distributions including the spin–polarization of the emitted electrons,

(v) studies on the photoionization and the radiative capture of electrons,

(vi) the computation of reduced coefficients, matrix elements [9] and angular coefficients for non–scalar one–particle and scalar two–particle operators [10],

(vii) the transformation of symmetry–adapted functions from Grasp-92 into a determinant basis [11], as well as

(viii) a toolbox to facilitate a number of small but frequently occuring tasks [12].

Further components, which are currently under development, concern (ix) the study of parity and time invariance violating interactions, (x) the computation of electron–impact excitation cross sections, (xi) studies for plasma screening effects on the level structures and the properties of multiple charged ions, and (xii) the generation of one–particle Green's functions. Most of these components have been developed in the past because of specific user requirements and due to the intention for providing tools,

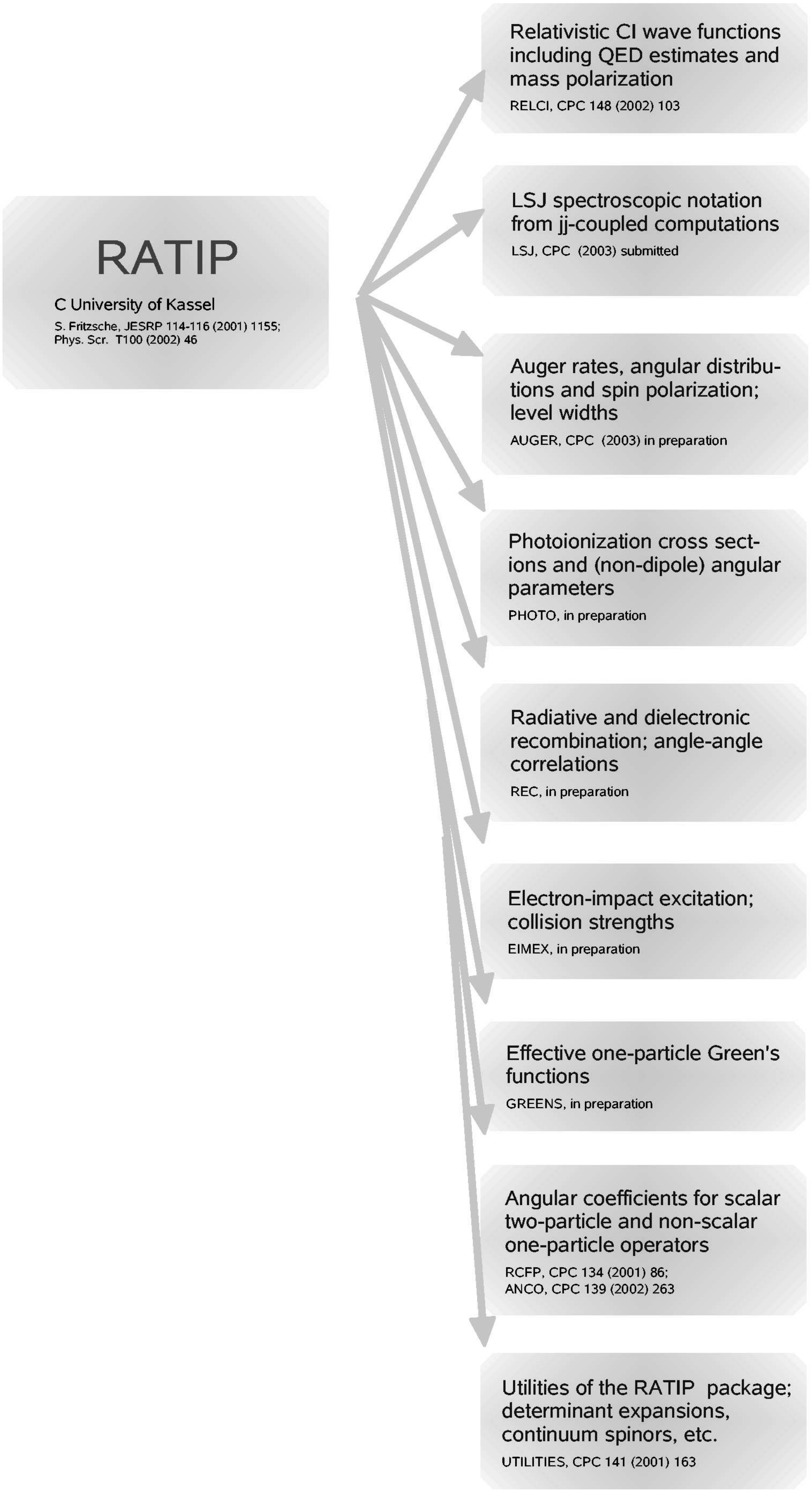

Figure 1: Main structure of the Ratip package which is divided into several programs.

which may support a broad range of applications as well as the study of rather different properties within the same framework.

As said above, RATIP has shown its capabilities in rather a large number of applications. For the sake of brevity, of course, here I can mention only a few important examples where RATIP was found helpful in the analysis and interpretation of experiment. By using the AUGER component, for instance, we were able to explain the *coherence transfer* through the photon excitation and subsequent Auger cascade in resonantly–excited noble gases [13, 14]. Further applications of the program concerned, in addition, studies on the:

- ❑ ultraviolet and EUV line spectra from multiple–charged ions,
- ❑ angular distribution and spin–polarization of emitted electrons [15],
- ❑ level structures of heavy and super–heavy elements [16],
- ❑ interpretation of photo–absorption spectra [17],
- ❑ two–photon ionization of atoms and ions [18],
- ❑ diagnostics of plasmas at tokamaks [19],
- ❑ interpretation of astro–physical data, as well as
- ❑ on the electron capture into highly–charged ions [20].

Concerning the use of systematically enlarged wave functions, the *gros* of experience has been gained so far for transition probability calculations in the optical and ultra–violet range. In particular for computations on multiple and highly–charged ions, it was found as a rule of thumb that *two additional layers of correlation orbitals* are typically sufficient in order to obtain accurate transition probabilities for most of the lines. Note, however, that this (semi–empirical) rule cannot always be fulfilled, in particular if open $d-$ and $f-$shells are involved in the computations.

Not much need to be said here about the future developement of RATIP. Our main concern now pertains to a long life–cycle of the code and to an object–oriented design within the framework of Fortran 90/95. This *up–to–date* language allows to implement programs which are very flexible with respect to the size of the individual investigation to be made. — Overall , the RATIP package has been designed as an independent and open environment whose main components can be obtained by the user on request. Usually, the program is provided as a tar–file from which the `ratip` root directory is generated. This `root` directory presently includes about 25 modules, a set of main programs for the various components, makefiles as well as a number of test suites. In general, a main program like `xcesd.f` or `xutilities.f` is available for each component and provides — along with the *use*d modules — access to the full source code. To distinguish the main programs and executables from other files of the package, they now all start with the prefix `x`.

The file structure of the `ratip` root directory has been set–up with the ulterior motive to facilitate the extension of the package by additional components. In fact, this can easily be done by appending modules, (main) programmes, and corresponding makefiles. For this reason, the code can be further developed almost independently of its maintenance both, on the users' and the developers' side. For the future, still a large number of additional features seems to be *desireable* for RATIP; however, since these components cannot be developed all by ourselves, support by coworkers or even independent developments are very welcome.

The variety of properties, which can be investigated by means of this package, makes RATIP attractive to a rather broad user community. Owing to its particular design in supporting systematically enlarged computations, RATIP may be found useful for the conception and interpretation of new experiments as well as for analyzing trends along isoelectronic sequences. For the on–going fusion research program, in particular, RATIP might help provide data as needed for the diagnostics or the optimization of the plasma parameters. Therefore, suggestions for improving the code are always welcome.

[1] Grant, I. P., in "Methods in Computational Chemistry", Vol. 2 (ed. S. Wilson, Plenum Press, New York, 1988) p. 1.

[2] Parpia, F. A., Froese Fischer, C. and Grant, I. P., Compt. Phys. Commun. 94, 249 (1996).

[3] Indelicato, P., private communication (2002).

[4] Fritzsche, S., J. Electr. Spec. Rel. Phenom. 114–116, 1155 (2001).

[5] Fritzsche, S., Phys. Scr. T100, 37 (2002).

[6] Fritzsche, S., Froese Fischer C. and Gaigalas, G., Compt. Phys. Commun. 148, 103 (2002).

[7] Gaigalas, G., Zalandauskas, T. and Fritzsche, S., Compt. Phys. Commun. 157, 239 (2004).

[8] Fritzsche, S., Froese Fischer, C. and Dong, C. Z., Comput. Phys. Commun. 124 , 342 (2000).

[9] Gaigalas, G. and Fritzsche, S., Comput. Phys. Commun. 134, 86 (2001).

[10] Gaigalas, G., Fritzsche, S. and Grant, I. P., Comput. Phys. Commun. 139, 263 (2001).

[11] Fritzsche, S. and Anton J., Comput. Phys. Commun. 124, 354 (2000).

[12] Fritzsche, S., Compt. Phys. Commun. 141, 163 (2001).

[13] Shimizu, Y. et al., J. Phys. B33, L685 (2000); Ueda, K. et al., J. Phys. B34, 107 (2001).

[14] Kitajima, M. et al, J. Phys. B34, 3829 (2001).

[15] Ueda, K. et al., Phys. Rev. Lett. 90, 153005 (2003).

[16] Sewtz. M. et al., Phys. Rev. Lett. 90, 163002 (2003).

[17] Koide, M. et al., J. Phys. Soc. Jap. 71, 1676 (2002); **71**, 2681 (2002);

[18] Koval, P., Fritzsche, S., Surzhykov, A., J. Phys. B37, 375 (2004).

[19] Marschuk, O. et al., J. Phys. B37, 1951 (2004).

[20] Surzhykov, A. et al., Phys. Rev. Lett. 88, 153001 (2002).

Energy-crossings and their effects on the spectra of the neon-like ions

C. Z. Dong[a,b] [1], **L. Y. Xie**[a] , **J. Jun**[a]

[a] Department of Physics, Northwest Normal University, Lanzhou 730070, China.
[b] National Laboratory of Heavy–Ion Accelerator of Lanzhou, Lanzhou 730000, China.

Abstract

Excitation energies, transition wavelengths and probabilities of the $2p^6$, $2p^5\,3l$, $2s\,2p^6\,3l$ $(l = 0, 1, 2)$ states along the Ne-like isoelectronic sequence from $Z = 21 - 92$ have been calculated by using the Multi-configuration Dirac-Fock package GRASP92 and a newly developing radiative transition program REOS99. In the calculations, the correlation and relaxation effects are included systematically. Based on the calculations, all possible energy crossings among the level groups with the same parity and total angle momentum have been presented. It is found that there are strong configuration interactions in some particular Z regions with energy-crossings, and which can cause the related transition probabilities change dramatically.

1 Introduction

The energy structures and spectra of the neon-like ions have been a subject of interesting investigations in theory, experiment and application. During the past years, many significative investigations have been carried out [1−12]. In theory, the neon-like ions are a multielectron system with a closed shell structure. It is a very good example to understand the contributions from relativistic, electron correlation, relaxation and quantum electrodynamic (QED) effects in accurate study on energy structures and transition properties. Systematic study of neon-like ions has become a candidate for testing various aspects of atomic structure theory. For example, Z-expansion method, model potential method, configuration-interaction method, multiconfiguration Hartree-Fock method, multiconfiguration Dirac-Fock (MCDF), and relativistic many-body perturbation theory (MBPT) have been used to produce lots of energies and transition probabilities data of many neon-like ions in these years [1−8]; In experiment, the neon-like charge state is relatively stable. It is often the dominant ionization state over a wide range of plasma temperature. The neon-like ions of medium and high Z are often present in a variety of high-temperature plasma sources, such as tokamak, laser-produced plasmas, gas-puff Z-pinch, solar atmosphere, EBIT and so on. As a result, the spectra of neon-like ions is the most easily observed lines [9−12]; In application,the properties of the neon-like ions suggest their use for diagnostic purposes. In tokamak, for example, the neon-like ions are employed to study transport and confinement of high-Z impurity ions. Also the spectra from the neon-like systems may provide diagnostic information on plasma electron temperature, electron density, charge-state

---

[1] email: dongcz@nwnu.edu.cn, Fax: +869317971277

abundances, and ion temperatures. In addition, it is also very important for understanding the energy levels and the excitation mechanisms of X-ray laser [10].

In the present work, systematic calculations on the 37 low-lying energy levels of the $2s^2\,2p^5\,3l$, $2s\,2p^6\,3l\,(l = 0, 1, 2)$ and $2s^2\,2p^6$ configurations and the E1 transition probabilities among those levels are carried out for the neon-like ions in the range of $Z = 21 - 92$. In the calculations, the effects of relativistic, relaxation and correlation have been considered by using the multiconfiguration Dirac-Fock package GRASP92[13] and a newly developing radiative transition program REOS99[14]. In order to describe the accuracy of the present calculations, some data of the excited energies and E1 transition probabilities are chosen in low Z (Z=36), middle Z (Z=60), and high Z (Z=92) respectively as comparison with the available experiments and calculations. From the calculations, a systematic study on Z-dependence of the energies and transition probabilities along the whole sequence is carried out. Of course, in this paper, more attention is paid on the energy crossings and their effects on transition probabilities.

2 Theoretical method and computational procedure

In this study, wave functions have been generated by the widely used atomic structure package GRASP92[13] on the basis of the multiconfiguration Dirac-Fock (MCDF). In this method, an atomic state is approximated by a linear combination of configuration state functions (CSFs) of the same symmetry

$$|\psi_\alpha\,(PJM)\rangle \;\; = \;\; \sum_{r=1}^{n_c} c_r(\alpha)\,|\gamma_r PJM\rangle, \tag{1}$$

where n_c is the number of CSF and $c_r(\alpha)$ denotes the representation of the atomic state in this basis. In standard calculation, the CSF are antisymmetrized products of a common set of orthonormal orbitals which are optimized on the basis of the Dirac-Coulomb Hamiltonian. Further relativistic contributions to the representation $c_r(\alpha)$ of the atomic states du to (transverse) Breit interactions were added by diagonalizing the Dirac-Coulomb-Breit Hamiltonian Matrix. The dominant quantum electrodynamic (QED) contributions to the transition energies have also been included in the computations as a perturbation.

To calculate the excited energies belonging to the $2p^6$, $2p^5\,3l$, $2s\,2p^6\,3l\,(l = 0, 1, 2)$ configurations and the transition wavelengths and probabilities among these levels, we used the GRASP92 program package developed by Grant and co-workers[13]. A set of subshell wave functions for the ground configuration $1s^2\,2s^2\,2p^6$, and that for 36 excited configurations $2l^{-1}\,3l'\,(l = 0, 1; l' = 0, 1, 2)$ (representing that of the $2l$ core-subshell electrons is excited to the $3l'$ subshell) were optimized through self-consistent field (SCF) calculations in the (extented) optimal level model of the GRASP92 package [13]. In order to consider systematically the influence of electron correlations in the calculations, the configuration interaction from virtual excitations of electrons from the spectroscopically occupied shells into the unoccupied (sub–) shells are taken into account by using the active space method. Typically, different *classes* of excitations are considered for different (layers of) shells. In the present computations, all virtual single (S) and double (D) excitations from the $2s, 2p$, and $3l$ shells into the (unoccupied) $3l$ shells as well as $4l$ shells are included. It is showed that the effects of those electron correlations are very important to the accuracy calculations of the transition wavelengths and probabilities in neon-like ions, especially that is even more for the lower Z ions[1]. The

3 Comparison with available results

In the present work, the energies of the 37 low-lying levels of the $2s^2\,2p^5\,3l$, $2s\,2p^6\,3l\,(l = 0, 1, 2)$ and $2s^2\,2p^6$ configurations and the E1 transition probabilities among those levels are calculated for the neon-like ions in the range of $Z = 21 - 92$. In order to illustrate the accuracy of the present calculations, a comparison with available results is given in Table 1 and Table 2 respectively for excited energies and transition probabilities for three selected ions with Z=36, Z=60 and Z=92.

Table 1. The excited energies (a.u.) of the states $2l3l'$ with $J^P = 1^-$ in ions Kr^{26+}, Nd^{50+}, and U^{82+}

	$2p_{3/2}^{-1}3s_{1/2}$ ($J^P = 2^-$)	$2p_{3/2}^{-1}3s_{1/2}$ ($J^P = 1^-$)	$2p_{1/2}^{-1}3s_{1/2}$ ($J^P = 0^-$)	$2p_{1/2}^{-1}3s_{1/2}$ ($J^P = 1^-$)	$2p_{3/2}^{-1}3d_{3/2}$ ($J^P = 1^-$)	$2p_{3/2}^{-1}3d_{5/2}$ ($J^P = 1^-$)	$2p_{1/2}^{-1}3d_{3/2}$ ($J^P = 1^-$)
Kr^{26+} (Z=36)							
This work	60.5692	60.6858	62.5881	62.6474	65.4389	66.2286	68.0269
Ref.[2]	60.5996	60.7146	62.6243	62.6818	65.4554	66.2256	68.0282
Ref.[4]	60.6039	60.7186	62.6285	62.6860	65.4551	66.2337	68.0330
Exp [4]	60.6020	60.7200	62.6280	62.6860	65.4720	66.2450	68.0660
Nd^{50+} (Z=60)							
This work	194.9528	195.1855	214.5768	214.6993	209.0095	211.5133	229.3980
Ref.[2]	195.0363	195.2675	214.6947	214.8141	208.9688	211.5009	229.3971
Ref.[4]	195.0447	195.2755	214.7029	214.8249	208.9978	211.4833	229.4005
Exp [4]	195.0570	195.2910		214.8610		211.500	
U^{82+} (Z=92)							
This work	472.1291	472.5659	615.6277	615.7452	528.9562	539.5601	673.4370
Ref.[2]	472.4793	472.9120	616.1176	616.2311	528.6030	539.2600	673.1913
Ref.[4]	472.6117	473.0437	616.1665	616.2809	528.8182	539.3926	673.3128

In Table 1, the present calculated and the available experimental and theoretical excited energies for the seven levels with $J^P = 1^-$ are listed. It can be seen from the table that the present results are in close agreement with experimental measurements and the other theoretical calculations, and the discrepancy among these results is generally less than 0.07%.

In Table 2, the calculated E1 transition probabilities from the excited states $2l3l'$ with $J^P = 1^-$ to the ground state $2p^6\,{}^1S_0$ are given for the three selected ions. Also some previous theoretical values are presented as comparison. It is found that the present calculations are very close to the results of the MBPT calculations by Safronova *et al.*[2] both in low Z , middle Z , and high Z ions. But there are also some very big differences between the present MCDF results and the MBPT calculations of Ivanova *et al.*[3] for some transitions in some ions, such as the transitions $2p_{1/2}^{-1}3s_{1/2}(1)-\ 2p^6\,{}^1S_0$ in Z=60 and $2p_{3/2}^{-1}3d_{3/2}(1)-\ 2p^6\,{}^1S_0$ in Z=92. We hope such big differences among the different calculations can be tested by experiment further.

Table 2. E1 transition probabilities (s^{-1}) from the excited states $2l3l'$ with $J^P=1^-$ to the ground state in ions Kr^{26+}, Nd^{50+}, and U^{82+} ($a[b]=a\times 10^b$)

Upper levels	$2p_{3/2}^{-1}3s_{1/2}$ ($J^P=1^-$)	$2p_{1/2}^{-1}3s_{1/2}$ ($J^P=1^-$)	$2p_{3/2}^{-1}3d_{3/2}$ ($J^P=1^-$)	$2p_{3/2}^{-1}3d_{5/2}$ ($J^P=1^-$)	$2p_{1/2}^{-1}3d_{3/2}$ ($J^P=1^-$)	$2s_{1/2}^{-1}3p_{1/2}$ ($J^P=1^-$)	$2s_{1/2}^{-1}3p_{3/2}$ ($J^P=1^-$)
Kr^{26+} (Z=36)							
This work	5.31[12]	3.57[12]	2.72[11]	7.06[13]	9.16[13]	4.90[12]	1.68[13]
Ref.[2]	5.34[12]	3.58[12]	2.56[11]	7.15[13]	8.98[13]	4.93[12]	1.66[13]
Ref.[8]	5.38[12]	3.91[12]	1.79[11]	6.55[13]	1.03[14]		
Nd^{50+} (Z=60)							
This work	5.66[13]	3.73[12]	8.35[12]	1.09[15]	7.71[14]	5.65[13]	1.82[14]
Ref.[2]	5.65[13]	3.96[12]	8.62[12]	1.09[15]	7.67[14]	5.40[13]	1.82[14]
Ref.[3]	5.5[13]	9.9[13]	2.4[12]	1.1[15]	8.0[14]	4.9[13]	1.8[14]
U^{82+} (Z=92)							
This work	4.70[14]	1.16[14]	4.10[14]	6.98[15]	4.56[15]	1.28[15]	9.62[14]
Ref.[2]	4.70[14]	1.20[14]	4.07[14]	6.89[15]	4.42[15]	1.27[15]	9.77[14]
Ref.[3]	4.7[14]	1.0[14]	4.0[13]	7.2[15]	4.6[15]	1.2[15]	9.5[14]

4 Energy-crossings and wave function mixing

Based on the MCDF calculations on the excited energies of the neon-like ions in the range of Z=21-92, the Z- dependence of these energy levels is studied systematically. It is found that there are seven pairs of the levels with the same parity and J which cross each other in some particular Z region. Some of them, for example level $2p_{1/2}^{-1}3s_{1/2}(1)$, even cross with two levels $2p_{3/2}^{-1}3d_{3/2}(1)$ and $2p_{3/2}^{-1}3d_{5/2}(1)$ at $Z\sim 51$ and $Z\sim 55$, respectively. The details of such crossings are given in Table 3. As we can see from the table, the situations of the crossings in the $J^P=1^-$ level group and in the $J^P=2^-$ level group are in agreement with the previous theories [2,3] and experiments [9], but the three crossings from the levels with $J^P=0^+$,$J^P=1^+$ and $J^P=0^-$ have not been studied before, and expected to be tested in the future.

Table 3. Energy-crossings along the neon-like sequence

J^P	**Crossing levels**	**Z-regions**	**Previous work**
0^+	$2p_{1/2}^{-1}3p_{1/2}(0)$, $2p_{3/2}^{-1}3p_{3/2}(0)$	$Z\sim 23$	
1^+	$2s_{1/2}^{-1}3s_{1/2}(1)$, $2p_{1/2}^{-1}3p_{3/2}(1)$	$Z\sim 73$	
0^-	$2p_{3/2}^{-1}3d_{3/2}(0)$, $2p_{1/2}^{-1}3s_{1/2}(0)$	$Z\sim 51$	
1^-	$2p_{3/2}^{-1}3d_{3/2}(1)$, $2p_{1/2}^{-1}3s_{1/2}(1)$	$Z\sim 51$	Ref.[9]
	$2p_{3/2}^{-1}3d_{5/2}(1)$, $2p_{1/2}^{-1}3s_{1/2}(1)$	$Z\sim 55$	Ref.[2,3,9]
	$2s_{1/2}^{-1}3p_{1/2}(1)$, $2p_{1/2}^{-1}3d_{3/2}(1)$	$Z\sim 70$	Ref.[2]
2^-	$2p_{3/2}^{-1}3d_{3/2}(2)$, $2p_{3/2}^{-1}3d_{5/2}(2)$	$Z\sim 37$	Ref.[2,5]

Usually, such level crossings can cause very strong configuration interactions among the crossing levels, and finally result in a serious mixing of the corresponding wave functions. As an example, here several main wave function components of the $2p_{1/2}^{-1}3s_{1/2}(1)$ level as function of Z is showed in Fig.1. It can be seen from the figure, in the main wave function components, the contribution from the $2p_{3/2}^{-1}3d_{3/2}(1)$ arrives by 29% at $Z \sim 51$, and the contribution from the $2p_{3/2}^{-1}3d_{5/2}(1)$ arrives by 40% at $Z \sim 55$. As we will see below, these mixing will also cause a series serious changes of the corresponding transition probabilities.

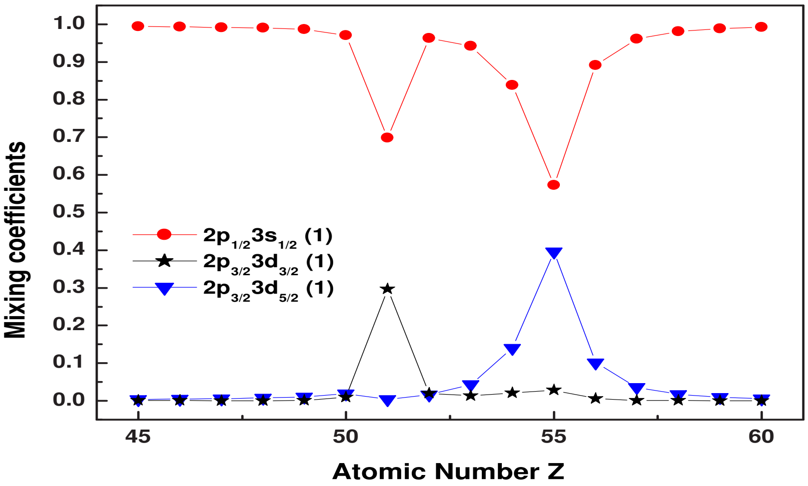

Fig 1. Main wave function components of the $2p_{1/2}^{-1}3s_{1/2}(1)$ level as a function of Z

5 Effects of energy crossings on transition probabilities

From the calculated E1 transition probabilities among all the 37 low-lying levels, the Z-dependence of the transition probabilities is also studied systematically along the sequence. It is found that the Z-dependence features become very irregular at some particular Z regions where existing energy crossings: some of them are enhanced, and the others are weaken; at the same time, as a direct result of strong configuration interactions caused due to the energy crossings, some of so-called two-electron and one-photon transitions (TEOP) become also very strong in some neon-like ions. In order to illustrate such complicated features, two typical examples are shown below.

In Fig.2, the trends of transition probabilities as function of Z for the five transitions from $2p^{-1}3s$ and $2p^{-1}3d$ excited states to the $2p_{3/2}^{-1}3p_{1/2}(1)$ state, in which there are very strong configuration interactions among the upper levels (see Table.3 and Fig.1). We can see from the figure, the transition probabilities are extremely sensitive to the configuration mixing. As a result, once one transition is diminished due to decrease of the corresponding main wave function component, the other one is always increased accordingly. For example, the two strongest transition peaks of the $2p_{1/2}^{-1}3s_{1/2}(1)$ - $2p_{3/2}^{-1}3p_{1/2}(1)$ at Z=51 and 55 are caused due to the decreases of the transition $2p_{3/2}^{-1}3d_{3/2}(1)$ - $2p_{3/2}^{-1}3p_{1/2}(1)$ at Z=51 and $2p_{3/2}^{-1}3d_{5/2}(1)$ - $2p_{3/2}^{-1}3p_{1/2}(1)$ at Z=55, respectively.

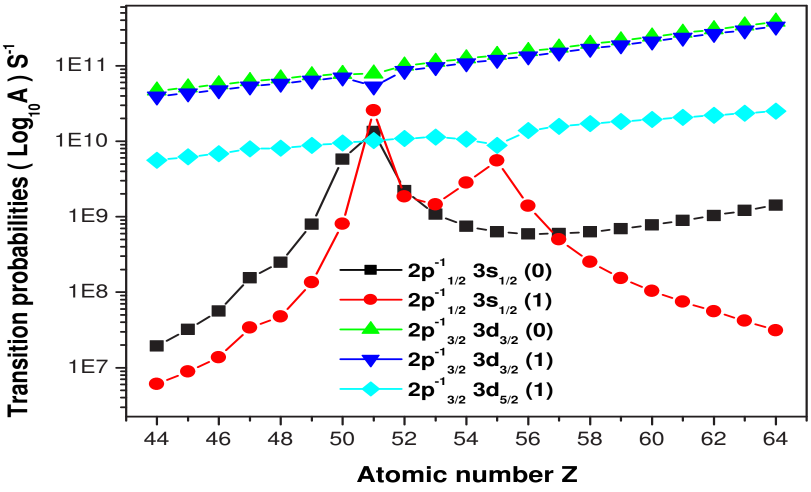

Fig.2 E1 transition probabilities (s^{-1}) from the upper levels with energy-crossings to the $2p^{-1}_{3/2}3p_{1/2}(1)$ as functions of Z.

In Fig.3, the E1 transition probabilities from two upper levels $2s^{-1}_{1/2}3d_{3/2}(1)$ and $2s^{-1}_{1/2}3d_{3/2}(2)$ to the lower level $2p^{-1}_{1/2}3s_{1/2}(1)$ are showed as function of Z. We can see that there are two maximum peaks around Z=51 and 55. As we know, these transitions are usually unallowed. But due to the strong configuration interactions between the $2p^{-1}_{1/2}3s_{1/2}(1)$ and $2p^{-1}_{3/2}3d_{3/2}(1)$ at Z=51 and between the $2p^{-1}_{1/2}3s_{1/2}(1)$ and $2p^{-1}_{3/2}3d_{5/2}(1)$ at Z=55, the transition lower level $2p^{-1}_{1/2}3s_{1/2}(1)$ include some important components of the $2p^{-1}3d(1)$ states in these ions. As a result, these transitions become not only possible, but also very strong, even can comparable with the strong E1 transitions. This is so called two-electron one-photo (TEOP) transition. We hope these transitions from the neon-like ions will contribute to well understand the TEOP transition, and can be tested in the future.

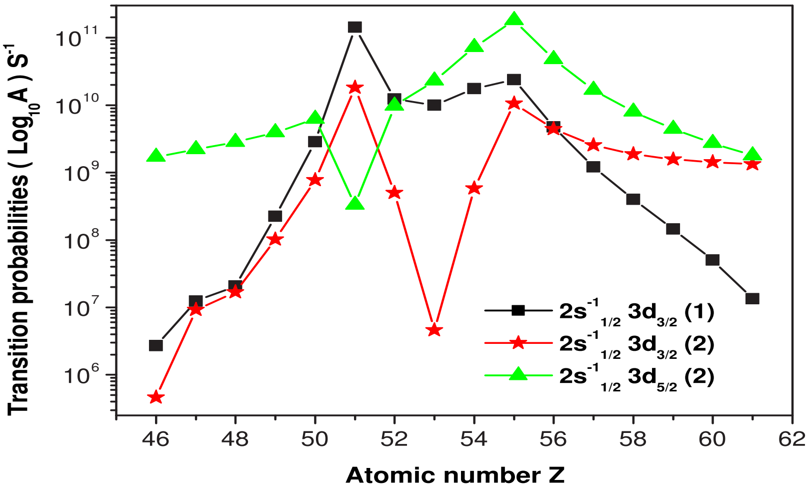

Fig.3 E1 transition probabilities (s^{-1}) from the excited states $2s^{-1}3d$ to the $2p^{-1}_{1/2}3s_{1/2}(1)$ as functions of Z.

6 Conclusion

In summary, the 37 low-lying energy levels and the related transition probabilities connecting these levels in the Ne -like ions from Z=21 to 92 have been calculated by using the MCDF method. The comparison with some available experimental and theoretical results is made for energies and transition probabilities for low Z, middle Z and high Z, respectively along the sequence. A good agreement can be obtained for both of them.

Based on the systematic calculations, all possible energy-crossings among the same J^P level groups have been presented along the whole isoelectronic sequence. It is found that there are several level-crossings for some particular energy levels in different Z regions, those crossings have resulted in great changes of the transition probabilities even for some strong lines. Some of them are diminished and the others are enhanced accordingly. Especially several strong TEOP transitions have been found in some of the neon-like ions, which should be observed in experiment.

Acknowledgement:

This work has been supported by the National Natural Science Foundation of China (Grant No. 10274062 and 10376026),the Excellent Young Teachers Program of MOE, P.R.C., and Foundation of the Center of Theoretical Nuclear Physics, National Laboratory of Heavy Ion Accelerator of Lanzhou, and the Foundation of Northwest Normal University (NWNU-KJCXGC-214) .

References

[1] C. Z. Dong, L. Y. Xie, X. X. Zhou, X. W. Ma, and S. Fritzsche, Hypefine interaction, 146/147, 161 (2003).

[2] U. I. Safronova, C. Namba, I. Murakami, W. R. Johnson, and M. S. Safronova, Phys. Rev. A 64, 012507 (2001).

[3] E.P. Ivanova and I.P. Grant, J. Phys. B 31, 2671 (1998); E.P. Ivanova, A.N. Zinoviev. Phys. Lett. A 274, 239 (2000).

[4] E. Avgoustoglou, W. R. Johnson and J. Sapirstein, Phys. Rev. A51, 1196(1995); E. Avgoustoglou and Z.W. Liu, Phys. Rev. A 54, 1351 (1996).

[5] P. Quinet, T. Gorilia, and E. Biémont, Phys. Scr. 44, 161 (1991).

[6] A. Hibbert, M. Le Dourneuf, and M. Mohan, At. Data Nucl. Data Tables 32, 435 (1993).

[7] E.V. Aglitskii, E.P. Ivanova, S.A. Panin, U.I. Safronova, S.I. Ulitin, L.A. Vainshtein, and J.-F. Wyart, Phys. Scr. 40, 601(1989).

[8] A. K. Bhatia, U. Feldman and J. F. Seely, Atomic Data and Nucl. Data Tables 32, 435 (1985).

[9] N. Nakamura, D. Kato, and S. Ohtani, Phys. Rev. A 61, 052510 (2000).

[10] G. Yuan, Y. Kato, R. Kodama, K. Murai, and T. Kagava, Phys.Scr. 53, 197 (1996).

[11] P. Beiersdorfer, M.H. Chen, R.E. Marrs, and M.A. Levine, Phys. Rev. A 41, 3453(1990); P. Beiersdorfer, Nucl. Instrum. Methods Phys. Res. B 56, 1144(1991).

[12] D.D. Dietrich, A. Simionovici, M.H. Chen, G. Chandler, C.J. Hailey, P.O. Egan, P.H. Mokler, S. Reusch, and D.H.H. Hoffmann, Phys. Rev. A 41, 1450 (1990).

[13] F. A. Parpia, C. Froses Fischer, I P. Grant, Compt. Phys. Commun. 94, 247 (1996).

[14] S. Fritzsche, C. Fischer Froese, and C. Z Dong, Compt. Phys. Commun. 124, 340 (2000).

The Need of Precision Atomic Structure Calculations for the Study of Plasma Processes

KOIKE Fumihiro, and KAWAMURA Tohru[1]
Physics Laboratory, School of Medicine, Kitasato University 1-15-1 Kitasato 228-8555 Japan
1) Tokyo Institute of Technology, 4259-G3-40 Nagatsuda 226-8502 Japan
e-mail: koikef@kitasato-u.ac.jp

Abstract

The model for plasma diagnostics or analysis consists of atomic models and plasma models. The precision atomic structure model will stimulate the sophistication of the plasma model and will also provide us with the tools for precision diagnostics or analysis of the plasmas. Two elements for the precision atomic structure calculation have been discussed. One is the necesity of the relativistic treatment, and the other is the indispensability of taking into account the electron-electron correlation effects in multi-electron atoms or ions. The effect of the spectator satellite lines of the heavy atomic ions, which are doped in the inertial nuclear fusion plasma, is discussed in detail based on accurate atomic structure calculations. Precise and accurate calculations have been intruduced for extreme ultra-violet optical transitions of atomic ions with atomic numbers ranging from 48 to 56. Intra N shell transitions of multiplly charged xenon and tin ions are discussed in detail.

Keywords: EUV, atomic structure, atomic transition, optical emission, relativistic theory, MCDF, configuration interaction, electron correlation

1.Introduction

In recent years, the growth of necessity in detailed and sophisticated description of the plasma is becoming noticeable in the study of confinement nuclear fusion plasma as well as the other application fields using plasmas as devises. Because a plasma model is based on the atomic model that may facilitate appropriately the corresponding plasma simulations, a precision plasma model requires precision atomic data. For plasmas containing heavy elements, we must take into account the effects arising from such the complex species. Firstly, the relativistic effects are remarkable. The $\beta = v/c$ parameter is about $14/137 \sim 0.1$ in silicon $1s$ orbital, for example, and the relativistic correction could be a few percent of the total energy. Large spin-orbit term splittings may also appear. Secondly, the electron correlation effects become important especially in the intermediately ionized atoms. In heavy elements, any pair of electrons may come close to provide us with large correlation energies. The energy of correlations of atomic electrons can be considered as typically of a few electron volt. We must take into account the electron correlation effects, when the required accuracy of the atomic transition energies falls in the range of a few electron volt. From the theoretical point of view, a precision atomic model enables us to evaluate the quality of the plasma models without being bothered by the inaccuracy of the atomic data. This means that a precision atomic model is indispensable for the evaluation of the plasma models.

As one of the best methods for the atomic structure calculations, we have employed a set of GRASP (General purpose Relativistic Atomic Structure Program) family codes[1,2,3] to produce the atomic data that fit to the precision plasma physics. We have performed elaborate atomic structure and dynamics calculations, firstly, for the analysis of a chlorine doped inertial fusion plasma[4], and secondly, for the analysis of EUV (Extreme Ultra Violet) radiations from laser irradiated heavy metal atom plasmas. It is revealed that such the sophisticated calculations of the atomic properties are indispensable to accomplish the plasma analysis in a proper way.

2. Kα Emission From Partially Ionized $C\ell$ Atoms

The interaction of ultra-short laser pulses with dense plasma is of wide interest because of its close relevance to challenging researches on femtosecond X-ray probing [5], energetic particle acceleration [6], and Inertial Confinement Fusion (ICF) [7]. Concerning the fast ignition approach to ICF [7], the Kα emission is useful for diagnostics of energetic electrons [8,9]. Measurement of Kα X-ray absorption and/or emission from partially ionized plasmas is also useful, particularly for dense but low temperature plasmas. In dense plasmas, the outer-shell electrons of atoms are ionized mostly by bulk electrons, and the inner-shell electrons are ionized mostly by by fast electrons; we may observe Kα emissions between the nominal Kα and the Heα lines. Figure 1 shows the calculated radiative decay rates of Kα lines for various ionization states of $C\ell$ atoms. In this figure, for the clarity of illustration, only the transitions of the single K-hole states are given; they are $C\ell^{1+}1s^12s^22p^63s^23p^5 \longrightarrow 1s^22s^22p^53s^23p^5, ...C\ell^{13+}1s^12s^22p^1 \longrightarrow 1s^22s^2$. For $C\ell^{14+}$, only transitions associated with $1s^12s^12p^1$ state are shown. The nominal Kα($C\ell^+$) transitions are distributed in the range of 2622-2628 eV. The Kα lines from He-like($C\ell^{15+}$) to O-like($C\ell^{9+}$) $C\ell$ are well-separated from the nominal ones, and those from Ne-like($C\ell^{7+}$) to S-like($C\ell^{2+}$) $C\ell$ are merging together with the nominal ones. The Kα lines of F-like($C\ell^{8+}$) $C\ell$ make a blue wing on the nominal ones. Energy differences from the nominal Kα depend on the ionic charge states. This feature is the main reason why the Kα emission from partially ionized atoms is useful for plasma diagnostics. Actually, an

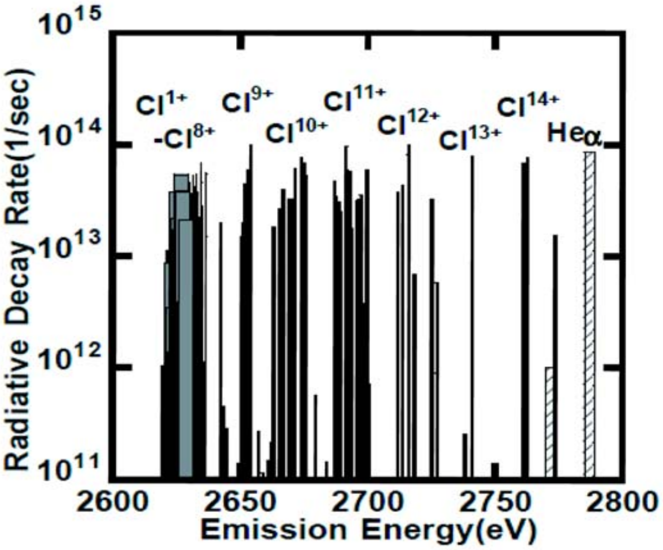

Figure 1: Radiative decay rates for parent Kα lines calculated by GRASP. The hatched bars at the left-hand-side show primary Kα ($C\ell^{+}$).

average charge state associated with this atomic population kinetics will be affected mainly by bulk electron temperature rather than the temperature of fast electrons. Especially, the $C\ell^{9+} - C\ell^{16+} K\alpha$ lines will provide us with plasma-temperature information.

3. Electron Correlations in Atomic Ions Relevant to EUV Light Sources

In these decades, the 13.5 nm range extreme ultra-violet (EUV) light emissions of many electron atomic ions have become of interest in relation to the semiconductor lithography technologies. One of the best candidates for such the EUV light source are considered to be of the intra N shell ($n = 4$ shell) transitions or inter $N-O$ shell transitions of tin (Sn) or xenon (Xe) multiplly charged atomic ions. It is normally indispensable to take into account the electron correlations if we are to evaluate the the transition energies within the accuracy of a few electron volts, because the correlation energy of the atomic valence electrons falls in this range. We have to evaluate, on one hand, the intra N shell electron correlations precicely for excited states as well as the ground states. On the other hand, we have to notice that, in this type of the ions, especially of the Sn ions, a peculiar behavior in the emission spectra has been observed by O'Sullivan and Faukner [10]. They pointed out the narrowing and the shift of the $4f - 4d$ spectra as due to the interactions between $4p^6 4d^{N-1} 4f^1$ and $4p^5 4d^{N+1} 4f^0$ configurations, where N is an integer that runs from 1 to 9.

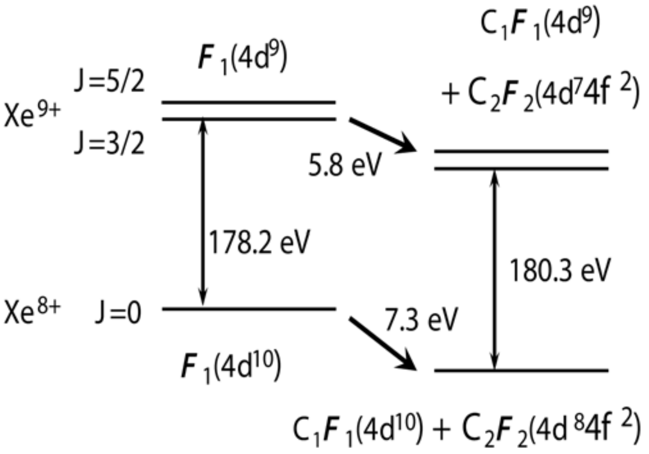

Figure 2: Ground state intra-shell correlation energies of $\mathrm{Xe}^{8+}4d^{10}$ and $\mathrm{Xe}^{9+}4d^9$, and the changes in ionization potentials. The Xe^{8+} ground state energy falls off by 7.3 eV when we include the contribution of $4d^84f^2$ configuration. The Xe^{9+} ground state energy falls off by 5.8 eV when we include the contribution of $4d^74f^2$ configuration. The change in ionization potential is 1.5 eV.

Firstly, to investigate the effect of intra-shell correlations, we have calculated the ground state energies of Xe^{8+} and Xe^{9+} ions with and without the $4d^2 - 4f^2$ correlations. The result is shown in Fig.2. Although whole the $4f^2$ correlation energy exceeds 5 eV, the change in ionization potential of Xe^{8+} ion is as small as 1.5 eV. Because the energies of single electron excited states of Xe^{8+} ions will enter between the ground state energies of Xe^{8+} and Xe^{9+} ions and we may expect that their $4f^2$ correlation energies are more or less the same as of these ground state ions, we can disregard this correlation effect if we consider the value 1.5 eV is small. If not, we must consider the correlation effect properly.

To obtain the $4d - 4f$ transition energy of Xe^{8+} ions, we included the following configurations in the MCDF calculation; those are $4d^94f^1$, $4d^74f^3$, $4d^74f^15p^2$, $4d^95p^1$, $4d^75p^3$, $4d^74f^25p^1$, $4d^95f^1$, $4d^74f^25f^1$, $4d^96p^1$, $4d^74f^26p^1$. We have obtained 104.2 eV for the transition energy, which is 11.90 nm in transition wavelength. This value can be compared to the coresponding experimental data 12.01 eV. To understand the origin of the differnce between the present calculation and the experimental data, we further included several configulations with higher lying f and p orbitals. However, the differnce of 0.11 nm could not be resolved.

Secondly, to gain a further insight of the effects that are pointed out by O'Sullivan and Faukner[10], we have carried out careful MCDF calculations for $4d^N$ ($N = 0$ to 10) atomic ions with atomic number $Z = 48$ to 56. As shown in Fig.3, we found, for example,

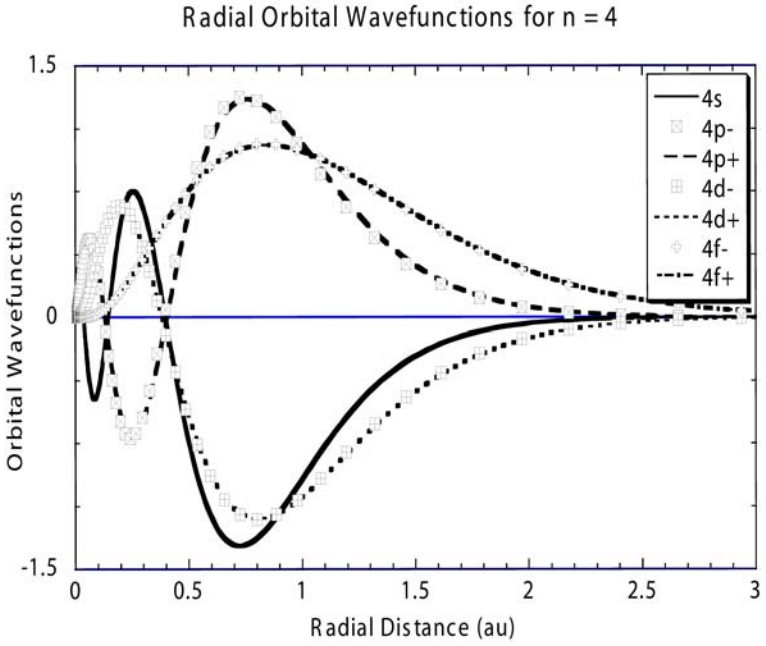

Figure 3: The large component of radial wavefunctions for $4s, 4p, 4d$, and $4f$ orbitals. Lines are of the positive κ orbitals and symbols are of the negative κ orbitals. The positions of the major peak almost coincide for all the wavefunctions.

that in the case of Sn^{12+}, the major peak positions of the $4s$ to $4f$ radial wavefunctions almost coincide, and, furthermore, that the differences of orbital energies between $4p$ and $4d$ orbitals, and $4d$ and $4f$ orbitals coincide within the range of 1%. The $4p^6 4d^1 4f^1$ and $4p^5 4d^3 4f^0$ configurations mix strongly, and the optical $4p - 4d$ and $4f - 4d$ transitions take place coherently, providing us with quite a peculiar EUV emission spectrum.

As an example, we illustrate the calculated G_f-factor distributions of Sn^{10+} in Fig.4. Due to the interference between the $4p^6 4d^4 - 4p^6 4d^3 4f^1$ and $4p^6 4d^4 - 4p^5 4d^5 4f^0$ transitions, we can observe a strong enhancement of the EUV emissions in 13.5 nm region, which provides us with the narrowing and shift in appearance of the emission spectra.

Quite a similar effect has been obtained also for Xe ions, and further on for almost all the atomic ions with $Z = 48 - 56$.

3. Conclusion

The precise and acculate theoretical data of the atomic structures and dynamics that includes the information about the relativistic effect and the electron-electron correlation

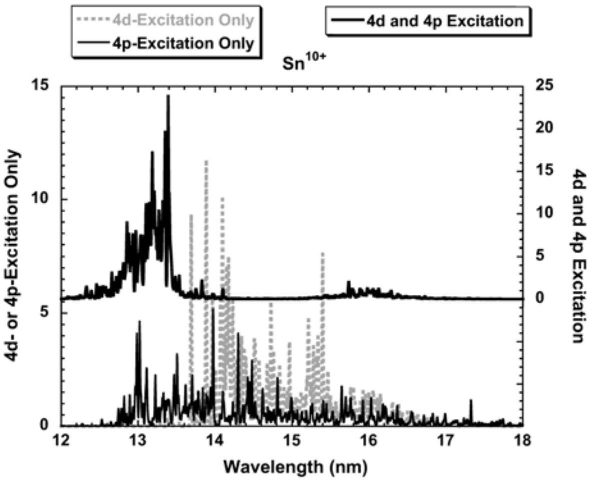

Figure 4: The distribution of G_A factors as function of EUV emission wavelength for $4d-4f$ and $4p-4d$ transitions in Sn^{12+} ions. The spectral distributions are convoluted with the artificial line width of 0.1 nm. The solid line represents the contibution of $4d-4f$ transitions only. The dotted line represents the contibution of $4p-4d$ transitions only. Whereas the dashed line includes both the contributions coherently.

effects provide us with a good base for precision plasma analysis.

Acknowledgement

This work is partly supported by the Leading Project for advanced semiconductor technology of MEXT.

References

[1] K. G. Dyall et al, Comput. Phys. Commun., **55**, 425 (1989).
[2] F. A. Parpia, C. F. Fischer, and I. P. Grant, Commpt. Phys. Commun., **94**, 249(1996).
[3] S. Fritzsche, J. Elec. Spec. Rel. Phenom., **114-116**, 1155 (2001).
[4] T. Kawamura, et al, Phys. Rev. **E66**, 016402 (2002).
[5] Rischel C et al, Nature, **390**, 490-492 (1997).
[6] Mackinnon AJ et al, Phys. Rev. Lett., **86**, 1769-1772 (2001).
[7] Tabak M et al, Phys. Plasmas, **1**, 1626-1634 (1994).
[8] Wharton KB et al, Phys. Rev. Lett., **81**, 822-825 (1998).
[9] Hall TA et al, Phys. Rev. Lett., **81**, 1003-1006 (1998).
[10] G. O'Sullivan, and R. Faukner, Opt. Eng. **33**, 3978 (1994).

Emissions from impurities in the Large Helical Device

T. Kato, T. Obara, R. More, D. Kato, I. Murakami,
M. Goto, K. Sato, H. Funaba, K. Ida, B. Peterson and U. Safronova[1]

National Institute for Fusion Science, Toki, Japan
[1] *University of Nevada, Reno , USA*

Abstract: We analyzed impurity VUV spectral emission quantitatively. Electron temperature is derived from the intensity ratio of CIII line intensities. Radiation loss sources are identified using spectroscopy and bolometer in the case of radiation collapse caused by neon gas puffing. Time dependent radiation loss of impurity ions are derived from line intensities of impurities. EUV spectra from Xe ions have been measured and are compared with theoretical spectra.
Key words: VUV spectra, impurities, radiation loss, Ne VII, C III, EUV spectra, Xe XI,

1. Introduction

In low temperature plasmas such as divertor or process plasmas, emission from impurities is important for plasma diagnostics and plasma modeling. Time dependent VUV spectra were measured in LHD and are analysed with collisional radiative models for impurities. The Large Helical Device (LHD) is a high temperature laboratory plasma for fusion research in the National Institute for Fusion Science.

We have analysed the spectra measured by two spectrometers; the wavelength ranges are λ = 90 – 130 nm and λ = 10 - 16 nm, respectively. Using the long wavelength spectrometer, spectra were taken every 100ms with 33ms exposure time and CIII、OVI, H Lyα、NeVII, NeVI, NeV lines were observed. We have derived electron temperature from CIII line ratios, and radiation loss from Ne VII lines. Using the short wavelength spectrometer, Xe spectra (~10 nm) were measured after Xe gas puffing. We study the identification of the lines and a model calculation of Xe ion spectra.

2. CIII line intensity ratio

We construct a collisional radiative model (CRM) for C^{2+} ions including levels up to n = 5. Our CRM includes dielectronic recombination to excited states [1, 2]. We derived effective rate coefficients for CIII lines, I_r ($2s^2\ ^1S$ - $2s2p\ ^1P$, 977A) and I_t ($2s2p\ ^3P$ - $2p^2\ ^3P$, 1175A) as a function of electron temperature and density. We studied the temperature and density dependences of line intensities using our CRM.

CIII line intensity ratios can distinguish ionizing or recombining plasma phases since the intensity ratio I_t (2s2p ^3P – 2p^2 ^3P)/I_r (2s^2 ^1S – 2s2p ^1P) is smaller than unity in an ionizing plasma and greater than unity in recombining plasma as shown in Fig. 1. We compare to spectra measured in LHD for cases where the spectra can be classified as ionizing or recombining plasma.

Observed spectra were taken for a plasma heated by ECH (#15080) and heated by Neutral Beam Injection (NBI) (#28967). Near the time of radiation collapse, impurity line emission increases by more than a factor 4. For #28967 case, the carbon spectra always indicate an ionizing plasma despite rapid cooling caused by radiation collapse because NBI is still on. In this shot we found the plasma is always in an ionizing phase. The temperature derived from the intensity ratios is as follows; Te ~ 40 eV (t = 0.2 - 0.8sec), Te ~ 40 eV -> 20 eV (t = 0.8 –1.1sec) Te ~ 3 eV(max radiation, t =1.3sec), Te drops to 2 eV (t = 1.4 - 1.7sec).

3. Neon ion spectra and radiation loss

We have analysed VUV spectra for a NBI heated (#28967) experiment with neon gas puffing which showed radiation collapse. We derived the radiation loss rate from impurity ions and compared them with the bolometric measurement. The observed spectra at 1.0, 1.2 and 1.3 sec are shown in Fig.2. We identify 2s - 2p fine structure transition lines from neon L-shell ions as a second order diffraction as shown in Fig.3 (a); Ne VII (2s2p ^3P_J - 2p^2 $^3P_{J'}$, 6 lines), Ne VI (2s^{2}2p ^2P_J - 2s2p^2 $^2P_{J'}$, 3 lines) Ne V (2s^{2}2p^2 ^3P_J - 2s2p^3 $^3D_{J'}$, 6 lines), Ne IV(2s^{2}2p^3 ^4S_J - 2s^{2}2p^4 $^4P_{J'}$, 3 lines). We calculate the intensities of Ne VII and VI lines by our collisional radiative model as shown in Fig.4(b). Ion density ratios are derived comparing spectra and calculations. We find the ion densities of Ne $^{6+}$ are about equal to Ne $^{5+}$

The absolute neon ion density is derived from charge exchange spectroscopy (CXS) at t = 1.0 sec. The neutral hydrogen heating beam has 140 keV energy. The 5249A line (n = 11 – 10) of Ne^{9+} is produced by charge transfer (Ne^{10+} + H --> Ne $^{9+}$ (n = 11) + H$^+$ --> Ne $^{9+}$ (n =10) + hv). The emission rate coefficient to produce NeX 5249A line by charge exchange is calculated by ADAS code [3] as $<\sigma_{CX}v> = 1.0 \times 10^{-8}$ cm^3 s^{-1}. State - selective charge transfer cross sections to high nl states are important to calculate emission rate coefficients. The absolute density of Ne^{10+} ions N(Ne^{10+}) = 2.5 x 10^{11} cm^{-3} at the plasma center is derived. We derived absolute time dependent impurity radiation loss from VUV spectra combining with the absolute value of neon ion density. Based on the density of Ne^{10+}, other neon ion densities are calculated by MIST code [4]; N(Ne $^{9+}$) = 6.3 x10^{10} cm^{-3}, N(Ne^{8+}) = 1.3 x10^{11} cm^{-3}, N(Ne^{7+}) = 3.1 x10^{10} cm^{-3}, N(Ne^{6+}) = 3.1 x10^{10} cm^{-3}, N(Ne^{5+}) = 2.5 x10^{10} cm^{-3} . The radiation loss rate coefficients of neon ions by ADAS code are R(Ne^{9+}) = 10^{-26} W cm^3 at 1 keV, R(Ne^{8+}) = 10^{-26}

W cm^3 at 1 keV, R(Ne^{7+}) = 5 x10^{-26} W cm^3 at 100 eV, R(Ne^{6+}) = 10^{-25} W cm^3 at 100 eV, R(Ne^{5+}) = 10^{-25} W cm^3 at 100 eV. Assuming n_e = 10^{13}cm^{-3} the radiation loss from neon K-shell ions is 17 KWm^{-3} at 1 keV and neon L-shell ions gives 72 KWm^{-3} at 100 eV. This value can be compared with the bolometric measurement 60 KW m^{-3} at ρ = 0.9 for 1 sec in Fig. 4. The value ρ is the distance from the plasma center normalized by the radius of the last closed magnetic surface.

From the observed intensity of NeVII 2s2p ^{3}P – 2p^2 ^{3}P at around 500A, the absolute intensities of other ions are estimated. With N(Ne^{6+}) = 3 x10^{10} cm^{-3}, n_e = 10^{13}cm^{-3} and effective excitation rate coefficients, C_{eff}(561A) = 2 x 10^{-9} and C_{eff}(564A) = 7 x 10^{-10}, absolute observed volume emissivities are obtained for I(561A) = 6 x 10^{14} photons cm^{-3} s^{-1} and I(564A) = 2 x 10^{14} photons cm^{-3} s^{-1}. From CIII 977.0A 2s^2 ^{1}S – 2sp^2 ^{1}P observed intensity, absolute volume emissivity I(CIII 977A) = 4.6 x 10^{14} photons cm^{-3} s^{-1} is derived using the intensity of neon emission lines. With C_{eff}(977A) = 6 x 10^{-8} cm^3 s^{-1} and n_e = 10^{13}cm^{-3} , density of C^{2+} ions N(C^{2+}) = 7.6x10^8 cm^{-3} is obtained. From our collisional radiative model, the radiation loss from C^{2+} is 0.8KW m^{-3} and radiation loss of carbon L shell ions is 2.3KW m^{-3}. Based on the radiation loss at t = 1 sec, time dependent radiation loss for C $^{2+}$ is derived from time variation of VUV line intensity. From OVI 1031A 2s ^{2}S – 2p ^{2}P observed intensity at t =1.0 sec, absolute volume emissivity I(OVI 1031A) = 6.6 x 10^{14} photons cm^{-3} s^{-1} is derived. With C_{eff}(1031A) = 1.3 x 10^{-8} cm^3 s^{-1} and n_e = 10^{13}cm^{-3} density of O^{5+} ions, N(O^{5+}) = 7.7x10^9 cm^{-3} is obtained. Radiation loss of 8 KWm^{-3} from O^{5+} is derived. Radiation loss from L-shell is estimated to be 16 KWm^{-3}. Based on the absolute values at 1 sec, we can estimate the time dependent radiation loss from the time dependent line intensities as shown in Fig. 5. Due to radiation loss by neon L-shell ions, temperature falls from periphery until radiation collapse. After radiation collapse, low charged carbon ions are the dominant source of radiation.

4. Xe ion spectra

Extreme-ultraviolet (EUV) light sources from compact plasmas are now intensively studied for the next generation of lithography. The emission of multicharged Xe ions has strong peaks near 11 and 13 nm and these emission near 13nm are attributed to transitions in Xe^{10+}. Better knowledge of this emission is important for EUV sources and for optimization of a 13.5nm EUV source. Recently EUV spectra from Xenon ions in LHD have been measured in the wavelength range 10 – 17 nm. We analyze the spectral lines near 13 nm. We compare the spectra with theoretical calculations and identify the spectral lines from Xe $^{10+}$ ions. We can make a bench mark test of computer codes using the observed spectral lines. This is important because the theory has not been extensively tested for such high- Z low charge ions. We will study plasma conditions which give the best EUV emission and make a collisional radiative model for high- Z many- electron ions.

Xe gas was puffed into LHD plasma and the EUV spectra from Xe ions were measured every 1 sec. The electron temperature at the center of LHD is about 3keV whereas the temperatures at periphery are 10 - 30 eV. Generally Xe emissions are weak in the beginning of the plasma and strong during or after radiation collapse. A 2m grazing incidence multichannel spectrometer SOXMOS [5] with 600g/mm grating was used for measurement. The measured line-width (FWHM) is $\Delta\lambda$ = 0.023nm at 13.283nm for Fe XXIII line.

We used the spectra before Xe gas puffing for wavelength calibration. The spectra with and without Xe gas puffing are shown in Fig.6. Iron FeXXIII 13.283nm and Cr XXI 14.9900 nm lines were mainly used as references. After wavelength calibration, we compare the observed spectra in different shots plotted with the same wavelength scale. In Fig.7, we show the observed spectra measured from two different shots in this wavelength scale. The strong peaks numbered as 1,2, , , are thought to be lines from Xe ions comparing to the spectra obtained without Xe gas puff except the line number 4 which is considered as Fe XXIII.

Since the electron configuration for Xe^{10+} is complicated, we cannot find accurate theoretical atomic data. Recently Churilov et al (2003) in NIST measured Xe^{10+} spectra and gave a list of prominent lines [6]. Sasaki showed the spectra based on atomic data from the Hullac code [7]. We calculated atomic data for Xe^{10+} with two different atomic codes; MCDF (Multiconfiguration Dirac-Fock) by Y. Ki. Kim[8] and Cowan (Multiconfiguration Hartee-Fock) code [9] in relativistic mode. For a many-electron system like the Xe^{10+} ion, electron correlation and configuration interaction are important. Configurations taken into account in calculations are $4s^2 4p^6 4d^8$ (lower state) and $4s^2 4p^6 4d^7 5p^1$ (upper state) for MCDF code and $4s^2 4p^6 4d^8$, $4s^2 4p^4 4d^{10}$ (lower state) and $4s^2 4p^6 4d^7 5p^1$, $4s^2 4p^6 4d^7 4f^1$, $4s^2 4p^5 4d^9$ (upper state) for Cowan code. We obtain many lines from the results of calculation by MCDF code and Cowan code. MCDF calculation includes 421 line and Cowan code calculation includes 195 lines. Atomic data of wavelength and transition probabilities Ar are compared. The comparison with the data by Churilov [6] is also made. Since it is difficult to compare the atomic data in detail for each lines, we made a convoluted spectra with a Gaussian profile assuming the integrated line intensity is equal to theoretical value gAr (s^{-1}) where g is a statistical weight of the upper level i and Ar is a transition probability from the upper level i to the lower level j. As seen in Fig.7, the feature in total convoluted spectra looks similar and strong peaks coincide each other. However the detailed structure are different.

We compared the observed spectra with a theoretical convoluted spectra based on the data by MCDF and Cowan codes. The agreements are not very good. However we can identify the strong lines with the error of 0.01nm (0.1A). The comparison of observed spectra with theoretical calculations are shown in Fig. 8. The observed line number 8 at 13.825nm is always strong but the theoretical value of gAr is not large. The lines with the large gAr values in theory are not always strong in measurement. One reason is that the observed lines are emitted by excitation or recombination by electron impact. In order to analyze the intensities we need to make a collisional radiative model which includes all these processes. Another reason is the difference in theoretical atomic data. We have identified the strong observed Xe^{10+} lines. Most of the strong lines are identified with transitions between singlets although the ground state is the triplet $4p^6 4d^8\ {}^3F_4$. This might suggests the lines are emitted through recombination or cascade. Recombination emission is supported by the fact that the emissions are strong in the later phase of the plasma. Strong emission is measured during radiation collapse or after radiation collapse. We plot the time dependent intensities at 4 different times for the shot #42801 in Fig. 9. Most of Xe lines show similar time behaviour. The line number 8 and 12 increase rapidly at late time. Line number 4 is thought to be a FeXXIII line. Since most of the line intensities increase at late times, we think they are emitted from low charged Xe ions such as Xe^{10+} but not Xe^{26+} as reported in W7-AS plasma [10]. LHD spectra can give a bench - mark test of theoretical data for wavelengths of Xe ions. We are making a model for intensities of high Z ions with many electrons.

Work partially supported by EUV leading project in Osaka Univ.

References

[1] T. Kato, M. Kato and R. More, Proceedings of IFSA 2001, Edited by K.A. Tanaka, The Data Science Library, ISBN: 2-84299-407-8, Elsevier, 991- 994 (2002)

[2] T. Kato, M. Kato, R. More, S-Y Zou, M. Goto and S. Morita, Current Developments in atomic, molecular and chemical physics with applications, by Man Mohan by Kluwer Academic/Plenum Publishers, New York, 265 - 272 (2002)

[3] H. Summers, JET-IR 06 (1994), http://adas.phys.strath.ac.uk/

[4] R. Hulse, Nuclear Technology/Fusion, 3, 259 (1983)

[5] J.L. Schwob et al, Review o Scientific Instrument, 58,(9),1601 (1987)

[6] A. Sasaki, J. Plasma Fusion Res., 79, 219 (2003)

[7] S. Churilov, Y.N. joshi and J. Reader, Optics letters, 28, 1478 (2003)

[8] Y.Ki. Kim and M.E. Rudd, Phys.Rev. A (1994)

[9] R.D. Cowan, The Theory of Atomic Structure and Spectra, Univ. of California Press,

Berkeley (1981)

[10] H.H. Hacker, R. Burbenn, K. Kondo et al, Appl. Phys. B, 59 (2001)

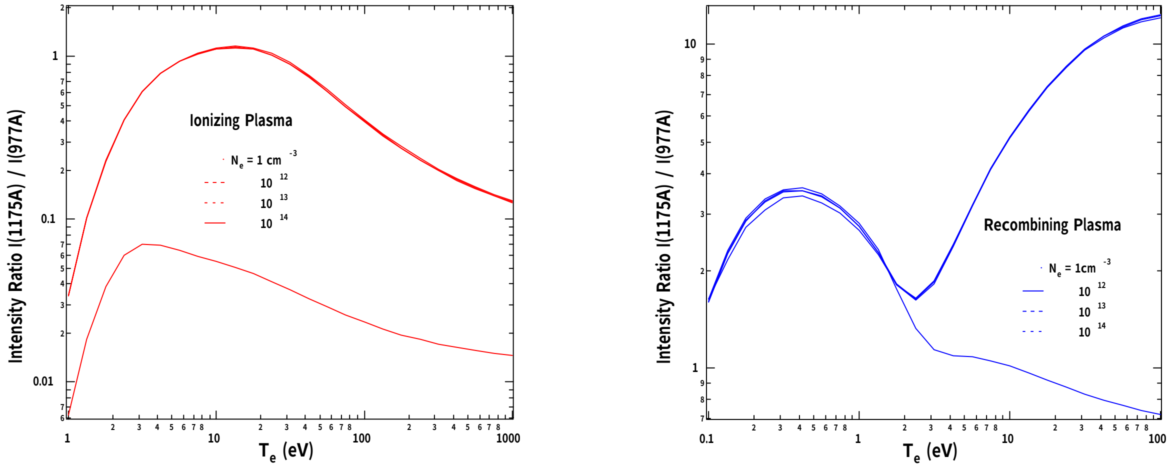

(a) (b)

Fig.1 Intensity ratio of C^{2+} lines in ionizing (a) and in recombining plasma (b).

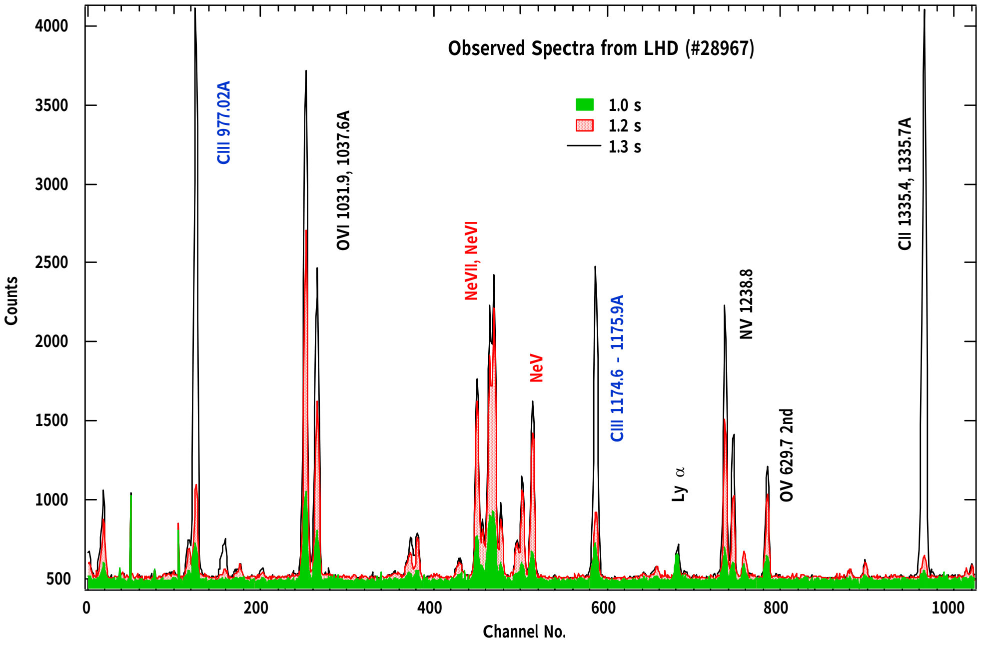

Fig.2 Observed time dependent VUV spectra

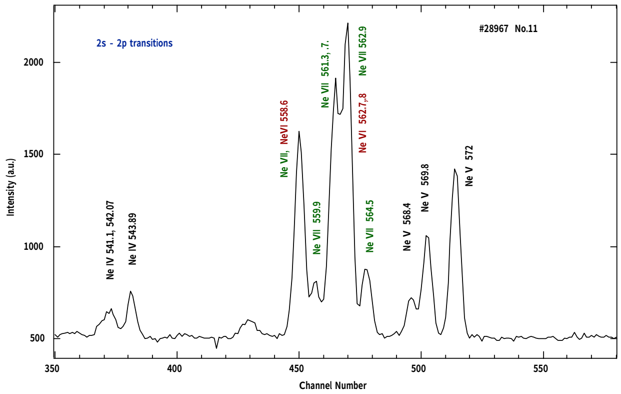

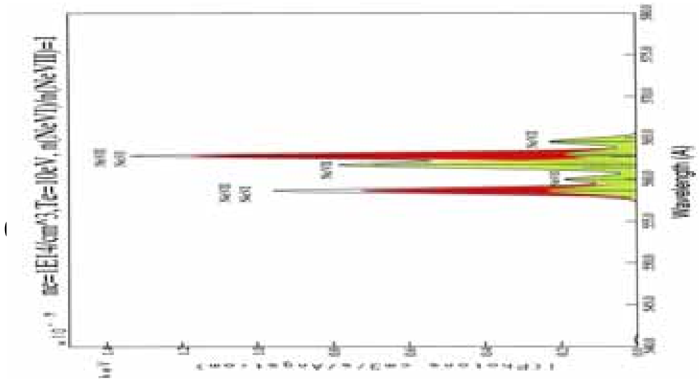

(a) (b)

Fig.3 Observed (a) and theoretical (b) spectra of NeVII and NeVI ions

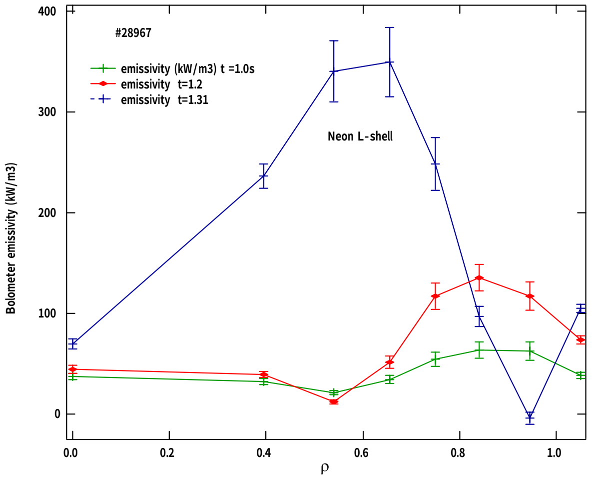

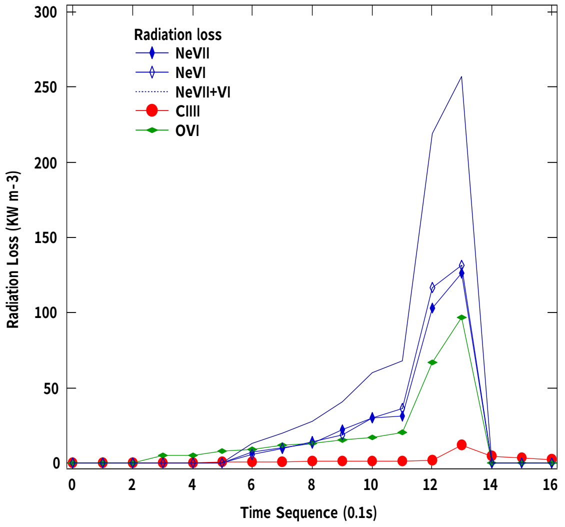

Fig. 4 Radial emission profile measured by bolometer

Fig. 5 Time dependent radiation loss from impurity ions

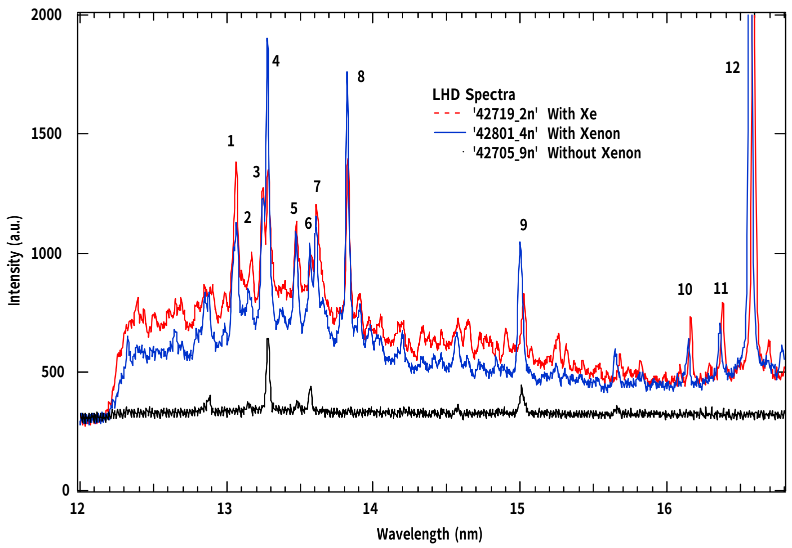

Fig. 6 Observed spectra with Xe puffing and without Xe puffing

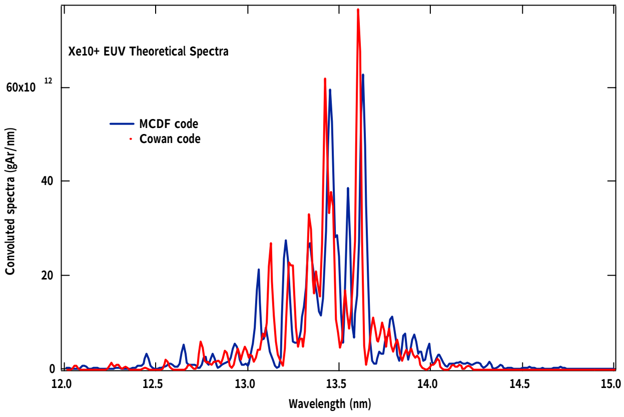

Fig.7 Theoretical spectra by the MCDF code and the Cowan code.

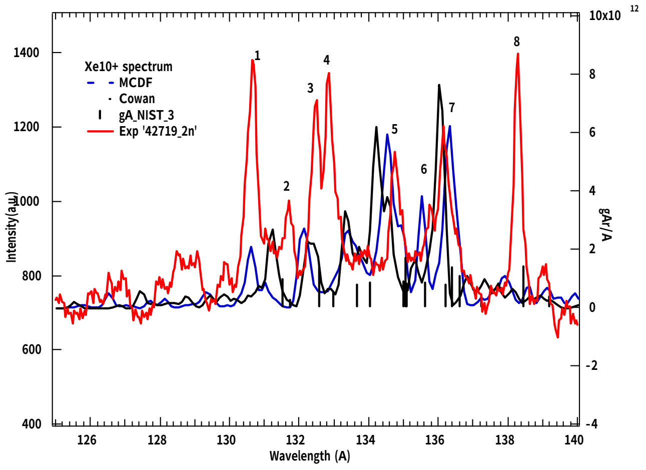

Fig.8 Comparison with an observed spectrum and theoretical spectra

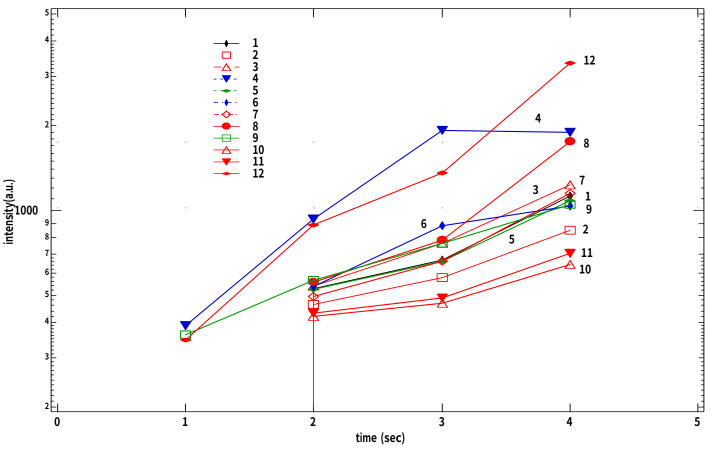

Fig.9 Time dependence of the observed line intensities

Plasma Spectroscopy of Hydrogen Ice Pellets in the Large Helical Device

M. Goto, R. Sakamoto, S. Morita, H. Yamada, and LHD experimental group

National Institute for Fusion Science
Toki 509-5292, Japan

Abstract

A pellet of solid hydrogen is injected into a plasma in the Large Helical Device, and a strong radiation from a dense plasma which sorounds the pellet is spectroscopically observed. Emission lines of neutral hydrogen exhibit typical Stark broadening profiles and the electron density is determined by comparing them with theoretical data. The simultaneously observed continuum radiation is found to cosist of two components which accompany the radiative recombination and attachment processes. The latter process is what yields negative ions. From the profiles and absolute intensities of the two continuum radiation, the electron temperature, the ion and atom densities, and the plasma volume are determined. These results indicate that the plasma condition is near to a complete LTE (local thermodynamic equilibrium). Among the isolatedly observed hydrogen lines, only the Balmer α line profile is found distorted due to a self-reabsorption effect. With the help of a one-dimensional radiation transport model, the plasma length in the direction of the line of sight is estimated. The result implies the plasma is elongated in the direction of the magnetic field.

1 Introduction

The pellet injection with solid hydrogen is regarded as a promising technique for an effecient particle fueling for fusion plasmas. The aim of this method is to provide particles in the core region of the plasma, and therefore it is important to measure how deep a pellet can penetrate into the plasma before it is completely ablated and ionized.

An injected pellet is surrounded by a relatively high density plasma which exhibits a intense radiation immediately after it penetrates into the plasma beyond the last closed magnetic surface. Such a dense plasma is called *cloud*. The conventional method to estimate the penetration depth of the pellet is to measure the Balmer α line intensity of neutral hydrogen from the cloud. Since the line intensity is generally thought to be proportional to the ionization flux of the neutral hydrogen irrespective of the plasma parameters, the temporal variation of the line intensity is directly interpreted as the spatial particle deposition profile. Note that the word 'flux' is here defined as the number of events, such as the ionization or recombination, per unit volume and time. However, the proportionality factor between the line intensity and the ionization flux may change in particular in high density conditions and the temperature dependece also exists. Therefore, these parameter dependences have to be taken into account for a more precise analysis.

Under such circumstances, we become to be interested in the plasma parameters in the cloud. Though there already exist some studies which measure the electron density from the observed Stark broadening in hydrogen lines [1–5], few attempts have ever been made for a comprehensive understanding of the plasma condition in the pellet cloud. Moreover, there exists

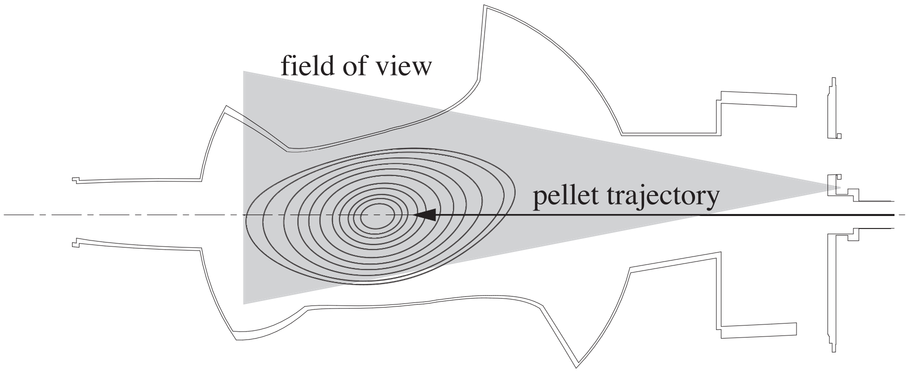

Figure 1: Trajectory of the injected pellet. The gray area indicates the field of view of our observation.

little experimental information about the electron temperature and the ionization degree. These parameters are indispesable for a quantitative determination of the effective ionization flux in the cloud. This paper introduces our attempts to determine as many parameters as possible experimentally, and derives a remarkable feature concerning the plasma condition in the cloud from them.

2 Experiment

In the Large Helical Device (LHD), the pellet injection is considered an essential technique to attain a high density plasma and this method has been intensively investigated. Each pellet has a cylindrical shape, both the diameter and length of which are 3 mm. The injection path goes throught the plasma as shown in Fig. 1.

A pellet starts to emit intensive light as it enters into the plasma, and this strong radiation typically last about 400 μs. Since a pellet has a velocity of about 1 km/s, this time duration corresponds to the length of about 40 cm.

Spectra of the emission light from the cloud is observed with an optical fiber having a diameter of 100 μm. An end surface of the fiber is located at an observation port of the vacuum chamber to see the pellet from behind as shown in Fig. 1. The field of view is so wide that whole the light emission from an injected pellet is observable. The other end surface of the fiber is put at the entrance slit of a UV and visible spectrometer (Chromex 500is) and the spectra are recorded on a CCD (charge coupled device) detector.

The spectrometer has a focal length of 50 cm, and a 100 grooves/mm grating is used for the present observation. The reciprocal wavelength dispersion is 19.957 nm/mm. The CCD detector consists of 1024 pixels (wavelength direction) $\times$ 256 pixels, and the each pixel size is 26 μm $\times$ 26 μm. Accordingly, the wavelength range as wide as about 500 nm is measured at the same time. This wavelength range covers whole the Balmer series lines of hydrogen. In the actual measurement spectra has been taken every 16 μs with the help of the so-called “fast kinetic mode” [6]. Here, we give our attention on a single time slice in which the strongest radiation is observed.

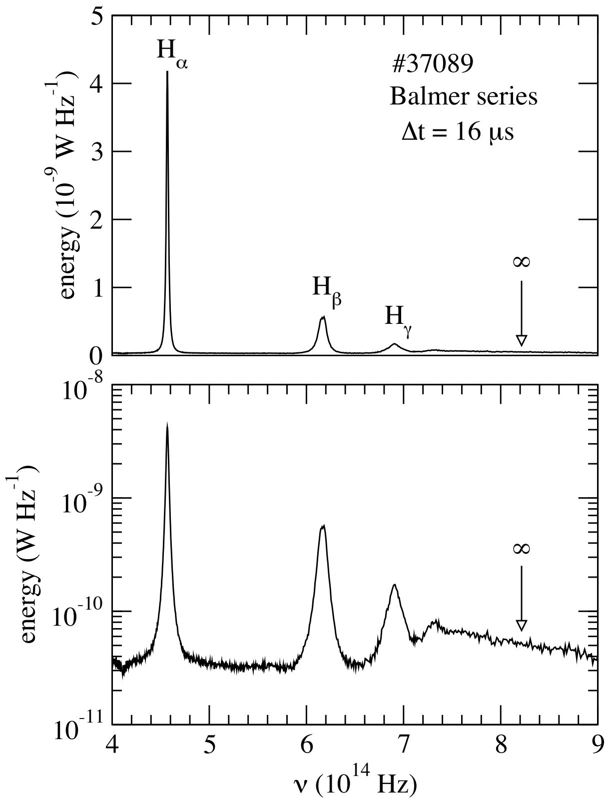

Figure 2: An example of the obtained spectra. The upper and lower panels show the same data, but the ordinate is in the linear scale for the former and in the logarithmic scale for the latter.

3 Results and discussion

Figure 2 shows an example of the obtained spectra of Balmer series lines of neutral hydrogen. Only the Balmer α, β, and γ lines are isolatedly observed and other series lines are merged with the neighbors each other to be a continuum radiation. The profiles of the isolated lines are dominantly determined by the Stark broadening and we evaluate the electron density by comparing the observed profiles with the theoretical data [7]. From the Balmer β and γ lines the same electron density, $n_e = 2.2 \times 10^{23}\,\mathrm{m}^{-3}$, is obtained independently. On the other hand, the Balmer α line yields an about twice higher density due maybe to the distortion of the apparent profile by the self-reabsorption. This effect is quantitatively examined later. Meanwhile, the Inglis-Teller formula [8]

$$\log n_e = 29.26 - 7.5 \log p_{\max}, \tag{1}$$

where $p_{\max}$ is the highest principal quantum number of the isolatedly observed line, suggests $p_{\max} \sim 6$ for the obtained density and this is consistent with the experimental data.

The continuum radiation power profile is fitted with the combination of those by radiative recombination processes

$$\mathrm{H}^+ + \mathrm{e} \to \mathrm{H}(p = 2, 3, \ldots) + h\nu, \tag{2}$$

where p denotes the principal quantum number, and by radiative attachment processes

$$\mathrm{H} + \mathrm{e} \to \mathrm{H}^- + h\nu, \tag{3}$$

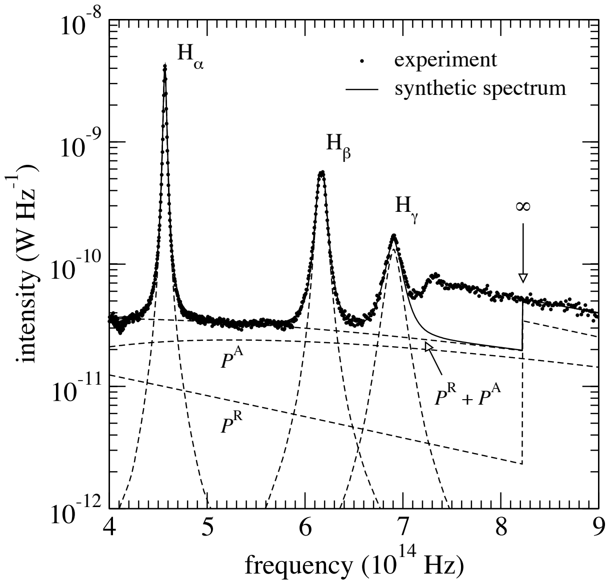

Figure 3: Fitting result of the experimental data under an assumption of the LTE condition with $T_e = 1.0\,\mathrm{eV}$ and $n_e = 2.2 \times 10^{23}\,\mathrm{m}^{-3}$. The influence of the self-reabsorption for the Balmer α line is taken into account. The components of the continuum emission, P^R and P^A, indicate the radiations accompanying the radiative recombination and attachment processes, respectively.

where h and ν are the Planck constant and the frequency of the emitted photon, respectively. The radiation powers by the former and the latter processes are respectively expressed as

$$P^R(\nu) = h\nu f(\varepsilon)\nu\sigma_{\mathrm{rad}}(\varepsilon)\frac{\mathrm{d}\varepsilon}{\mathrm{d}\nu}n_i n_e V, \tag{4}$$

and

$$P^A(\nu) = h\nu f(\varepsilon)\nu\sigma_{\mathrm{att}}(\varepsilon)\frac{\mathrm{d}\varepsilon}{\mathrm{d}\nu}n_H n_e V', \tag{5}$$

where n_i and n_H are the densities of proton and the ground state neutral hydrogen atom, respectively, and V and V' are the plasma volumes which emit the recombination continuum radiation and the attachment continuum radiation, respectively. The cross sections of radiative recombination, σ_{rad}, and attachment, σ_{att}, are obtained from those of the photoionization and photodetachment processes, respectively. As the energy distibution function of free electrons, $f(\varepsilon)$, we assume here a Maxellian function throughout. The parameters which best explain the experimental result, both the profile and the absolute intensity, is $T_e = 1.0\,\mathrm{eV}$, $n_e n_i V = 1.7 \times 10^{41}\,\mathrm{m}^{-3}$, and $n_e n_H V' = 1.4 \times 10^{43}\,\mathrm{m}^{-3}$. The components are individually shown in Fig. 3. Since the electron density is already estimated from the Stark broadening as $n_e = 2.2 \times 10^{23}\,\mathrm{m}^{-3}$, $V = 3.5 \times 10^{-6}\,\mathrm{m}^3$ is obtained under an assumption of $n_i = n_e$. Furthermore, $n_H = 1.8 \times 10^{25}\,\mathrm{m}^{-3}$ is also determined if the plasma volumes which emit both the continuum radiations are identical, namely, $V = V'$.

In a relatively high density plasma like this case, most of the excited levels of neutral hydrogen are expected to be in a local thermodynamic equilibrium (LTE) with proton. If so, the population densities of those levels, $n(p)$, are expressed with the Saha-Boltzmann equation as

$$n(p) = p^2 \left(\frac{h^2}{2\pi m k T_e}\right)^{3/2} \exp\left[\frac{R}{p^2 k T_e}\right] n_e n_i, \tag{6}$$

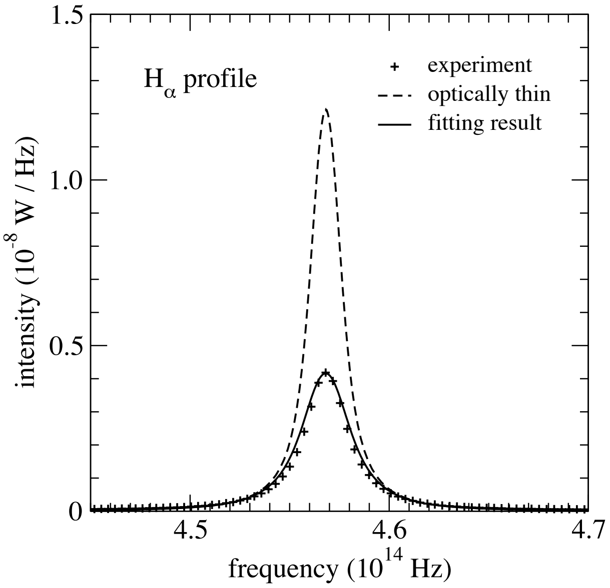

Figure 4: Observed Balmer α line profile (crosses). Also shown are the expected line profile under an assumption of LTE condition ($T_e = 1.0$ eV and $n_e = 2.2 \times 10^{22}$ m^{-3}) for the $n = 3$ level, and the fitting result where the self-reabsorption effect is taken into account.

where m, k, and R are the electron mass, the Boltzmann constant, and the Rydberg constant, respectively. What should be noted here is that the relation between $n(1)$ ($\approx n_H$) and n_i also nearly satifies this equation, and this means a "complete LTE" is almost established.

Figure 3 also shows the Balmer α, β, and γ profiles in the absolute units for the present plasma, and the latter two line profiles are found to agree well with the experimental data. For the Balmer α line, the LTE intensity is found higher than the observed one by a factor of about 3. When the self-reabsorption is significant, the observed line intensity may be reduced and the apparent line width may be increased. This is qualitatively agree with the present result.

It is, however, difficult to carry out a precise evaluation of the absorption effect on the line profile since we know little concerning the geometrical shape of the pellet cloud. Instead we attempt a quantitative analysis with a simplified model. We consider a one-dimensinal model having homogeneous n_e, T_e, and n_H. The radiation transport is expressed with a equation as

$$\frac{dI_\nu(x)}{dx} = -\kappa_\nu I_\nu(x) + \eta_\nu, \tag{7}$$

where $I_\nu(x)$ is the radiance, and κ_ν and η_ν are the absorption and emission coefficients, respectively. By integrating Eq. (7) and adopting a boundary condition $I_\nu(0) = 0$, we obtain

$$I(\nu)(x)4\pi S = \frac{\eta_\nu 4\pi S\, x}{\kappa_\nu x}\left[1 - \exp\left(-\kappa_\nu x\right)\right]. \tag{8}$$

Here, both hands side of the equation are multiplied by a factor of $4\pi S$, where S is the area of the apparent emission volume for the observer, so that the units coincide the value in the ordinate of Fig. 3. The absorption coefficient κ_ν is expressed as

$$\kappa_\nu = \frac{h\nu}{4\pi} B(3,2) n(2) P(\nu), \tag{9}$$

where $B(3,2)$ is Einstein's B coefficient for the absorption between $n = 2$ and $n = 3$ levels, and $n(2)$ is the population density of the $n = 2$ level. $P(\nu)$ stands for a normalized absorption profile which satisfies $\int P(\nu)\mathrm{d}\nu = 1$. We adopt a Stark broadening profile corresponding to $n_\mathrm{e} = 2.2\times10^{22}\,\mathrm{m}^{-3}$ under optically thin condition as $P(\nu)$, and then $n(2)\ell = 4.5\times10^{18}\,\mathrm{m}^{-3}$ is obtained as a result of the fitting of the Balmer α line profile in Fig. 3 with Eq. (8). The result is shown in Fig. 4. This result is reflected on the Balmer α line profile in Fig. 3. Since the level $n = 2$ is also expected to be in LTE, $n(2) = 1.9\times10^{21}\,\mathrm{m}^{-3}$ is obtained, and finally, $\ell = 2.4\times10^{-3}$ m is derived. Considering the plasma volume determined in Section 3 ($V = V' = 3.5 \times 10^{-6}\,\mathrm{m}^3$), we guess the cloud is elongated in the direction parpendicular to the line of sight, or, in the direction of the magnetic field. This is confirmed by a picture image taken by a CCD camera.

References

[1] D. H. McNeill *et al.*, Phys. Rev. Lett. **55**, 1398 (1985).

[2] G. A. Wurden *et al.*, Rev. Sci. Instrum. **61**, 3604 (1990).

[3] D. H. McNeill *et al.*, Phys. Fluids B **3**, 1994 (1991).

[4] L. R. Baylor *et al.*, Nucl. Fusion **32**, 2177 (1992).

[5] H. W. Müller *et al.*, Nucl. Fusion **42**, 301 (2002).

[6] M. Goto *et al.*, Phys. Plasmas **10**, 1402 (2003).

[7] C. Stehlé and R. Hutcheon, Astron. Astrophys. Suppl. Ser. **140**, 93 (1999).

[8] D. R. Inglis and E. Teller, Astrophys. J. **90**, 439 (1939).

EXCITED HYDROGEN ATOM FORMED BY NON-ADIABATIC ELECTRON TRANSFER FROM METAL SURFACES

Daiji Kato, Tetsuo Tanabe*, and Takako Kato

National Institute for Fusion Science, 322-6 Oroshi-cho, Toki 509-5292, Japan

**Nagoya University, Nogoya 464-8603, Japan*

Abstract

Formation of excited hydrogen atoms at a tungsten surface is explained by the non-adiabatic single electron capture by protons. Occupation probabilities of the excited levels are calculated using a one-dimensional mixed quantum-classical model for proton velocities of 0.1 – 1.0 a.u. The non-adiabatic evolution of electronic states is attributed to wave functions astride of the potential ridge.

Keywords: Ion-surface interaction, electron capture, non-adiabatic transition, time-dependent Schrödinger equation.

1. Introduction

Electronic processes in ion-surface interactions have been attracting interests in variety of fields such as nuclear fusion energy research, surface diagnostics, chemical reaction in the interstellar medium [1], and so on. For the hydrogen recycling in magnetically confined fusion devices, experimental studies have revealed importance of excited states in energetic neutrals of atomic hydrogen isotopes backscattered at surfaces of plasma facing high-Z metals [2]. However, the excited-state distribution is little understood.

The excited states of atomic hydrogen are very unstable in the bulk of metals; they readily disappear (be ionized) due to strong screening effect by high-density conduction electrons. The excited states are formed by electron capture above the surface where the electron density decays exponentially. The excited states therefore might be useful as a novel probe of *topmost* surface diagnostics of the metals.

Besides the practical importance, the excited state formation in the ion-surface interaction is a challenging problem in theoretical point of views due to inherent complexity of many-electron processes involved. Pioneering studies on electron transfer at metal surfaces have been undertaken by Brako and Newns [3] and Burgdörfer [4]. Both give the similar results for occupation probabilities of atomic states within the adiabatic approximation to time variation of the ion-surface interaction. In this paper, we present theoretical calculations for single electron capture by protons from a tungsten surface with emphasis on the non-adiabatic promotion of the excited state formation. Atomic units $(\eta = m_{\mathrm{e}} = 1)$ are used throughout unless otherwise stated.

2. Theoretical Model

In the present model, it is assumed that the formation of the excited hydrogen atoms is due to single electron capture by protons from the conduction band of the metal. The hydrogen atom (proton + electron) above the metal surface is illustrated in Figure 1. We use the spherical coordinates whose origin is located at the proton to describe electronic wave functions. Geometry of the electronic system is restricted to $\theta = 0$; the angular freedom of motion is omitted in the present model. Because it is assumed that the electron motion along a perpendicular from the proton to the surface may play the most important role in the electron transfer process. The electron moves under influences of three potentials: Coulomb attractive potential of the proton, attractive potential of the surface dipole layer and the exchange-correlation effect ($V_{\mathrm{e}}^{\mathrm{I}}$), and repulsive potential of a pile of electron density at the

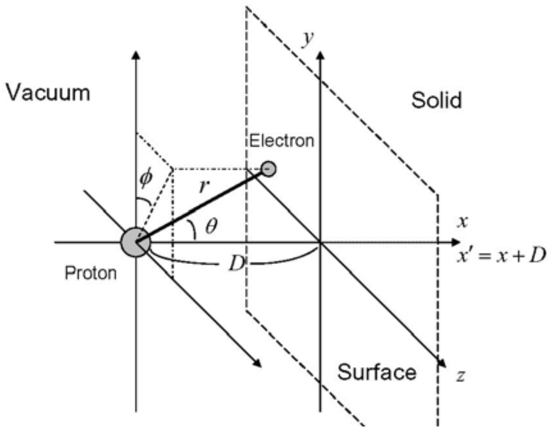

Figure 1: Coordinate system of hydrogen atom above metal surface.

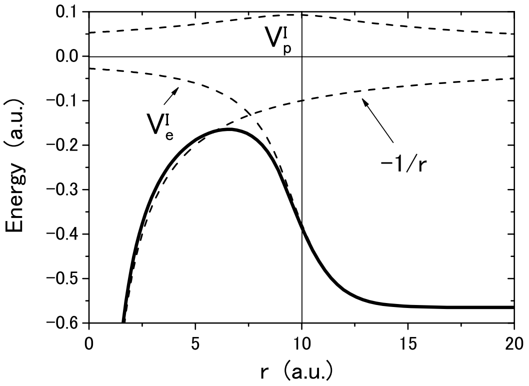

Figure 2: Effective potential of electron for tungsten (110) surface. Bold solid line is sum of the three potentials. D =10 a.u.

surface induced by the proton ($V_{\mathrm{p}}^{\mathrm{I}}$). The semi-empirical formula is employed for $V_{\mathrm{e}}^{\mathrm{I}}$ of tungsten proposed by Jennings, Jones and Weinert [5]. $V_{\mathrm{p}}^{\mathrm{I}}$ is obtained from the static linear density response function of the conduction electrons whose wave functions are calculated using the $V_{\mathrm{e}}^{\mathrm{I}}$ [6]. Figure 2 shows the potentials for the tungsten surface.

The electronic wave function at each proton-surface distance D is the solution of the one-dimensional Schrödinger equation,

$$\hat{H}(D)\Phi(r;D) = \left\{-\frac{1}{2}\frac{d^2}{dr^2} - \frac{1}{r} + V_{\mathrm{e}}^{\mathrm{I}}(x(r;D)) + V_{\mathrm{p}}^{\mathrm{I}}(x(r;D))\right\}\Phi(r;D) = \varepsilon(D)\Phi(r;D), \tag{1}$$

where $\Phi(0;D) = 0$. A set of discrete eigen-energies ε are obtained by solving Equation (1) in a finite radial coordinate range, $r \in [0, R]$, under some boundary conditions of Φ at $r = R$. The eigen-energies separate into energy levels of the atomic hydrogen and discretized energy levels of the conduction electrons at large D values. On the other hand, near the surface, the atomic levels are broadened as well as shifted by the surface potentials. Energy width of the broadening is proportional inversely to life time of the atomic state, and represents degree of the electron transfer between the atomic site and the surface site. To calculate the energy width of the broadening, the outgoing wave boundary condition is

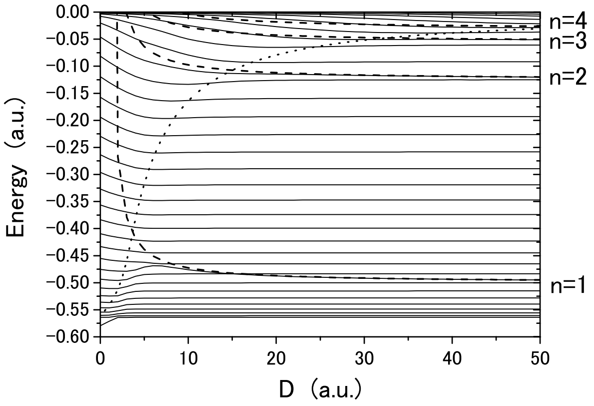

Figure 3 (a): Eigen-energy for tungsten surface (110) as a function of D. Solid curves are the eigen-energies, dashed curves atomic hydrogen levels shifted by the classical image potential, and dotted curve top of the potential ridge (see Figure 2).

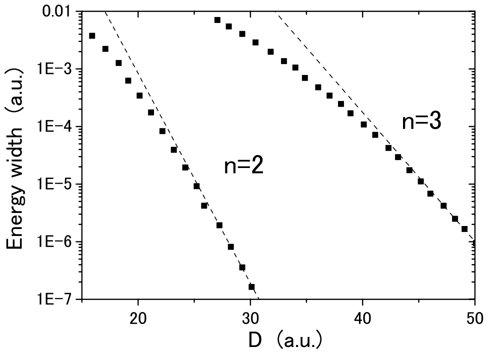

Figure 3 (b): Level broadening of atomic hydrogen above tungsten surface (110) as a function of D. Dotted lines are fitting to exponential functions of D.

imposed to the electronic wave function, $\left(d/dr - ik\right)\Phi\big|_{r=R} = 0$, where $k = \sqrt{2\varepsilon}$ measured from V_{e}^{1} in the bulk of the metal. As a result, the Hamiltonian matrix of Equation (1) becomes quadratic of k. It is transformed to the linear non-Hermitian matrix equation of k [7], and solved numerically using the discrete-variable representation [8] of the Jacobi-polynomial. The imaginary part of $-k^2$ is the energy width. Figure 3 shows the calculated eigen-energies and the level broadening of the atomic hydrogen as a function of D for the tungsten surface.

Proton motion is described by classical trajectories as the de Broglie wavelength is much shorter than the atomic scale for proton energies considered here (> 100 eV). The excited hydrogen atoms disappear immediately once they dive into the conduction electron gas of the metal due to the strong screening effect. Thus, only outgoing part of the trajectory is relevant to the excited hydrogen atoms emitted from the surface. For simplicity, we use the straight line trajectory normal to the surface. Velocity change of the proton due to the image force and electronic transition is omitted, since it may be not significant for the proton energies considered here.

At the initial time t_0, the proton is placed just above the surface with a small distance of D_0, and then recedes from the surface with a constant velocity of $v < 0$. The initial electronic state of the hydrogen-tungsten system is assumed to be in the ground state: All electronic levels below the Fermi level of the tungsten (about -0.19 a.u.) are equally occupied, while higher levels are empty. The random phase approximation is applied for the wave function of the initial state. The wave function multiplied by a kinematical factor is propagated numerically in the time domain using the split-operator spectral method [9],

$$\begin{aligned}\Psi(r,t_0) &= \exp\left[-ivx + i\,v^2/2t_0\right]\sum_k \Phi_k(r;D_0)\exp\left[i\sigma_k\right]\Theta(\varepsilon_{\mathrm{F}} - \varepsilon_k(D_0)),\\ \Psi(r,t) &= \exp\left[-i\int_{t_0}^{t}\hat{H}[D(t')]dt'\right]\Psi(r,t_0).\end{aligned} \tag{2}$$

At a sufficiently large D (after a long time), the occupation probabilities of the atomic levels are obtained by projecting $\Psi(t)$ on to $\Phi_k(D(t))$, whereas those of the conduction levels by projecting on to $\exp[-ivx + i\,v^2/2t]\Phi_k(D(t))$.

3. Results and Discussion

In this paper, we present calculations of the occupation probabilities due to the single electron capture by the receding proton from the tungsten slab whose width is about 100 a.u. (about 50 Å). Figure 4 (a) shows the occupation probabilities of the excited levels of the atomic hydrogen as a function of the proton velocity. They are normalized to that of the ground level. At low proton velocities, the relative probabilities are vanishingly small. At those velocities, the electronic state of every eigen-energy curve changes adiabatically along the same curve as D varies. The eigen-energy curves associated with the excited states of the atomic hydrogen at large D are above the Fermi level of the tungsten for all the D values (see Figure 3 (a)). Thus, the excited levels are hardly occupied at the low velocities. As the velocity increases, the probabilities grow significantly. It indicates that the non-adiabatic transition of the electronic state among the different eigen-energy curves takes place. However, it is clear from Figure 3 (a) that there is no apparent avoided-crossing of the

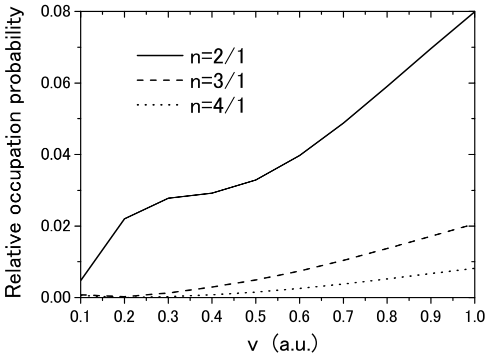

Figure 4 (a): Occupation probability of excited levels of atomic hydrogen emitted from tungsten surface (110).

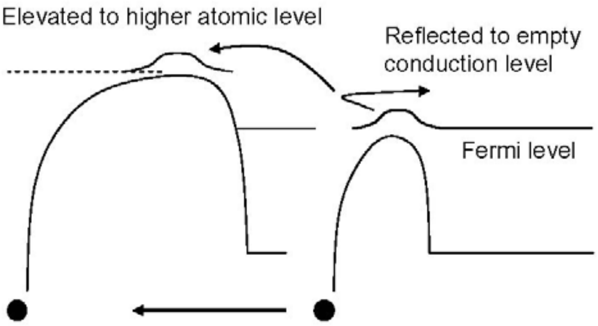

Figure 4 (b): Non-adiabatic electron capture by receding proton from metal surface.

eigen-energy curves to explain the non-adiabatic transition. The mechanism of the non-adiabatic electron capture is described in Figure 4 (b). Near the surface, top of the potential ridge lying between the proton and the surface dives below the Fermi level. As the proton recedes from the surface, the top rises out of the Fermi level. Faster the proton recedes from the surface, more the electronic wave function is kept sitting astride of the potential ridge and elevated to the higher atomic level. It may be explained as promotion through a series of hidden-crossings [10] of the eigen-energy surface on the *complex* D plane; projection of the hidden-crossings on to the real D axis may be drawn along the top of the potential ridge as shown in Figure 3 (a).

A hump is seen in the n=2 occupation probability at low velocities. It may be attributed to the oscillatory transition between quasi-resonant states of the n=2 level and a discrete conduction level of the metal slab. At the low proton velocity, the electron has an ample time to jump back and forth between the atomic level and the discrete conduction level before the proton gets out from the interaction region. With the larger slab width (the higher number density of the conduction levels), the hump becomes less significant. For the semi-infinite metal, the hump should disappear after the transition amplitude is integrated over the continuous conduction levels around the atomic level (bandwidth effect).

As a concluding remark, it is noted that the present model is based upon the dispersion relation of the quasi-free electron gas. Its density of state is very different from that of the tungsten (transition metal). An improved model taking account of a realistic density of state is under development.

Acknowledgment

The authors thank to Prof. R. Janev and Prof. R. More for fruitful discussions. D. K. is grateful to all organizers of the China-Japan Symposium on Atomic and Molecular Processes in Plasma for their hospitality.

References

[1] For example, D. Field, Astron. Astrophys. 362 (2000) 774.

[2] T. Tanabe, K. Ohya, and N. Otsuki, J. Nucl. Mater. 220-222 (1995) 841.

[3] R. Brako and D. M. Newns, Rep. Prog. Phys. 52 (1989) 655.

[4] J. Burgdörfer, E. Kupfer, and H. Gabriel, Phys. Rev. A 35 (1987) 466.

[5] P. J. Jennings, R. O. Jones, and M. Weinert, Phys. Rev. B 37 (1988) 6113.

[6] A. G. Eguiluz, Phys. Rev. B 31 (1985) 3303.

[7] O. I. Tolstikhin, V. N. Ostrovsky, and H. Nakamura, Phys. Rev. A 58 (1998) 2077.

[8] J. C. Light, I. P. Hamilton, and J. V. Lill, J. Chem. Phys. 82 (1985) 1400.

[9] M. R. Hermann and J. A. Fleck, Jr., Phys. Rev. A 38 (1988) 6000.

[10] S. Yu. Ovchinnikov and E. A. Solov’ev, Comments At. Mol. Phys. 22 (1988) 69.

SPECTROSCOPIC STUDY OF IONS TRANSMITTED THROUGH A MICROCAPILLARY

Y. Kanai,[a] Y. Iwai,[a] Y. Morishita,[a,*] and Y. Yamazaki [a,b]

[a] Atomic Physics Laboratory, RIKEN, Wako, Saitama 351-0198, Japan
[b] Institute of Physics, Graduate School of Arts and Sciences, University of Tokyo,
Meguro, Tokyo 153-8902, Japan

ABSTRACT

The formation and relaxation processes of hollow atoms and related excited states of ions produced with a Ni microcappillary thin foil have been studied employing various experimental techniques. The initial population of first transfer electron from the surface to the ions was studied by using visible light measurements. On the other hand, X-ray measurements revealed the core electronic configurations of ions at the last moment of the hollow atom evolution.

Keywords: Hollow atoms, Microcapillary, Slow highly charged ions

1 Introduction

When a highly charged ion (HCI) approaches a solid surface, the ion is accelerated toward the surface with its image charge and then the ion resonantly captures target electrons into excited states. Such an atom (ion) with multiply excited electrons and inner shell vacancies is called a "hollow atom (ion)" [1-11]. Although the formation and relaxation dynamics of hollow atoms have been studied in recent years with a flat surface target, not enough information on the electronic configurations of the hollow atom has been available so far. This is because its intrinsic lifetime could be longer than the time interval (*i.e.* ~10^{-13} s) between the hollow atom formation above the surface and its arrival at the surface. To overcome the difficulty, hollow atoms (ions) were extracted in vacuum employing a microcapillary target [12-20, 22-27]. The microcapillary used in our experiments was ~1mm^2 in size with a thickness of ~ μm and had a multitude of a straight holes of ~ 100 nm in diameter. When HCIs impinge on the microcapillary target parallel to the capillary axis, part of the hollow atoms (ions) formed in the capillary can pass through it before hitting the capillary wall. In this case, free hollow atoms are extracted in vacuum. We have used free hollow atoms to study

---

* present address: National Metrology Institute of Japan, AIST, Tsukuba 305-8567, Japan

its production and relaxation mechanisms employing the following techniques [20]: (1) Visible light measurements, which give information on Rydberg states produced by the charge transfer from the capillary surface[17,23,27], (2) X-ray measurements in coincidence with the final charge states, which reveal the lifetime of inner shell hole(s) for different number of electrons transferred[14,15,16], and (3) X-ray measurements with a high-resolution grating spectrometer, which allows one to identify the core electronic configurations of hollow atoms[24,25,26], and (4) charge state and scattering angle measurements, which are expected to reflect the distance between the ion and the surface at the moment of the charge transfer[25]. In this paper, we review our experimental results by using spectroscopic techniques; visible light measurements and high-resolution X-ray measurements

2 Visible light measurements

As mentioned in the introduction, when a HCI approaches to a solid surface, electrons from the valence band of the solid are resonantly transferred to highly excited states of the ion. According to the classical over barrier (COB) model [1, 21], the first electron transfer takes place to

$$n_c \sim Q_{in}/\,[2W(1+(Q_{in}-0.5)/(8Q_{in})^{1/2})]^{1/2}$$

of the incident ion, where Q_{in} is the charge of the ion and W is the work function of the target (physical quantities are given in atomic units unless otherwise noted) [21]. Adapting 0.191 a.u. for Ni work function W, n_c is estimated to be $Q_{in}+1.3$. Those atoms (ions) may emit visible light via transitions among highly excited states. In order to see what really happens, visible light emitted from the ions transmitted through a Ni capillary were measured with a Czerny-Turner type spectrometer with 1 to 1 imaging mirrors. Spectra for 2.0 keV/u Ar^{Qin+} ($6 \le Q_{in} \le 10$) ions are shown in Fig. 1 [17, 22, 23, 27]. Almost all lines are attributed to $\Delta n = 1$ transitions of the ions which have captured an electron into a high Rydberg state, the transition wavelengths of which can be well accounted for by assuming energy levels as those of hydrogen-like ions as shown in Table 1.

It is noted that the line observed for Ar^{Qin+} incident ions can also be observed at the same wavelength, in the present spectral resolution, for $\mathrm{Ar}^{(Qin+1)+}$ ($\mathrm{Ar}^{(Qin+2)+}$) incident ions, which is labeled by primed letters like i' (i'') in Fig. 1. This indicates that $\mathrm{Ar}^{(Qin+1)+}$ ($\mathrm{Ar}^{(Qin+2)+}$) ion has captured many electrons in the capillary, and de-excited through radiative or Auger transitions leaving one electron in its high Rydberg states.

We have also measured the decay curve of each emission line for Ar^{7+} and Ar^{8+} incident ions with high resolution to get detailed information of initial (n, l) distribution of the first transferred electron [23]. We solved the rate equation for each (n, l) state to reproduce the observed decay curves taking into account the cascade filling processes with n as high as Q_{in}+ 4, and obtained the initial (n, l) distributions. These initial (n, l) distributions have following features; (1) the mean value $< n >\sim Q_{in}+1.5$ and the width of $n \sim \pm 1$, which is consistent with the prediction of the COB model $n_c\sim Q_{in}+1.3$, and (2) for each n manifold, the higher angular momentum states are in general preferentially populated like in the statistical distribution rather than the flat (l independent) distribution [23].

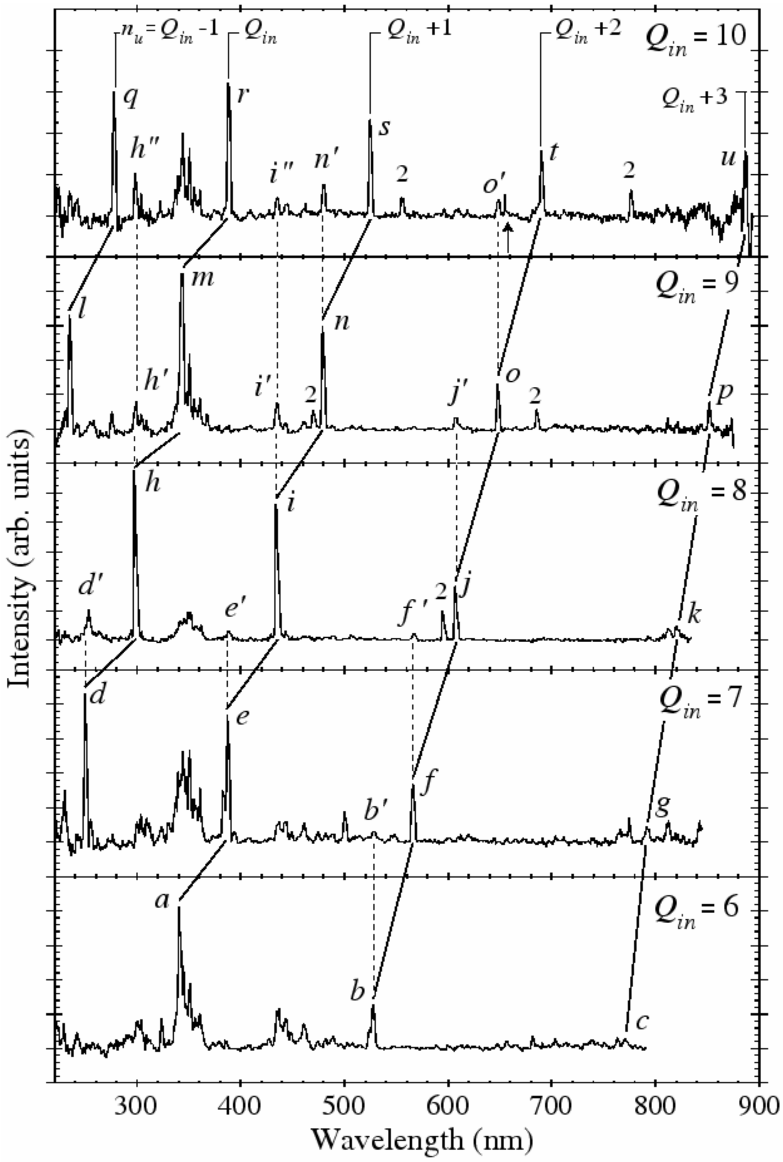

Figure 1. Spectra observed with 2.0 keV/amu Ar^{Qin+} ions ($6 \leq Q_{in} \leq 10$). The ordinate of each spectrum is proportional to the number of the emitted photons. Lines labeled by alphabetical letters are identified as $\Delta n = 1$ transitions, and transitions represented as principal quantum numbers of upper states $n_u = Q_{in} + s$ ($-1 \leq s \leq 3$) are connected with the solid lines. Lines labeled by dashed letters indicate transitions after multiple electron capture, which are connected by dashed lines. Lines labeled by 2 represent the second order diffraction. Broad bump around 300-360 nm for all incident charges are attributed to the emissions from sputtered Ni atoms

Q_{in}	n_u	E_{n_u}- $E_{n_{u-1}}$(nm)	Observed wavelength (nm)	
11	11	434	436.0 ± 2.0	*w*
	10	321	323.8 ± 2.0	*v*
10	13	887	887.0 ± 2.0	*u*
	12	690	690.5 ± 2.0	*t*
	11	525	525.0 ± 2.0	*s*
	10	388	389.0 ± 2.0	*r*
	9	278	278.0 ± 2.0	*q*
9	12	852	852.0 ± 2.0	*p*
	11	648	648.0 ± 2.0	*o*
	10	480	479.5 ± 2.0	*n*
	9	343	343.0 ± 2.0	*m*
	8	235	235.0 ± 2.0	*l*
8	11	820	821.0 ± 2.0	*k*
	10	607	607.5 ± 2.0	*j*
	9	434	435.5 ± 2.0	*i*
	8	298	299.0 ± 2.0	*h*
7	10	793	792.0 ± 2.0	*g*
	9	567	566.0 ± 2.0	*f*
	8	389	388.0 ± 2.0	*e*
	7	252	250.0 ± 2.0	*d*
6	9	772	771.0 ± 2.0	*c*
	8	529	528.0 ± 2.0	*b*
	7	343	341.5 ± 2.0	*a*

Table 1. Δn = 1 transition wavelengths calculated assuming energy levels as hydrogen-like and observed wavelengths. The last column shows the letters in Fig.1.

3 High resolution X-ray measurements

To identify the electronic configurations involved in the X-ray emission is very important to understand the dynamics of the hollow atom relaxation processes. In order to obtain enough energy-resolution to identify the electronic configurations, we developed a high-resolution soft X-ray spectrometer, which consists of a grating with varied groove spacing and a back-illuminated CCD (charged couples device) [24]. The K X-ray spectra taken with the spectrometer for 2.3 keV/u N^{7+} and N^{6+} ions transmitted through the Ni capillary are shown in Figs. 2 and 3, respectively. All sharp lines are identified as shown in Tables 2 and 3. The small peak at 489.6 ± 0.5 eV in Fig. 2 may be attributed to the $2p^2$ ^3P-$1s2p$ ^3P transition, which is the Auger forbidden transition.

According to the result of the visible light spectroscopy as mentioned in section 2, the principal quantum numbers of the initially populated states are $n_c \sim Q_{in}+1.5$, which are ~ 8.5 and 7.5 for N^{7+} and N^{6+} incident ions, respectively. In other words, the observed transitions (8p-1s) and ($1s8p$-$1s^2$) for N^{7+} and N^{6+} incident, respectively, are the transitions from the initially populated states. The populations of low *n* states may be produced by (1) the multiple electron capture followed by the Auger decays and/or (2) the one electron capture into high angular momentum state followed by the radiative cascades.

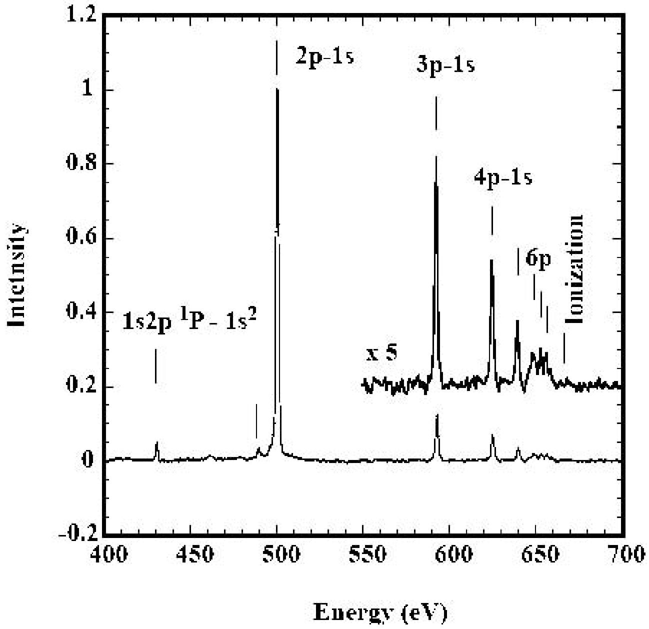

Figure 2. K X-ray spectra measured, immediately down stream of the target for 2.3 keV/amu $^{15}N^{7+}$ ions with a 25 μm entrance slit of the spectrometer [25]. Small peak at 489 eV may be attributed to $2p^2\ ^3P$-$1s2p\ ^3P$ transition

Obs. (eV)		Ref. (eV) [28]	Configurations
430.8	0.4	430.7	$1s2p$-$1s^2$
500.4	0.5	500.3	2p-1s
593.0	0.7	592.9	3p-1s
625.4	0.7	625.4	4p-1s
640.4	0.7	640.4	5p-1s
649.3	0.8	648.5	6p-1s
653.9	0.8	653.4	7p-1s
656.3	0.8	656.6	8p-1s
		667.1	ionization

Table 2. Observed line energies and configurations [25].

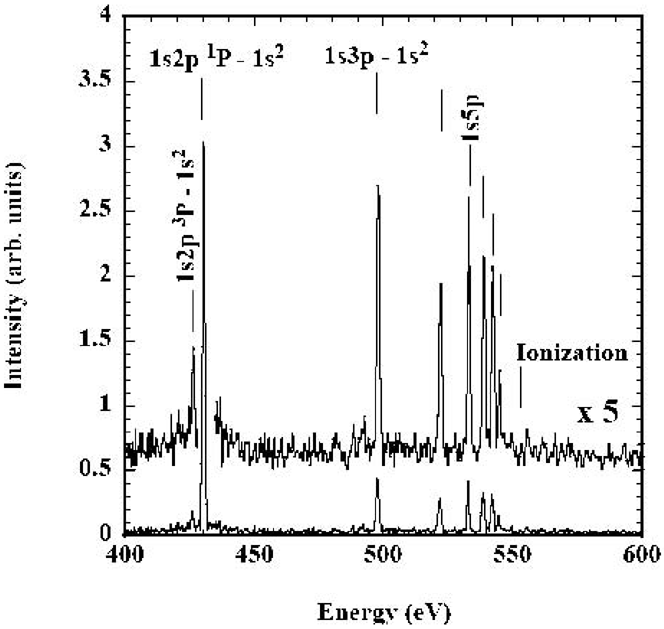

Figure 3. K X-ray spectra measured, immediately down stream of the target for 2.3 keV/amu N^{6+} ions with a 50 μm entrance slit of the spectrometer.

Obs.(eV)		Ref. (eV) [28]	Configurations
426.1	0.8	426.3	$1s2p\ ^3P_1$-$1s^2\ ^1S_0$
430.4	0.8	430.7	$1s2p\ ^1P_1$-$1s^2\ ^1S_0$
497.8	1.0	498.0	$1s3p\ ^1P_1$-$1s^2\ ^1S_0$
521.8	1.1	521.6	$1s4p\ ^1P_1$-$1s^2\ ^1S_0$
532.7	1.2	532.6	$1s5p\ ^1P_1$-$1s^2\ ^1S_0$
538.7	1.2	538.5	$1s6p\ ^1P_1$-$1s^2\ ^1S_0$
542.2	1.2	542.1	$1s7p\ ^1P_1$-$1s^2\ ^1S_0$
544.5	1.2	544.6	$1s8p\ ^1P_1$-$1s^2\ ^1S_0$
		552.1	ionization

Table 2. Observed line energies and configurations.

4 Summary

With visible light measurements, (1) we experimentally confirmed the prediction of the COB model; the first electron transfer takes place to $n_c \sim Q_{in}/\,[2W(1+(Q_{in}-0.5)/(8Q_{in})^{1/2})]^{1/2}$ of the incidence ion and (2)we obtained the evidence that multi electrons transfer into ions from the capillary and those ions are stabilized with one electron in the Rydberg state. High-resolution X-ray measurements reveal core electronic configurations of ions after the capillary at the moment of the X-ray emission.

Although we observed a small signal from the doubly excited state $N^{5+**}(2p^2\ {}^3P)$ with the high-resolution X-ray measurements, we have not enough information of electronic configurations of hollow atom. As the next step, we are planning to measure the electrons emitted by Auger processes, which is the main decay processes of hollow atom (ion) produced by multi electron capture.

References

[1] J. Burgdörfer, P. Lerner, F.W. Meyer, Phys. Rev. A **44** (1991) 5674.
[2] J.P. Briand et al., Phys. Rev. Lett. **65** (1990) 159.
[3] H. J. Andrá et al., Z. Phys. D**21** (1991) S135.
[4] H. Winter, Europhys. Lett, **18** (1992) 207.
[5] F. Aumayr et al., Phys. Rev. Lett. **71** (1993)1943.
[6] F.W. Meyer et al., Phys. Rev. Lett. **67** (1991) 723.
[7] J. Das, R. Morgenstern, Phys. Rev. A. **47** (1993) R755.
[8] R. Köhrbrück et al., Phys. Rev. A **50** (1994) 1429.
[9] L. Folkerts et al., Phys. Rev. Lett. **74** (1995) 2204.
[10] K. Kakutani et al., Jpn J. Appl. Phys. **34** (1995) L580.
[11] T. Neidhart et al., Phys. Rev. Lett. **74** (1995) 5280.
[12] H. Masuda, K. Fukuda, Science **268** (1995) 1466.
[13] H. Masuda, M. Satoh, Jpn J. Appl. Phys. **35** (1996) L126.
[14] Y. Yamazaki et al., J. Phys. Soc. Jpn. **65** (1996) 1199.
[15] S. Ninomiya et al., Phys. Rev. Lett. **78** (1997) 4557.
[16] S. Ninomiya et al., Physica Scripta T**73** (1997) 316.
[17] Y. Morishita et al., Physica Scripta T**80** (1999) 212.
[18] Y. Yamazaki. Physica Scripta T**73** (1997) 293.
[19] Y. Yamazaki, Int. J. Mass Spectrometry **192** (1999) 437.
[20] Y. Kanai et al., Nucl. Instr. and Meth. **B182** (2001)174.
[21] J. Burgdörfer, in: Review of Fundamental Processes and Applications of Atoms and Ions, ed. C.D. Lin (World Scientific, Singapore, 1993) p. 517.
[22] H.A. Torii et al., RIKEN Review **31** (2000) 30.
[23] Y. Morishita et al., to be published in Phys. Rev. **A** (2004).
[24] Y. Iwai et al., RIKEN Review **31** (2000) 34.
[25] Y. Iwai et al. Nucl. Instr. and Meth. **B193** (2002)504.
[26] Y. Iwai et al., Nucl. Instr. and Meth. **B205** (2003)762.
[27] Y. Morishita et al., Nucl. Instr. and Meth. **B205** (2003)758.
[28] R.L. Kelly, J. Phys. Chem. Ref. Data, **16** Supple. 1 (1987).

Electron transfer and decay processes of highly charged iodine ions

Hiroyuki A. Sakaue, Atsunori Danjo [1], Kazumoto Hosaka [2], Daiji Kato, Masahiro Kimura [3],
Atsushi Matsumoto [4], Nobuyuki Nakamura [5], Shunsuke Ohtani [5], Makoto Sakurai [6],
Hiroyuki Tawara [7], Ichihiro Yamada and Masuhiro Yoshino [8]

National Institute for Fusion Science, Toki 509-5292, Japan
1) Department of Environmental Science, Niigata University, Niigata 950-2181, Japan
2) National Physical Laboratory, Teddington, TW11 OLW, United Kingdom
3) Kochi University of Technology, Kochi 782-8502, Japan
4) Hiroshima Institute of Technology, Hiroshima 731-5193, Japan
5) The University of Electro-Communications, Chofu 182-8585, Japan
6) Department of Physics, Kobe University, Kobe 657-8501, Japan
7) Max Planck Institute for Nuclear Physics, Saupfercheckweg 1, D-69117, Germany
8) Shibaura Institute of Technology, Saitama 337-8570, Japan

Abstract

In the present experimental work we have investigated multi-electron transfer processes in I^{q+} (q=10, 15, 20 and 25) + Ne, Ar, Kr and Xe collisions at 1.5q keV energy. The branching ratios between Auger and radiative decay channels have been measured in decay processes of multiply excited states formed by multi-electron transfer collisions. It has been shown that, in all the multi-electron transfer processes investigated, the Auger decays are far dominant over the radiative decay processes and the branching ratios are clearly characterized by the average principal quantum number $<n>$ of the initial excited states of projectile ions. We could express the branching ratios in high Rydberg states formed in multi-electron transfer processes by using the decay probability of one Auger electron emission.

Keywords: highly charged ion, charge transfer, Auger decay

1. Introduction

To date, multiple electron capture processes in collisions of highly charged ions (HCIs) A^{q+} with atoms B have been widely studied [1]. The electron capture cross sections in HCIs-atom collisions have been understood reasonably well through the classical over-barrier model [2, 3, 4, 5], also the energy deposition model has been used successfully to apply the observed Auger decay processes and multiple ionization processes [6, 7, 8]. Recent activities on those studies are reviewed by Cederquist [9]. Such collisions generally produce multiply excited states

$\mathrm{A}^{(q-j)+**\cdots}(n,n',\cdots)$, which in turn are stabilized through emissions of electron(s) and photon(s): $\mathrm{A}^{q+} + \mathrm{B} \to \mathrm{A}^{(q-j)+**\cdots}(n,n',\cdots) + \mathrm{B}^{j+}$

$$\to \mathrm{A}^{(q-i)+} + \mathrm{B}^{j+} + (j-i)\mathrm{e}^{-} + h\nu + h\nu' + \cdots$$

where q represents the charge of the incident projectile ion, j the number of the electrons initially transferred into the ion from target atom during the collision, and i the final charge change of the incident ion after stabilization and $(n,n',\cdots)$ shows the principal quantum numbers of the electron transferred states. Since various combinations of j and i are possible, multiple electron capture processes are so complicated that systematic investigations are needed for the detailed understanding.

In the present study, the previous work has been extended to still higher q to investigate the stabilization processes of higher excited states. In general, the electron transferred levels become higher as the charge of the incident ion increases. We discuss the branching ratios of decay processes as a function of the average principal quantum number "$<n>$" of the electron transferred levels.

2. Branching ratios of decay processes

We consider the following multiple electron capture processes in highly charged iodine ion (q=10, 15, 20 and 25) – rare gas atom (Ne, Ar, Kr and Xe) collisions:

$$\mathrm{I}^{q+} + \mathrm{B} \to \mathrm{I}^{(q-i)+} + \mathrm{B}^{j+} + (j-i)\mathrm{e}^{-} + \sum h\nu + Q$$

Q is the translational energy gain in the collision, and $\sum$ represents the cascade photon emissions. It is convenient to discuss the electron capture processes by dividing into the following two steps.

I) j-electron transfer process:

$$\mathrm{I}^{q+} + \mathrm{B} \to \mathrm{I}^{(q-j)+**\cdots}(n,n',\cdots) + \mathrm{B}^{j+} + Q$$

where $n,n',\cdots$ are the principal quantum numbers of the electronic states produced in this process.

II) Decay process of the excited product ion:

$$\mathrm{I}^{(q-j)+**\cdots}(n,n',\cdots) \to \mathrm{I}^{(q-i)+} + (j-i)\mathrm{e}^{-} + \sum h\nu.$$

In this paper, we discuss the branching ratios of the above decay processes II) in multiply excited product ions. We have determined the branching ratios in the decay of multiply-excited ions from the coincidence measurement of the scattered and recoil ions. The present experimental apparatus and method were the same as those used in the previous work [10, 11]. The branching ratios *P(j,j-i)* in the decay of multiply-excited ions by emission of (*j-i*) electrons after *j*-electron transfer is defined by:

$$P(j, j-i) = \frac{\sigma^{j}_{q,q-i}}{\sum_{i} \sigma^{j}_{q,q-i}} = \frac{\sigma^{j}_{q,q-i}}{\sigma^{j}_{q}}$$

where $\sigma^{j}_{q,q-i}$ is i-electron capture and j-electron removal cross section, and σ^{j}_{q} is j-electron removal cross section.

We also assume that the Auger decay rates of multiply-excited states with high *n*-values do not depend strongly on the ion charge, but the number of Auger processes depends on the number of the decay channels from the excited states. Since the number of decay channels is related to the degree of the *n*-value, the probability of the decay process with *j*-electrons transferred can be expressed by using the following average value <*n*> of all *j* electrons: $<n>=(n_1+n_2+\ldots+n_j)/j$. Here n_j represents the principal quantum number of the *j*-th electron transferred which can be estimated from the extended classical-over-barrier-model (ECBM) [12].

Figure 1, 2 and 3 show one of the possible arrangements for the relationship between the branching ratios and the average principal quantum number <*n*>. Here, we plot the measured branching ratios as a function of $-1/<n>^2$, where <*n*> is the value calculated with the ECBM for each *j*-electron transfer process. Here we also show the calculated threshold values n_{thre} of the energetically allowed Auger decay processes for the respective branching ratio *P(j,j-i)*. The solid and dotted lines are drawn to guide the eyes, they show the general dependence of the branching ratios on the <*n*>-values. In drawing these lines, we take the following simple principles into account: 1) the *P(j,j-i)* branching ratio is zero when the average transfer levels <*n*> are lower than the threshold levels n_{thre} and 2) the sum of the branching ratios equals to 1.0.

A) Doubly-excited states

In the doubly-excited states (figure 1), we can place the branching ratio of the radiative decay to be 1.0 when the average transfer levels <*n*> are lower than $n_{thre} \cong 5.7$ which corresponds to the threshold levels for the *P(2,1)* processes. On the other hand, as

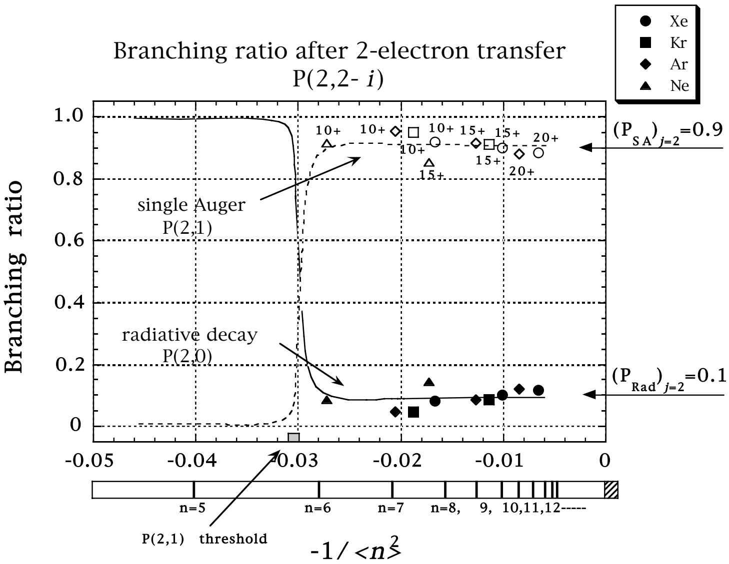

Figure 1. $-1/<n>^2$ dependence of the branching ratios after 2-electron transfer : P(2,2-i). n is the principal quantum number of the transferring excited levels calculated by ECBM

q becomes higher, the highly charged ions capture electrons into higher excitation levels than the threshold ($n_{thre} \cong 5.7$), where the Auger decay becomes energetically possible. In these cases, the single Auger decay becomes dominant and the branching ratios show almost constant value. Actually as shown in our experimental results with charge state range of *q*=10~20, the branching ratio *P(2,1)* has been determined to be 0.9, while the branching ratio of radiative decay *P(2,0)* is about 0.1, indicating that the radiative decay rate is much smaller than the Auger decay rate.

B) Triply-excited states

In the triply-excited states (figure 2), when three electrons are bound to the comparatively deep inner shells ($5.3 \leq \langle n \rangle \leq 6$) of the ion, the excited states of ions decay dominantly by emitting one electron. However, when the electrons are transferred to levels higher than the *P(3,2)* threshold level ($n_{thre} \cong 6$), the single Auger decay processes start to decrease, and instead the double Auger decay processes start to increase gradually. When the three electrons are transferred to higher excited states ($\langle n \rangle \geq 8$), the fraction of the double Auger decay reaches up to about 0.8. Finally all of the branching ratios (*P(3,0)*, *P(3,1)* and *P(3,2)*) keeps roughly constant in high <*n*> region, where the radiative decay processes almost disappear and the Auger decay processes become dominant.

C) Quadruply-excited states

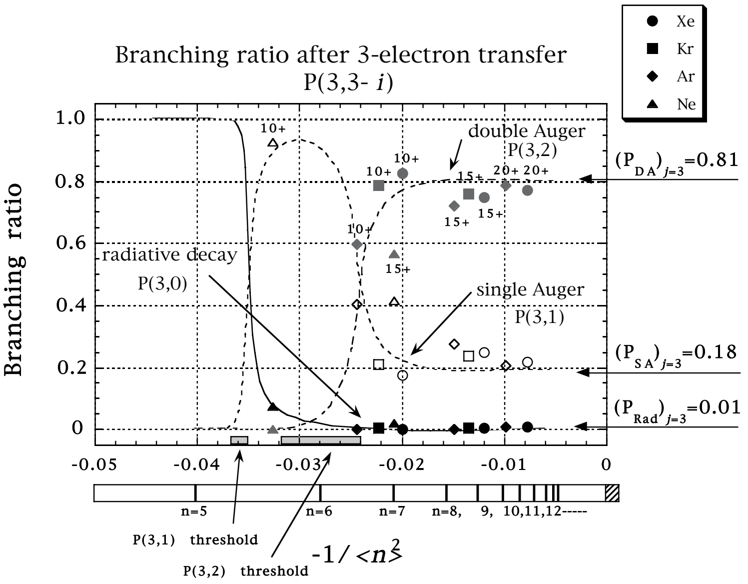

Figure 2. $-1/\langle n \rangle^2$ dependence of the branching ratios after 3-electron transfer : P(3,3-i).

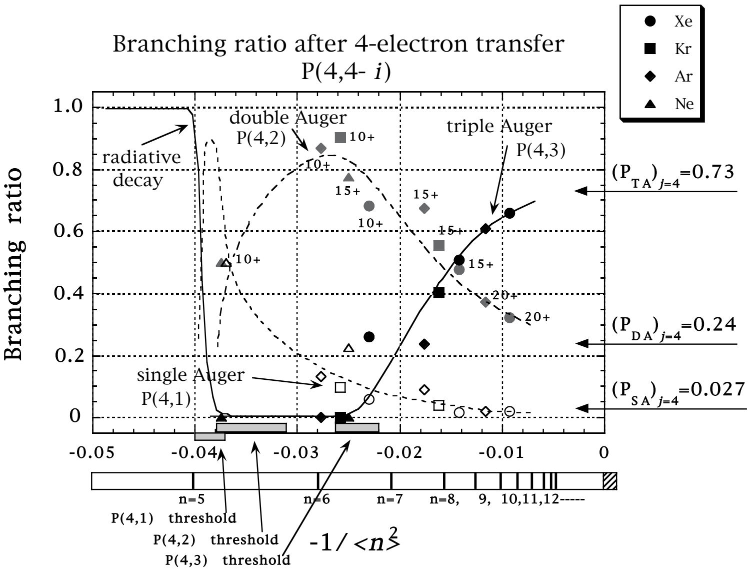

Figure 3. $-1/\langle n \rangle^2$ dependence of the branching ratios after 4-electron transfer : P(4,4-i).

Similarly, in the quadruply-excited states (figure 3), the double Auger decay processes increase as the single Auger decay processes decrease at $<n> \cong 5.3$ and afterwards become dominant at $<n> \cong 6$. The triple Auger decay channel is opened at $<n> \cong 6.3$, the threshold for *P(4,3)*. The ratios of double and triple Auger decays are turned inversely near $<n> \cong 8$. If the four electrons are transferred into still higher excited states ($<n> \geq 11$), the triple Auger decay channels become dominant and the *P(4,3)* approaches to about 0.7.

Through the above arrangements of experimental data, we have summarized the general feature in the decay processes from the multiply-excited states produced by many-electron transfer collisions. When electrons are transferred to higher levels than the threshold $<n_{thre}>$, the Auger decay dominates rather than the radiative decay. Then as the transferred levels go up higher $<n>$, the Auger decay with more than one electron emissions becomes favorable. Finally, all of the branching ratios for radiative and Auger decay processes take constant values as an asymptotic characteristics with high $<n>$.

We will discuss the observed systematic behavior for the decay processes of highly excited ions with multi-Rydberg electrons. At first, we define R_{Auger} as the decay probability with single Auger electron emission and R_{rad} as the radiative decay probability, respectively, from sufficiently high $<n>$ levels produced by the multi-electron transfer, where $R_{Auger} + R_{rad} = 1$. For the doubly-excited states with $<n>$ higher than the threshold level n_{thre}=5.7, the branching ratios, *P(2,1)* and *P(2,0)* become constant and are 0.9 and 0.1, respectively, as shown in figure 1. Therefore, the R_{Auger} corresponds to the asymptotic value of the branching ratio for the single Auger electron decay from the doubly-excited state produced by two-electron transfer (j=2) collision: $(P_{SA})_{j=2}$ = *P(2,1)*, and the R_{rad} also corresponds to the branching ratio for the radiative decay: $(P_{rad})_{j=2}$ = *P(2,0)*, which are determined experimentally as follows:

$$(P_{SA})_{j=2} = R_{Auger} = 0.9, \quad (P_{rad})_{j=2} = R_{rad} = 0.1.$$

In three and four-electron transfer collisions, triply- and quadruply-excited states can be produced, which may decay radiatively and ejecting two or three electrons. Here, we make assumptions that, for the multiply-excited states with asymptotically high $<n>$, the successive Auger decay processes are favorable, which take place successively with combination of cascading single Auger processes, whose probabilities are nearly the same because the multi-electrons still remain in high Rydberg states after the first and the succeeding Auger decay processes. On the other hand, we suppose that the multi-Auger decay processes ejecting correlated two or three electrons simultaneously is negligible.

Next, we discuss the decay processes from the triply-excited states with high $<n>$. There are three possible processes with own branching ratios, 1) the successive double Auger decay:

$(P_{DA})_{j=3}$, 2) the combination of single Auger and radiative decay: $(P_{SA})_{j=3}$ and 3) the combination of two pure radiative decay: $(P_{rad})_{j=3}$. Based on the above assumptions, the respective branching ratios are expressed as follows:

$$(P_{DA})_{j=3} = (R_{Auger})^2,$$

$$(P_{SA})_{j=3} = 2\times R_{Auger}\times R_{rad} = 2\times R_{Auger}\times(1- R_{Auger}),$$

$$(P_{rad})_{j=3} = (R_{rad})^2=(1- R_{Auger})^2.$$

As the asymptotic value of R_{Auger} has been found to be 0.9 from our experiment, the above branching rations are calculated to be $(P_{DA})_{j=3}= 0.81$, $(P_{SA})_{j=3}= 0.18$ and $(P_{rad})_{j=3}= 0.01$. These values are shown in figure 2 with horizontal arrows. The calculated branching ratios are in good agreement with the asymptotic values in the observations, as seen in figure 2, for three-electron transfer processes.

By extending similar discussion to the decay processes from the quadruply-excited states, the branching ratios of the stabilization probabilities with the triple, double, single Auger and pure radiative decay can be described as follows:

$$(P_{TA})_{j=4} = (R_{Auger})^3,$$

$$(P_{DA})_{j=4} = 3\times(R_{Auger})^2\times R_{rad} = 3\times(R_{Auger})^2\times(1- R_{Auger}),$$

$$(P_{SA})_{j=4} = 3\times R_{Auger}\times(R_{rad})^2 = 3\times R_{Auger}\times(1- R_{Auger})^2,$$

$$(P_{rad})_{j=4} = (R_{rad})^3 = (1- R_{Auger})^3.$$

The calculated values are $(P_{TA})_{j=4}$=0.73, $(P_{DA})_{j=4}$=0.24, $(P_{SA})_{j=4}$=0.027 and $(P_{rad})_{j=4}$=0.001, respectively. These values are shown in figure 3 and again found to reproduce the observed values.

3. Conclusions.

The present observation of branching ratios suggests that the Auger decay processes after multiple electron transfer are characterized by the principal quantum number *n* of the transferred level and are nearly independent of the projectile ion charge *q* for *q*=10~20 range. Asymptotic characteristics of the branching ratios for the related decay modes are described as a combination of successive Auger processes, and well reproduced in terms of the probability determined in the observation of decay processes from the doubly-excited ions with asymptotically high Rydberg electrons. We have found that the branching ratios in high Rydberg states formed in multi-electron transfer processes can be expressed in terms of the decay probability (R_{Auger}) for one Auger electron emission.

References

[1] Barat M and Roncin P 1992 *J. Phys. B: At. Mol. Phys.* **25** 2205

[2] Ryufuku H and Sasaki K 1980 *Phys. Rev.* A **21** 745

[3] Mann R, Folkmann F and Beyer H K 1981 *J. Phys. B: At. Mol. Phys.* **14** 1161

[4] Mann R 1986 *Z. Phys. D* **3** 85

[5] Barany A and Hvelplund P 1987 *Nucl. Inst. Meth.* B **23** 40

[6] Russek A 1963 *Phys. Rev.* **132** 246

[7] Cock C L 1979 *Rhy. Rev.* A **20** 749

[8] Muller A, Groh W and Salzborn E 1983 *Phys. Rev. Lett.* **51** 107

[9] Cederquist H, Fardi A, Haghighat K, Langereis A, Schmidt H T and Schwartz S H 1999 *Phys. Scr.* T**80** 46

[10] Nakamura N, Currell F J, Danjo A, Kimura M, Matsumoto A, Ohtani S, Sakaue H A, Sakurai M, Tawara H, Watanabe H, Yamada I and Yoshino M 1995 *J. Phys. B: At. Mol. Opt. Phys.* **28** 2959

[11] Yamada I, Currell F J, Danjo A, Kimura M, Matsumoto A, Nakamura N, Ohtani S, Sakaue H A, Sakurai M, Tawara H, Watanabe H and Yoshino M 1995 *J. Phys. B: At. Mol. Opt. Phys.* **28** L9

[12] Niehaus A 1986 *J. Phys. B: At. Mol. Phys.* **19** 2925

SPECTROSCOPIC STUDY OF CHARGE TRANSFER IN COLLISIONS OF MULTI-CHARGED IONS

Hajime Tanuma

Department of Physics, Tokyo Metropolitan University,
1-1 Minami-Ohsawa, Hachioji, Tokyo 192-0397, Japan

ABSTRACT

Population distribution in magnetic sublevels of $1s^23p\ ^2P$ states of Li-like C, N, and O ions produced in collisions of He-like ions with gaseous targets has been obtained from the degree of polarization of the emission lines corresponding to the 3s-3p transitions. Dependence of the polarization degree upon the collision system has been discussed in view of the internuclear distance in which the electron transfer takes place during the collision.

The EUV (Extreme Ultra-Violet) spectra emitted from excited multiply charged Xe ions produced by charge transfer reactions have been observed in the wavelength range of 6- 24 nm to compare with the emission spectra from the laser or discharge plasmas. These spectra tell us the charge states of Xe ions for each EUV emission line from the Xe plasma.

keywords : multiply charged ion, charge transfer, polarization spectroscopy, EUV emission

1 Introduction

Charge transfer is the dominant inelastic-process in slow collisions of multiply charged ions with neutral atoms and molecules. This process, which is electron capture by multiply charged ions in other words, of considerable interest because it plays an important role in understanding the interaction of plasmas with cool gases and in diagnosing the fusion plasma. The detail mechanism of this reaction is extensively investigated both theoretically and experimentally as one of the most active research subjects in the atomic and molecular physics, because of its great importance in the development of X-ray laser and the astrophysical problem.

The single electron transfer reaction is represented by means of the following expression:

$$A^{q+} + B \rightarrow A^{(q-1)+}(nlm) + B \qquad (1)$$

where n, l, and m are the principle, azimuthal, and magnetic quantum numbers, respectively. It is one of important features of the electron capture by multiply charged ions that this reaction occurs with very strong state-selectivity, namely the captured electron populates quite limited numbers of electronic orbitals. For the single electron capture process, the n of the most dominant capture level can be predicted by the classical over-barrier (COB) model and is given by the following simple formula [1]:

$$n \approx \left(\frac{1 + 2\sqrt{q}}{2I\left(q + 2\sqrt{q}\right)} \right)^{\frac{1}{2}} q \tag{2}$$

where q is the charge state of the incident ion and I is the ionization potential of the neutral target in atomic units. This formula is derived for one-electron system, which consists of a fully stripped ion and a hydrogen atom. This theory, however, is extremely useful in understanding the electron capture processes, even in many electron systems, and also widely used in various related subjects after some modification [2].

The distribution of l states within a single n shell is difficult to predict by theory. In many cases, however, it can be measured with translational energy spectroscopy and photon emission spectroscopy, because the energy gaps between different l states larger than the energy resolution in each spectroscopic method. On the other hand, magnetic sublevels within a single nl state cannot be distinguished in energy by ordinary spectroscopic methods, because all energies of different magnetic sublevels are completely degenerate in the absence of a magnetic field. For single excited states, the measurement of the degree of polarization for photon emission is the only method for observing alignment which id determined by the distribution of m states. In the first part of this article, we report the experimental results on alignment of the $1s^2 3p$ states of Li-like ions produced by the single electron transfer in collisions of He-like ions, these are C^{4+}, N^{5+}, and O^{6+}, with several target gases.

Recently, much effort has been focused on the development of an EUV (Extreme Ultra-Violet) light source for next generation lithography. One of the candidates of the light source is a laser-produced plasma of xenon. However, the electronic structures of heavy atoms, like xenon, are very complicated because of the strong electron correlation and spin-orbit interaction. Hence, the energy levels of multiply charges xenon ions have not been established yet, even though much spectroscopic data has been reported [3]. Therefore spectroscopic information about multiply charged xenon ions is desired for modeling and optimization of the EUV light source. In the second part of this article, we present preliminary results on the EUV emission spectra from multiply charged Xe ions.

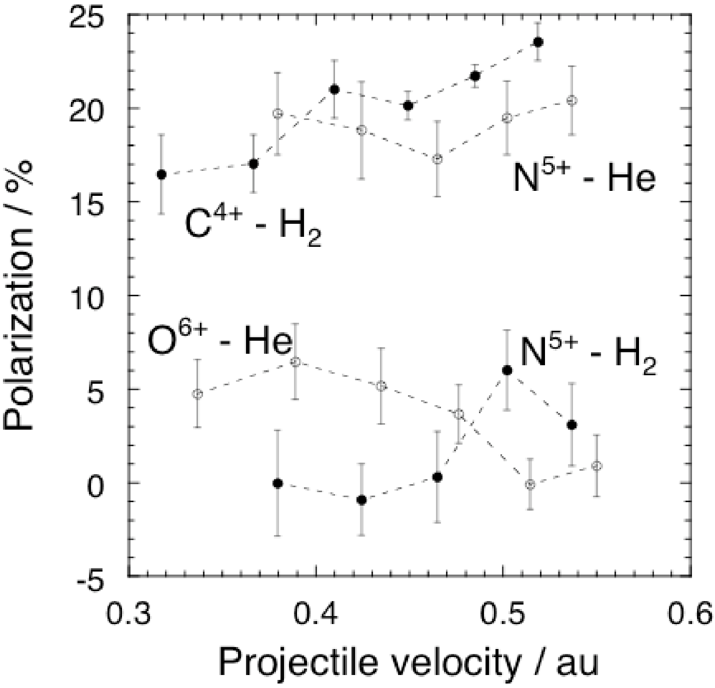

Figure 1. The degree of polarization for the line corresponding to the 3s $2^2S_{1/2}$ - 3p $^2P_{3/2}$ transition of excited Li-like ions produced by the single electron capture of He-like ions in collisions with two-electron targets as a function of projectile velocity in atomic units.

2 Polarization spectroscopy of Li-like ions

Since we are interested in the direct capture into the3p orbital, we chose the target gases which give the capture levels of *n* =3 according to prediction by the classical over-barrier model, namely H_2, Ar, Kr, and Xe for C^{4+}; He and H_2 for N^{5+}; and He for O^{6+}, respectively. In fact, the 3p states is directly populated by electron transfer and the cascades from upper states to 3p states can be neglected in the following collision systems, C^{4+} + H_2, N^{5+} + H_2, N^{5+} + He, and O^{6+} + He, according to the cross section measurements by means of the photon emission spectroscopy in the VUV region [4].

Multiply charged ions C^{4+}, N^{5+}, and O^{6+} are produced by a 14.25 GHz ECR (Electron Cyclotron Resonance) ion source from pure CH_4, N_2, and O_2 gas, respectively. The ion beams extracted at high potential of 7.5 - 20 kV from the source are analyzed with a magnet for the charge state separation. The beam of the selected He-like ions is directed into the collision chamber, where it intersects a target gas jet at the right angle. The optical radiation, emitted from the collision and passing through synthetic quartz windows and polarizers placed both sides of the chamber at the right angles to both the ion beam and the gas jet, is observed with a monochromator and a liquid nitrogen cooled CCD camera.

Figure 1 shows the degree of polarization for the emission line corresponding to the 3s $^2S_{1/2}$ - 3p $^2P_{3/2}$ transition of Li-like ions as a function of projectile velocity in atomic units for four collision systems with two-electron targets of He and H_2. Details of the measurement and analysis are shown in published articles [5-7]. As can be seen in this figure, no significant collision velocity dependence is seen in this velocity range for all systems. The results, however, classify the collision systems into two categories: In the cases of C^{4+}-H_2 and N^{5+}-He, the polarization degree has very large value around 20 %. The large polarization degree can be understood as a general characteristic of the electron transfer reaction in collisions of multiply charged ions with neutral targets, which had been reported for various collision systems [8]. On the other hand, the polarization degree has a very small value and is close to 0 % for the O^{6+}-He and N^{5+}-H_2 collisions. This finding is difficult to explain with a simple model.

As shown in Table 1, the crossing distances between the initial and final channels in diabatic potential curves of the collision systems shows the correlation with the degree of polarization. The crossing distance is estimated with the consideration of only the polarization interaction between the ion and the neutral in the initial channel and the Coulombic repulsion between ions in the final channel. In this table, we also show the strengths of the electric field at the potential crossing point by the residual target ion produced by the single electron transfer to the projectile ion, which the excited projectile ion feels just after the electron capture. As a highly probable cause of the small polarization degree in the O^{6+}-He and N^{5+}-H_2 systems, we are considering the mixing of different *nl* states through the linear Stark effect in strong electric fields by residual ions. The importance of this effect has been shown in the theoretical calculation by Salin [9].

As extension of the experiment, we have performed the similar measurements for the collisions of C^{4+} with rare gases, namely Ar, Kr, and Xe. The result with Ar target is very similar to that with H_2 target. However, Kr and Xe target cases are difficult to explain only with the Stark mixing model. Strong spin-orbit interaction in heavy atoms should be considered in these cases.

Table 1. Observed polarization degree, crossing distance in diabatic potential curves, and electric field strength at the crossing for each collision system.

Collision system	Polarization degree (%)	Crossing distance (Å)	Electric field (GV/m)
C^{4+} - H_2	16 - 24	4.7	6
N^{5+} - He	17 - 21	4.1	9
N^{5+} - H_2	0 - 7	2.8	18
O^{6+} - He	0 - 7	2.4	25

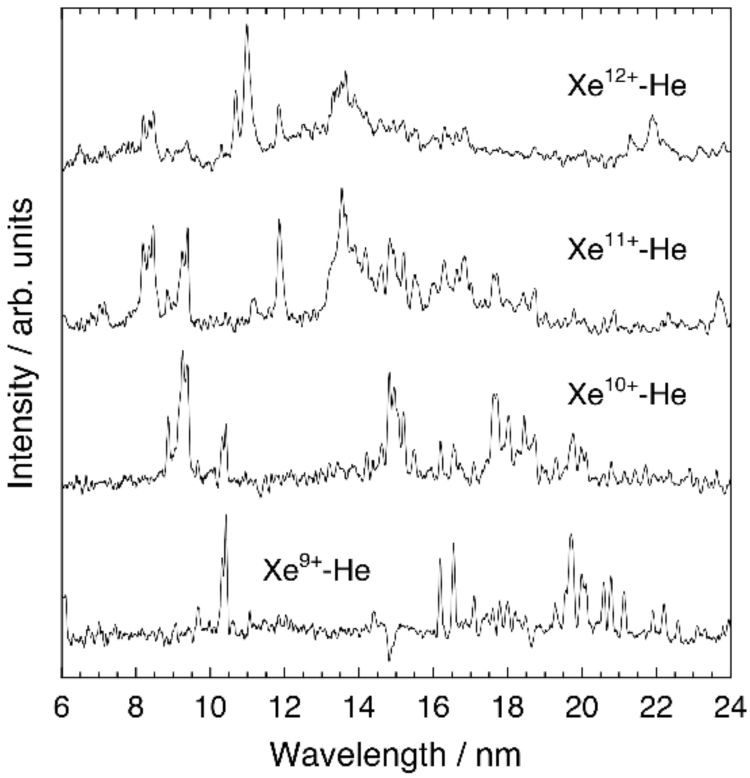

Figure 2. EUV spectra of radiation following electron capture by multiply charged Xe ions from He gas target.

3 EUV emission from charged selected Xe ions

We measured the photon emission from excited multiply charged Xe ions in the EUV region of 6 - 24 nm. The Xe ions produced from pure Xe gas in a 14.25 GHz ECR ion source at Tokyo Metropolitan University. The ions are extracted with an electric potential of 20 kV, selected in respect of their mass-to-charge ratio, and directed into a collision chamber, where the ion beam interacts a target gas jet. The EUV emission from the collision center is observed at 90° to the ion beam with a compact grazing incident spectrograph developed in Institute for Laser Engineering, Osaka University.

The EUV measurement has performed with the incident xenon ions Xe^{q+} of $q = 7$ - 13 and the target gas of He. For low charges of $q = 7$ and 8, Ar gas was used as the target, because no emission line was observed with He target. In order to calibrate the wavelength in our measurement system, the well-known EUV emission lines from $O^{5+}(1s^2l)$ and $O^{6+}(1sl)$ have been measured in the collisions of O^{6+} and O^{7+} ions with He target, respectively. Some preliminary EUV emission spectra are shown in Figure 2. Since the target-gas pressure was too high to maintain the single-collision conditions, some emission lines were observed in collisions of different charge states of the incident ions. Identifications of observed lines from Xe ions have not been finished yet, we have confirmed that emission lines around 13.5 nm, which should be used for the EUV lithography, are ascribed to Xe^{10+} ions.

Acknowledgement

This work became possible due to the contribution of graduate and undergraduate students, T. Hayakawa, A. Konnai, E. Shibuya, and T. Okuno (ILE, Osaka University) and due to the collaboration with Professors H. Nishimura (ILE) and K. Nishihara (ILE), and Professor Emeritus N. Kobayashi. A part of this work was financially supported in part by MEXT (Ministry of Education, Culture, Science and Technology, Japan) under contract subject "Leading Project for EUV lithography source development".

References

[1] H. Ryufuku, K. Sasaki, and T. Watanabe, Phys. Rev. A **21** (1980) 745.

[2] A. Niehaus, J. Phys. B **19** (1986) 2925.

[3] V. Kaufman, J. Sugar, and J.L. Tech, J. Opt. Soc. Am. **73** (1983) 691; J. Blackburn, P.K. Carroll, J. Costello, and G.O'Sullivan, J. Opt. Soc. Am. **73** (1983) 1325; S.S. Churilov and Y.N. Joshi, Phys. Scr. **65** (2002) 40 (2002); S. Churilov, Y.N. Joshi, and J. Reader, Opt. Lett. **28** (2003) 1478.

[4] D. Dijkkamp, D. Ciric, E. Vlieg, A. de Boer and F.J. de Heer, J. Phys. B **18** (1985) 4763.

[5] H. Tanuma, T. Hayakawa, C. Verzani, H. Kano, H. Watanabe, B. D. DePaola, and N. Kobayashi, J. Phys. B **33** (2000) 5091.

[6] T. Hayakawa, R. A. Lomsadze, C. Verzani, H. Watanabe, H. Tanuma, B. D. DePaola, and N. Kobayashi, Phys. Scripta **T92** (2001) 322.

[7] A. Konnai, H. Tanuma, and N. Kobayashi, Nucl. Instr. Meth. B **205** (2003) 586.

[8] *For example*, L.J. Lembo *et al.*, Phys. Rev. Lett. **55** (1985) 1874; D. Vernhet *et al.*, Phys. Rev. A **32** (1985) 1256; R. Hoekstra *et al.* J. Physique **50** (1988) C1/387.

[9] A. Salin, J. Physique **45** (1984) 671.

Elastic and inelastic processes in H^++CH_2 collisions below the 1.5 keV regime

Hiroya Suno[1,2], Sachchida N. Rai[3], Heinz-Peter Liebermann[4],
Robert J. Buenker[4], Mineo Kimura[5], R.K. Janev[2,6]

[1]*Faculty of Engineering, Yamaguchi University, Ube, 755-8611, Japan*
[2]*National Institute of Fusion Science, Oroshi-cho, Toki, 509-5292, Japan*
[3]*Computer Centre, Bijni Complex, North-Eastern Hill University, Shillong-793003, Meghalaya, India*
[4]*Fachbereich C-Theoretische Chemie, Bergische Universitaet Wuppertal, D-42119 Wuppertal*
[5]*Graduate School of Sciences, Kyushu University, Fukuoka 812-8581, Japan*
[6]*Macedonian Academy of Sciences and Arts, 1000 Skopje, Macedonia*

Keywords: scattering of atoms and molecules, interatomic and intermolecular potentials for collisions, charge transfer.

ABSTRACT

Electron capture and direct elastic scattering in collisions of H^+ ions with CH_2 molecules between 0.5 and 1.5 keV are theoretically investigated. A molecular representation is adopted within a fully quantum-mechanical approach. Differential cross sections (DCSs) for elastic scattering and electron capture are calculated at 1.5 keV and 0.5 keV for different molecular orientations. Our results indicate that electron capture dynamics and corresponding electron-capture cross sections depend substantially on the molecular orientation, thus revealing a strong steric effect.

1 Introduction

Electron capture such as $X^+ + Y \rightarrow X + Y^+$ is an important process in atomic and molecular physics, since it provides information fundamental for atomic and molecular spectroscopy and many-body collision dynamics. It is also important for applications such as astrophysics and fusion research. In this work, we study the electron capture and elastic scattering processes in a collision of H+ ion with CH2 (methylene) molecule between 1.5 and 0.5 keV. This work is along the line of the previous investigations which dealt with the electron capture processes in $H^+ + CH_4$ [1], $H^+ + C_2H_2$ [2] collisions below a few keV. The hydrocarbon molecule, CH_2, is a radical, and hence highly reactive, but is known to exist in various atmospheric and astrophysical environments. In fusion divertor plasmas, charge exchange reactions between protons and hydrocarbon molecules (including CH_2) play a decisive role in the hydrocarbon transport [3].

We consider specifically four molecular configurations: (I) the proton approaches the C atom along the bisector of the H-C-H bond angle, passing the midpoint of the H-H line, (II) it comes along the same line as (I), but in the opposite direction, (III) the proton approaches the C atom perpendicularly to the H-C-H bond angle, and (IV) it approaches the C atom perpendicularly to the H-C-H plane, see Fig. 1. The investigation of these configurations should give significant insight into the steric effect for electron capture, and expected to provide a guideline for future experimental research.

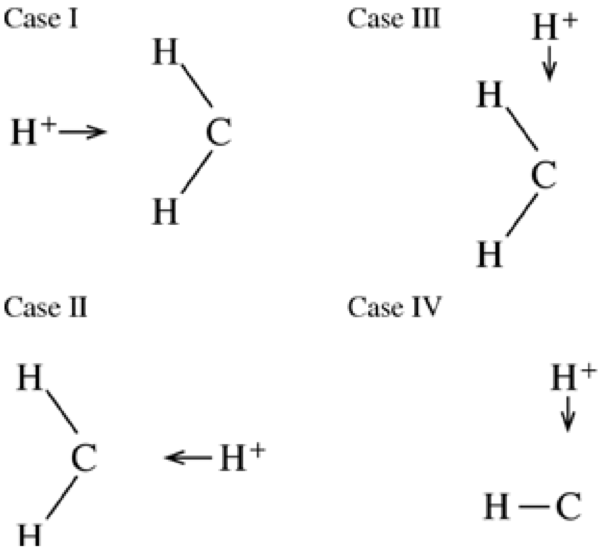

FIG. 1: Schematic diagram indicating the four molecular configurations for collisions.

2 Method

The adiabatic potential curves are calculated by using the multireference single- and double-excitation configuration-interaction (MRD-CI) method [4], with configuration selection and energy extrapolation. The Table-CI algorithm [5] is employed for efficient handling of Hamiltonian matrix elements for many-electron basis functions. The atomic orbital (AO) basis set employed in the present work consists of 80 contracted Cartesian Gaussian basis functions. The calculations are carried out in the C_{2v} point group for each of the approaches of the proton to the carbon atom along two of the three principal axes. Case III calculations are carried out in the lower C_s point group. All coordinates are frozen at the equilibrium intramolecular distances of the C_{2v} geometry [5]: $r_{\text{C-H}}$=1.0753Å and $\Theta_{\text{H-C-H}}$=134°. Only the internuclear distance (R) between the H^+ projectile and the C atom was varied. This approximation is reasonable down to a few tens of eV of collision energy.

Scattering dynamics is studied on the basis of the fully quantum-mechanical formulation of a molecular orbital close coupling (MOCC) method, in which dynamical transitions are driven by nonadiabatic couplings. The total wave function is described in an adiabatic representation as an expansion in products of electronic and nuclear wave functions and the electron translation factor. Insertion of the total wave function into the Schrödinger equation yields a set of coupled differential equations. It is computationally convenient to adopt a diabatic representation. Transformation from the adiabatic to diabatic representations leads to the coupled equation:

$$\left[\frac{1}{2\mu}\nabla_R^2 I - V^d(R) + EI\right] X^d(R) = 0\,, \tag{2}$$

and

$$E = k^2 / 2\mu\,, \tag{3}$$

where k is the momentum of the projectile, μ is the reduced mass of the system, and I is the identity matrix. The coupled equations (2) are solved numerically to obtain the scattering matrix for each partial wave l. The differential cross section is then obtained from the formula

$$\frac{d\sigma(\theta)}{d\Omega} = \frac{1}{4k^2}\left[\sum (2l+1)\left\{\delta_{if} - S_{if}^l\right\} P_l(\cos\theta)\right]^2\,, \tag{4}$$

where S_{if}^l is the scattering matrix element for partial wave l, and θ is the scattering angle in center-of-mass coordinates. Integration over all angles gives the total cross section.

3 Results

In Figs. 2 (a) and (b), we show the adiabatic potential curves. In Fig. 2 (a), the seven lowest potential curves for case I are presented as providing a general view of adiabatic potentials. The dominant electron-capture process is found to take place between the adiabatic potential curves shown as the solid lines in Fig. 2 (b). In Fig. 2 (b), we also show the potential curves involved in the dominant electron-capture process for case II-IV.

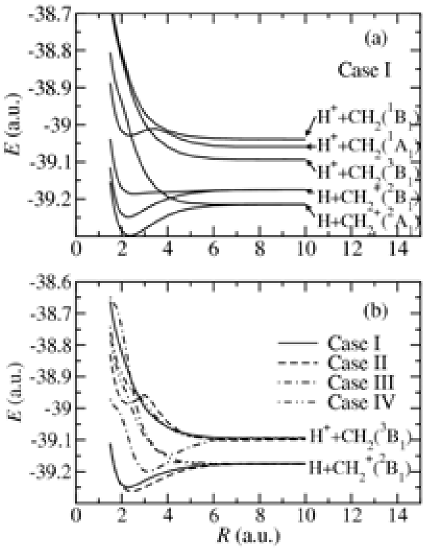

FIG. 2: Adiabatic potential curves for cases I, II, III and IV.

The differential cross sections (DCSs) obtained are shown in Figs. 3(a) and 3(b) for case I, in Figs. 4(a) and 4(b) for case II, in Figs. 5(a) and 5(b) for case III, and in Figs. 6(a) and 6(b) for cases IV, for scattering angles 0-180° at 1.5 and 0.5 keV, respectively. Both electron-capture and direct elastic scattering are included. For all four molecular configurations, large magnitudes of the DCSs of 10^6-10^8 cm^2/sr arise from narrow regions of the scattering angles θ<10°and θ>170°. Oscillations of the elastic scattering and electron capture DCSs are found for all molecular configurations. We state that these oscillations are attribuable to interference between elastic and electron-capture channels because most of these oscillations are formed to closely correlate between elastic and electron-capture channels. It is also apparent from these results that electron capture process is sensitive to the molecular orientation, thus a strong steric effect is observed. We find similarly large electron-capture differential cross sections for cases I and II, while cases III and IV are found to be secondary.

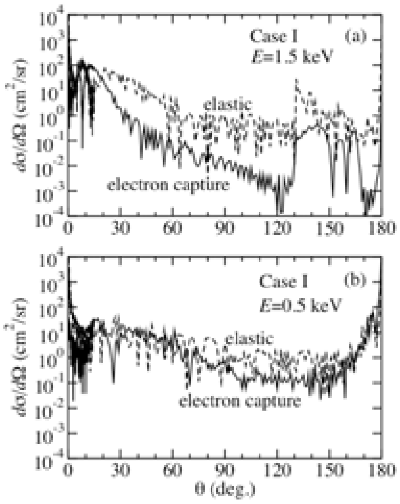

FIG. 3: Differential cross sections for case I at (a) 1.5 keV and (b) 0.5 keV.

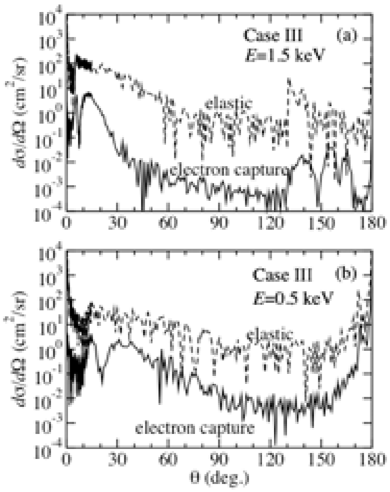

FIG. 5: Differential cross sections for case III at (a) 1.5 keV and (b) 0.5 keV.

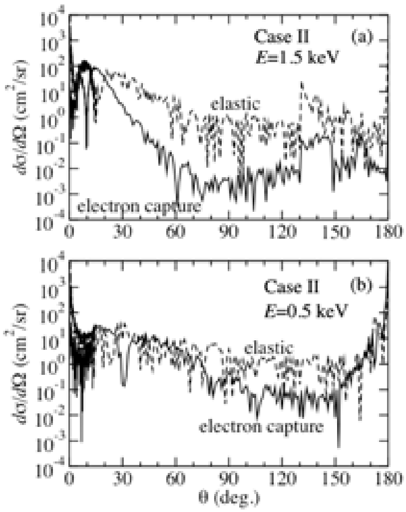

FIG. 4: Differential cross sections for case II at (a) 1.5 keV and (b) 0.5 keV.

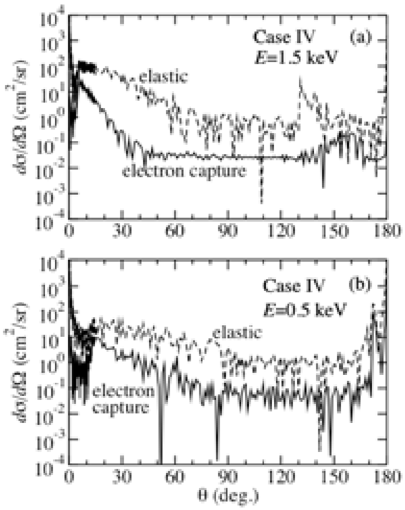

FIG. 6: Differential cross sections for case IV at (a) 1.5 keV and (b) 0.5 keV.

4 SUMMARY

In summary, we have carried out a theoretical study of elastic and electron-capture processes in collisions of H^+ ions with CH_2 molecules in the energy range from 500 eV to 1.5 keV for the four distinct molecular configurations as described in the text. We found a strong steric effect for electron capture in H^++CH_2 collisions at those energies. The present cross-section data are considered to be useful for various applications.

REFERENCES

[1] M. Kimura *et al.,* Phys. Rev. A **52**, 1196 (1995).

[2] M. Kimura *et al.,* Phys. Rev. A **54**, 5019 (1996).

[3] R.K. Janev and D. Reiter, Phys. Plasmas **9**, 4071 (2002).

[4] See for example, R.J. Buenker and S.D. Peyerimhoff, Theor. Chim. Acta. **35** 33 (1974).

[5] R.J. Buenker, in *Proceedings of the Workshop on Quantum Chemistry and Molecular Physics, Wollongong, Australia*, edited by P. Burton (University Press, Wollongong, 1980).

Institute of Applied Physics and Computational Mathematics Beijing 1 P. R. China

Abstract.

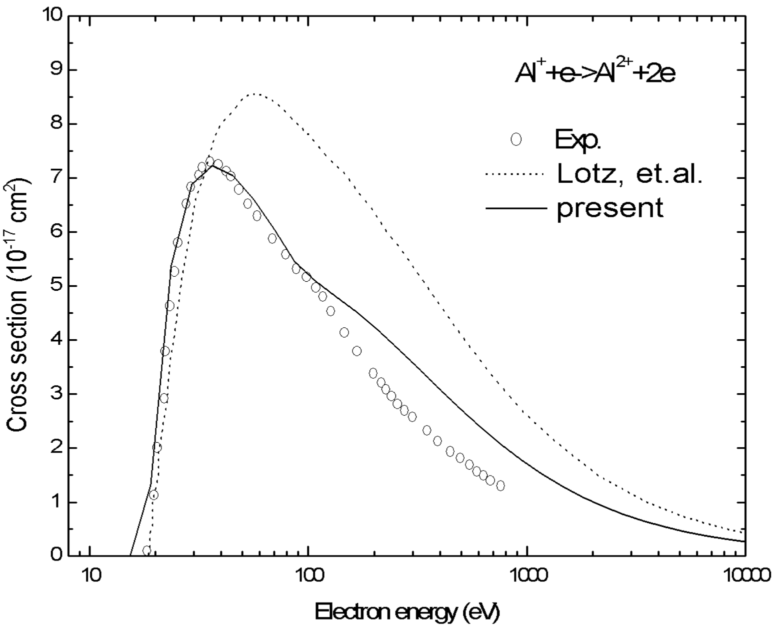
$Al^{+}+e\to Al^{2+}+2e$
Exp.
Lotz, et.al.
present
Cross section (10^{-17} cm^2)
0
1
2
3
4
5
6
7
8
9
10
10
100
1000
10000
Electron energy (eV)

ACKNOWLEDGEMENTS

REFERENCES

et. al.

13

PLASMA POLARIZATION SPECTROSCOPY

Anisotropic electron velocity distribution in an ECR helium plasma

Atsushi Iwamae* and Takashi Fujimoto
Department of Engineering Physics and Mechanics,
Graduate School of Engineering, Kyoto University, Kyoto 606-8501, Japan

ABSTRACT

A helium plasma is produced by electron cyclotron resonance heating in a cusp-configuration magnetic field. Neutral helium atom emission lines from n^1P, n^1D, n^3P and n^3D levels are linearly polarized in the direction perpendicular to the magnetic field. Population and alignment of these excited levels are deduced from the intensity and the polarization degree of the emission lines. Population-alignment collisional-radiative model is developed, and the experimental result is interpreted in terms of an anisotropic electron velocity distribution, which is found to be oblate.

Keywords: electron velocity distribution function, polarization, population-alignment collisional-radiative model, ECR discharge

I. INTRODUCTION

Non-Maxwellian distributions of electrons are sometimes encountered in laboratory and astrophysical plasmas. The electron velocity distribution function (EVDF) could even be anisotropic. Various methods have been developed to obtain information of the anisotropic EVDF: e.g., directional bremsstrahlung observation, polarization observation, Langmuir probes[1–6].

When atoms are excited by electrons with an anisotropic EVDF, a population imbalance among magnetic sublevels, or alignment, is produced in excited atoms, that emit linearly polarized light. Thus the anisotropy of EVDF can be investigated by plasma polarization spectroscopy (PPS). The importance of the polarization of optical radiation is being increasingly recognized in a variety of fields [7–9].

II. EXPERIMENTAL SETUP

Figure 1 shows the experimental setup for PPS for a cusp plasma[10]. A helium discharge plasma is generated in a stainless-steel vessel of a box shaped central part, $480 \times 480 \times 100\,\mathrm{mm}^3$,

---

*Electronic address: `iwamae@kues.kyoto-u.ac.jp`

with cylindrical tubes of inner diameter of 256 mm and length of 170 mm protruding from the both sides of the central vessel. Base pressure is less than 1.3×10^{-5} Pa. Helium gas is fed into the vessel to the pressure of $p_{\mathrm{He}} = 23$ mPa. A pair of coils produces a magnetic field with a cusp configuration, which is axially symmetric around the horizontal axis and plane symmetric with respect to the vertical central plane perpendicular to the axis. A microwave of 2.54 GHz, 800 W is fed through a fused quartz window into the vessel from the top of the central box for four seconds. The polarization of the microwave field is in the central plane. The ECR field strength is 875 G, and the ECR surface is a spheroid with short diameter of 92 mm along the central axis and long diameter of 168 mm on the central plane at the coil current of 990 A. Single probe measurements suggest electron temperatures of 20 eV and density of $10^{17}\,\mathrm{m}^{-3}$.

The plasma is observed through a fused quartz window in the side viewing port from slightly under the central horizontal plane. The plasma image of the area shown as a rectangle in Fig. 1 is recorded by a CCD camera. A linear polarizer and a band-pass filter for the 501.6 nm ($2^1S - 3^1P$) line with 1.5 nm bandwidth are equipped in front of the camera lens.

Figure 2(a) shows the plasma image by this line. Magnetic field lines on the plane including the axis and perpendicular to the line of sight (LOS) are also shown along with the ECR surface . Four images taken with different directions of polarizer of 0, 45, 90 and 135 degrees were processed and a polarization map[11] was constructed as shown Fig. 2(b). The polarization directions are perpendicular to the magnetic field. The polarization degree increases toward the outer region. It exceeds 0.1 at the edge of the cusp magnetic field.

The plasma region marked with LOS1 to 5 in Fig. 2(a) is observed with a polarization separation optics, PSO. The direction of the magnetic field line on the LOS is taken as the quantization axis. The PSO consists of a lens and a beam splitting Glan-Thompson prism. See Fig. 1. The PSO is tilted at 15° in order to resolve the polarization components which are parallel (π light) and perpendicular (σ light) to the quantization axis. The Glan-Thompson prism transmits the extraordinary (σ) light undeviated, and it deflects the ordinary (π) light which emerges from the side exit surface in the normal direction. The exit beams are free from the chromatic dispersion effect. On each output side of the prism, five optical fibers of 400 μm core diameter are aligned 1 mm apart each other in a row. The PSO are designed and adjusted so that each corresponding pair of ordinary and extraordinary rays falls on the same LOS in the plasma. The 400 μm core image is magnified in the plasma to 4 mm diameter and the five LOSs are about 10 mm apart on a line along the magnetic field as shown in Fig. 2(a). At the output end of the fiber bundle ten optical fibers are aligned 2 mm apart each other in a row. The exit surface of the fiber bundle is placed at a distance of 2 mm from the entrance slit of a

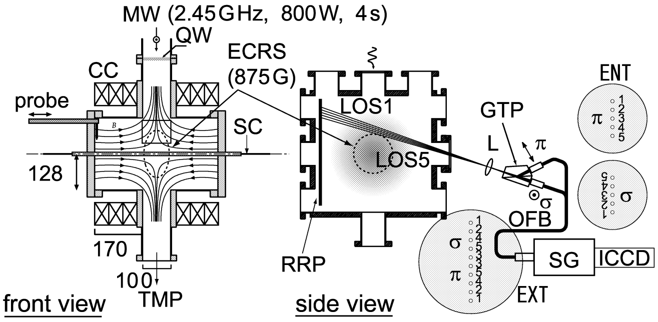

FIG. 1: The experimental setup. Front view and side view. Dimensions are in millimeters. MW: microwave, QW: quartz window, CC: cusp coil, ECRS: electron cyclotron resonance surface, SC: stuffer conductor (not used in the present experiment), RRP: Reflection Reducing Plate, LOS: Line of Sight, L: Lens, GTP: Beam splitting Glan-Thompson prism, OFB: Optical Fiber Bundle, SG: Spectrograph (Nikon G500: f=500 mm, F/8.5, 1200 grooves/mm grating), ICCD: Intensified CCD, ENT: entrance surfaces of OFB, EXT: exit surface of OFB.

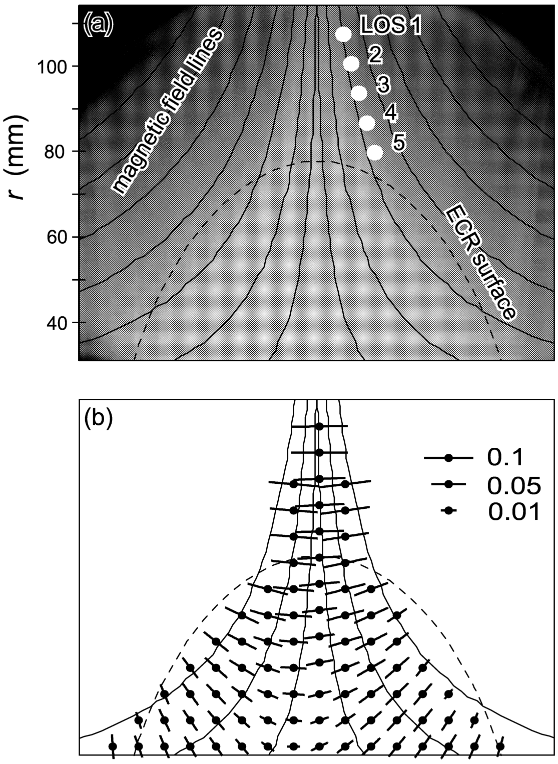

FIG. 2: (a) Plasma image taken with the He I 501.6 nm, $2^1S - 3^1P$ line. LOS: Line of Sight, solid curves: magnetic field lines, dashed curve: ECR surface (b) Polarization map of the $2^1S - 3^1P$ line. The direction of the lines indicates the polarization direction and the length of the line is proportional to the square root of the polarization degree.

spectrograph (Nikon G500:$f = 500\,\mathrm{mm}$, $F/8.5$, 1200 grooves/mm grating); this is for the purpose of focusing the fiber images on the focal plane. The entrance slit width is $200\,\mu$m. The dispersed light is focused on a photo-electric surface of an image intensifier, which is fiber-coupled with reduction of 1.5:1 to the CCD (578×384, $22.5\,\mu$m square pixels). Vertical pixels corresponding to the spectral image of each optical fiber are binned and five pairs of the polarization resolved spectra are obtained simultaneously. The optical system including the spectrograph and ICCD is calibrated against the light from a diffuse white reflectance standard plate (Labsphere Spctralon) illuminated by a spectral irradiance lamp(USHIO JPD100V-500WCS). The signal linearity to the ICCD gain and to the exposure time is examined with extreme care.

III. RESULTS AND DISCUSSION

Figure 3(a) shows an example of the polarization resolved spectra taken with 30 ms exposure. The three lines are 492.2 nm ($2^1P \leftarrow 4^1D$), 501.6 nm ($2^1S \leftarrow 3^1P$) and 504.8 nm ($2^1P \leftarrow 4^1S$). Since the upper level of the 504.8 nm line is a ^1S state, this line emission is never polarized and is used as a reference for the polarization determination for other lines. The σ-component intensities of the 501.6 and 492.2 nm lines are found to be higher than the corresponding π-component intensities. The total intensity and the longitudinal alignment of an emission line are defined as $I_0 = \frac{2}{3}(I_\pi + 2I_\sigma)$ and $A_\mathrm{L} = (I_\pi - I_\sigma)/(I_\pi + 2I_\sigma)$, respectively. During the four-second duration of a single discharge, 56 spectra are taken with 30 ms exposure, and a total of 224 spectra in the four discharges are processed to construct a histogram, or a frequency distribution, of the observed A_L. Figure 3(b) shows an example of the histograms of A_L for the three lines on LOS 1. The A_L for both the 492.2 and 501.6 nm lines are negative all from LOS 1 to LOS 5. LOS 1 observes the outermost region where A_L takes the largest absolute values among the observed A_L. The A_L decreases with an increase in helium pressure to almost diminish at $p_\mathrm{He} = 1.1\,\mathrm{Pa}$.

The intensity I_0 of an emission line $s \leftarrow p$ is proportional to the population $n(p)$ of the upper level p:

$$I_0(p,s) = n(p)A(p,s)\hbar\omega\frac{\mathrm{d}V\,\mathrm{d}\Omega}{4\pi}, \tag{1}$$

where $A(p,s)$ is Einstein's A coefficient, $\mathrm{d}V$ is the volume of the observed region and $\mathrm{d}\Omega$ is the solid angle subtended by our optics. The longitudinal alignment A_L is proportional the alignment divided by the population,

$$A_\mathrm{L}(p,s) \;=\; (2L_p+1)\left(\frac{3}{2}\right)^{1/2}(-1)^{L_p+L_s}\begin{Bmatrix} L_p & L_p & 2 \\ 1 & 1 & L_s \end{Bmatrix}\frac{a(p)}{n(p)}. \tag{2}$$

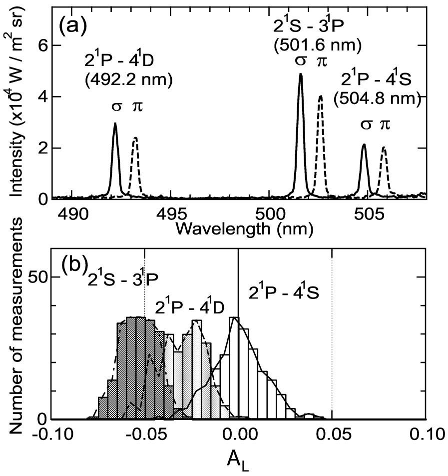

FIG. 3: (a) Polarization resolved spectra observed on LOS 1. The π and σ components are shown by the dashed and solid curves, respectively. The π component is displaced by 1 nm. (b) Histograms of the londitudinal alignment $A_{\mathrm{L}} = (I_\pi - I_\sigma)/(I_\pi + 2I_\sigma)$. The $2^1P - 4^1S$ line is used to calibrate relative sensitivities of our observation system.

where $\{\}$ is the 6-j symbol and L_i is the orbital angular momentum quantum number of level i. We convert the observed I_0 and A_{L} into $n(p)$ and $a(p)$ for several upper levels. For triplet levels, the fine-structure is taken into account; the depolarization effect caused by fine structure reduces the observed longitudinal alignment. The results are displayed in Fig. 4(a) and (b), respectively.

The population-alignment collisional-radiative, PACR, model is a kinetic model which relates the observed intensity and polarization to an anisotropic EVDF in plasma[7]. The results from the model for beryllium-like oxygen and for helium-like carbon are reported in [12, 13]. The present PACR model is the extension of the CR model developed by Goto[14]. Total of 61 levels, up to the principal quantum number n=22, are included. Alignment is considered in the levels n^1P, n^1D, n^3P and n^3D with $n \leq 7$. The excitation cross sections by electron impact, Q_0^{00}, are based on Ralchenko et al[15]. Csanak et al. calculate the alignment production cross sections, Q_0^{20}, by the distorted wave approximation, DWA[16, 17]. It is found that Q_0^{20}/Q_0^{00} depends only weakly on n of the upper level. Bray has provided us with magnetic-sublevel resolved cross sections $Q_{MM'}$ calculated by the convergent close-coupling, CCC, method[18, 19] for transitions, $1^1S, 2^1S, 2^3S \rightarrow n^1P, n^1D, n^3P, n^3D$ ($n \leq 4$; except for $2^1P, 2^3P, 4^3P$ and 4^3D)[20].

Isotropic thermal EVDFs are first assumed in the present PACR model, and the results are confirmed to coincide with those from the original CR model[14]. Since we observed the plasma edge, we try to interpret the result in terms of a single set of plasma parameters. As a model EVDF of gyrating electrons accelerated by the ECR microwave field we adopt a Saturn-type

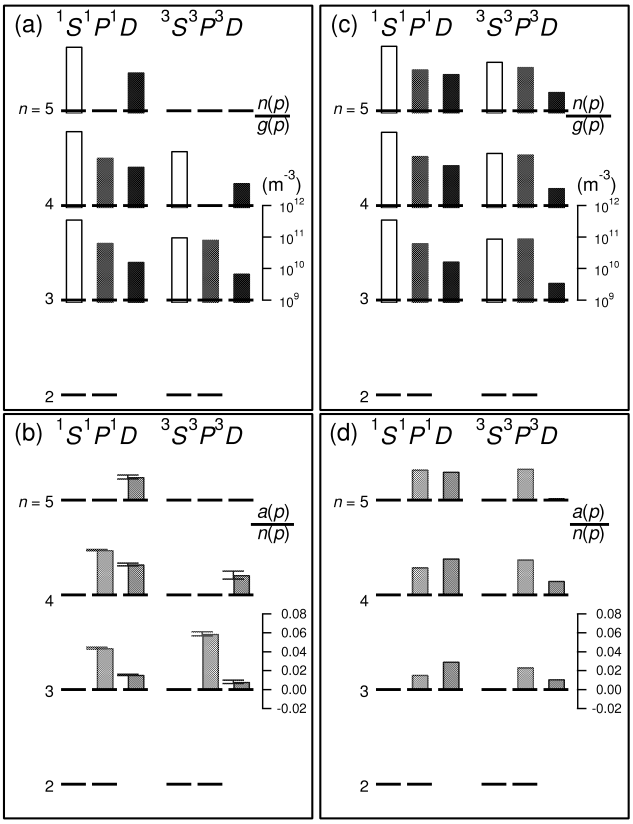

FIG. 4: Experimentally observed intensity and longitudinal alignment are converted into (a) the population per unit statistical weight, $n(p)/g(p)$, and (b) the alignment divided by the population, $a(p)/n(p)$. PACR model calculation: (c) $n(p)/g(p)$ and (d) $a(p)/n(p)$.

EVDF: i.e. we assume $f(v,\theta) = f_{\rm th}(v,\theta) + f_{\rm r}(v,\theta)$: where the central and ring components are given by,

$$f_{\rm th}(v,\theta)=\frac{2\pi}{1+\delta}\left(\frac{m}{2\pi k_{\rm B}T_{\rm eth}}\right)^{3/2}\exp\left(\frac{-mv^2}{2k_{\rm B}T_{\rm eth}}\right) \tag{3}$$

and

$$f_{\rm r}(v,\theta)=\frac{2\pi\delta A_r}{1+\delta}\exp\left\{\frac{-m\left(v^2-2vV_{\rm r}\sin\theta+V_{\rm r}^2\right)}{2k_{\rm B}T_{\rm er}}\right\}, \tag{4}$$

respectively. The ratio of the electron number densities between these components is δ. The direction of the displacement $V_{\rm r}$ is perpendicular to the quantization axis in velocity space. Here m is the electron mass, $k_{\rm B}$ is the Boltzmann constant and $A_{\rm r}$ is the normalization factor to give $\iint f_{\rm r}(v,\theta)v^2\sin\theta{\rm d}v\,{\rm d}\theta = \delta/(1+\delta)$. The population of the 2^3S metastable state is reduced to effectively include the diffusion loss; the reduction to one-twentieth brings the calculated population densities of the triplet system to overall agreement with the experiment. The effect of radiation trapping on the resonance-series lines is taken into account by introducing the escape factor, g_0. The estimated g_0 is 0.06 for 1^1S-2^1P, for example. Alignment relaxation, or

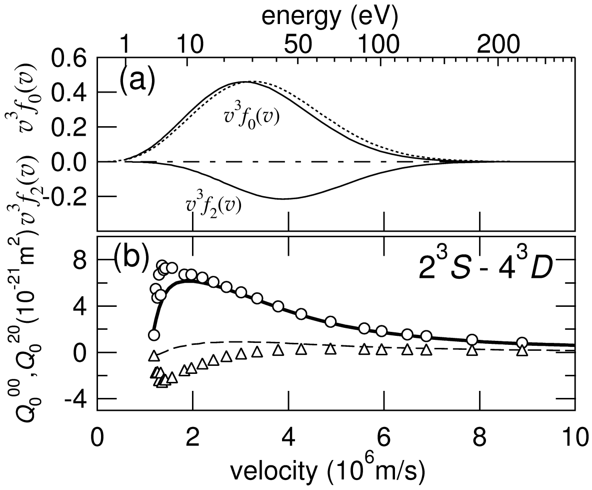

FIG. 5: (a) Solid curves: $K = 0$ (upper) and $K = 2$ (lower) terms of Legendre expansion of the EVDF, $v^3 f_k(v, \theta)$, with $T_{\rm eth} = T_{\rm er} = 14\,{\rm eV}, V_{\rm r} = 1.8 \times 10^6\,{\rm m/s}$ and $\delta = 0.68$. Dotted curve: Maxwell EVDF of $T_{\rm e} = 20\,{\rm eV}$ for comparison. (b)Excitation and alignment production cross sections from the 2^3S metastable level to the 4^3D level. Solid curve: Q_0^{00} [15]. Dashed curve: Q_0^{20} by DWA[17]. Open circles and triangles are Q_0^{00} and Q_0^{20}, respectively, by CCC[20].

disalignment, by radiation re-absorptions[21, 22] is also included in the model. The alignment destruction rate is the sum of the disalignment rate γ_2 and the depopulation rate γ_0. γ_2 is estimated to be $1.21 \times 10^9\,{\rm s}^{-1}$ for the transition $1^1S - 2^1P$, for example. An ionizing plasma was assumed[23].

Figure 4(c) and (d) shows the best-fitted distributions of $n(p)/g(p)$ and $a(p)/n(p)$ with $T_{\rm eth} = T_{\rm er} = 14\,{\rm eV}$, $V_{\rm r} = 1.8 \times 10^6\,{\rm m/s}$ (corresponding to 10 eV) and $\delta = 0.68$ with $n_{\rm e} = 2.0 \times 10^{16}\,{\rm m}^{-3}$. The experimentally observed $n(p)/g(p)$ are well reproduced. The $n(p)/g(p)$ distribution is similar to the result for the thermal distribution with $T_{\rm e} = 20\,{\rm eV}$; the isotropic $K = 0$ term of the Legendre expansion coefficients of the present EVDF, $v^3 f_0$, is close to the Maxwell distribution at $T_{\rm e} = 20\,{\rm eV}$ as shown in Fig. 5(a). The $K = 2$ term, $v^3 f_2$, is negative. The absolute value of $v^3 f_2$, increases with an increase in δ. The velocity at the peak of $v^3 f_2$ increases with an increase in $V_{\rm r}$.

The alignment production rate coefficient is given from the integration of Q_0^{20} over $v^3 f_2$. For excitation from the ground state, DWA and CCC both give negative cross sections in the relevant energy range, leading to positive alignments in all the levels. For excitation from 2^3S to n^3D, DWA gives slightly positive cross sections as shown in Fig. 5(b), while CCC gives a negative cross section giving rise to positive alignment, which reproduces well our experiment.

The authors would like to thank Ms. Karen Lewis and Professor Igor Bray for providing cross sections and Dr. George Csanak for discussions and variable comments. This work was partially supported by the Ministry of Education, Science and Culture, Grant-in-Aid for Young Scientist (B), No. 13780386 also by the 21st Century COE program for Research and Education on Complex Functional Mechanics Systems.

[1] D. G. S. Greene, J. L. Shohet, and P. A. Raimbault, Phys. Rev. Lett. **27**, 90 (1971).

[2] D. G. S. Greene and J. L. Shohet, Plasma Phys. **15**, 5 (1973).

[3] A. P. Mezentsev, A. S. Mustafaev, and V. L. Fedorov, Sov. Phys.-Tech. Phys. **30**, 322 (1985).

[4] V. L. Fedorov, Sov. Phys.-Tech. Phys. **30**, 554 (1985).

[5] V. A. Godyak, P. B. Piejak, and B. M. Alexandrovich, Plasma Sources Sci. Technol. **1**, 36 (1992).

[6] T. Fujimoto, H. Sahara, T. Kawachi, T. Kallstenius, M. Goto, H. Kawase, T. Furukubo, T. Maekawa, and Y. Terumichi, Phys. Rev. E **54**, R2240 (1996).

[7] T. Fujimoto and S. A. Kazantsev, Plasma Phys. Control. Fusion **39**, 1267 (1997).

[8] S. A. Kazantsev and J. C. Hénoux, *Polarization Spectroscopy of Ionized Gases* (Kluwer, Boston, 1995).

[9] S. A. Kazantsev, A. G. Petrashen, and N. M. Firstova, *Impact Spectropolarimetric Sensing* (Kluwer Academic / Plenum Publishers, 1999).

[10] M. Uchida, S. Fukumoto, M. Asakawa, H. Tanaka, T. Maekawa, and Y. Terumichi, Jpn. J. Appl. Phys. **38**, L885 (1999).

[11] E. Vogt and J.-C. Hénoux, Astron. Astrophys **349**, 283 (1999).

[12] A. Iwamae, A. Tanaka, T. Inoue, T. Fujimoto, H. L. Zhang, D. P. Kilcrease, and G. Csanak, in *Proceedings of the 3rd US-Japan Plasma Polarization Spectroscopy Workshop* (2001), p. 165.

[13] A. Iwamae, T. Fujimoto, H. L. Zhnag, D. P. Kilcrease, and G. Csanak, NIFS-DATA **78** (2003).

[14] M. Goto, J. Quant. Spectros. Radiat. Trans. **76**, 331 (2003).

[15] Y. V. Ralchenko, R. K. Janev, T. Kato, D. V. Fursa, I. Bray, and F. J. de Heer, NIFS-DATA **59** (2000).

[16] G. Csanak and D. C. Cartwright, J. Phys. B: At. Mol. Phys. **22**, 2769 (1989).

[17] G. Csanak, D. C. Cartwright, S. A. Kazantsev, and I. Bray, Phys. Scripta **T78**, 47 (1998).

[18] I. Bray, Phys. Rev. A **49**, 1066 (1994).

[19] D. V. Fursa and I. Bray, Phys. Rev. A **52**, 1279 (1995).

[20] I. Bray, *CCC Data Base* (2004), URL `http://atom.murdoch.edu.au/CCC-WWW/index.html`.

[21] M. I. D'yakonov and V. I. Perel', Soviet Phys. JETP **20**, 997 (1965).

[22] M. Nimura, M. Hasuo, and T. Fujimoto, in *Proceedings of the Fourth International Symposium on Plasma Polarization Spectroscoy* (2004).

[23] T. Fujimoto, *Plasma Spectroscopy* (Oxford University Press, 2004).

Improved density functional calculations for atoms, molecules and surfaces

B. Fricke, J. Anton, S. Fritzsche, C. Sarpe-Tudoran

Institut für Physik, Universität Kassel, D-34109 Kassel, Germany

Abstract

The non-collinear and collinear descriptions within relativistic density functional theory is described. We present results of both non-collinear and collinear calculations for atoms, diatomic molecules, and some surface simulations. We find that the accuracy of our density functional calculations for the smaller systems is comparable to good quantum chemical calculations, and thus this method provides a sound basis for larger systems where no such comparison is possible.

1 Introduction

An attractive way to describe electronic matter is through density functional theory (DFT). This method is as old as wave-function based approximations for solving the electronic Schrödinger or Dirac equation, and originally comes from the simple Thomas-Fermi model [1, 2], which in early times was the only practical method to describe total electronic energies and densities within atoms. However, with the ever increasing computer power and the development of more sophisticated algorithms, the many-particle Dirac equation can now be treated with relatively high accuracy for small electronic systems.

For atoms the Dirac-Fock-Slater [3], Dirac-Fock and Multiconfiguration Dirac-Fock [4, 5] approximations have been in use for more than two decades now, and very precise ab-initio calculations are now possible for many-electron systems in heavy atoms [6]. Somewhat later the same development began for the solution of molecular systems, but at that time most quantum chemical methods were restricted to the non-relativistic framework, and initially relativistic effects were included through the Pauli-Hamiltonian via perturbation theory (if at all). Because of the importance of spin-orbit coupling for molecules containing heavy elements, a lot of effort was invested in approximate 2-component methods which often lead to excellent results even for states with very large spin-orbit splittings (some reviews are given in [7, 8, 9]; see also ref. [10] for a collection of articles concerning the early days of relativistic electronic structure theory). Nevertheless, such methods have to be considered as approximations to the full four-component Dirac description. The density functional method has a sound basis in form of the Hohenberg-Kohn Theorem in 1964 [11] which proved that all electronic matter can be described exactly by a 3-dimensional density only. (Kohn received the Nobel prize for this in 1998).

In 1973 this theorem was extended to the relativistic domain by Rajagopal and Callaway [12]. In this case the total energy is a unique functional of the four-current J_μ. The problem to find the exact four-current in the relativistic framework analogous to the density in the non-relativistic case has not yet been solved. Nevertheless, a number of density functionals have already been proposed [15, 14, 13, 16] and still strong efforts are made to find the "exact" density functional (see for example Ref. [17, 18]). Four-component density functional theory for molecules within the non-collinear approach have already been reported.

2 Non-collinear and collinear Kohn-Sham theory

We briefly discuss Gordon's decomposition [19] to approximate the four-current of the exact relativistic formulation in the form of a charge and magnetization density in order to perform actual calculations within the non-collinear formalism for molecules. A general derivation of this method can be found in Ref. [17] and [20]. Within this approximation the total energy of a molecular system is given by the following expression

$$\begin{aligned} E &= \sum_{i=1}^{M} n_i \left\langle \psi_i \,\middle|\, \hat{t} \,\middle|\, \psi_i \right\rangle + \int V^N \rho \, d^3\vec{r} + \frac{1}{2}\int V^H \rho \, d^3\vec{r} \\ &\quad + E^{xc}[\rho, \vec{m}] + \sum_{p>q} \frac{Z_p\, Z_q}{|\vec{R}_p - \vec{R}_q|} \end{aligned} \tag{1}$$

with the density ρ and magnetization density $\vec{m}$ which are defined by

$$\rho(\vec{r}) = \sum_{i=1}^{M} n_i \, \psi_i^+(\vec{r})\psi_i(\vec{r}) \tag{2}$$

$$\vec{m}(\vec{r}) = -\mu_B \sum_{i=1}^{M} n_i \psi_i^+(\vec{r})\beta\vec{\Sigma}\psi_i(\vec{r})\,. \tag{3}$$

Here n_i are the occupation numbers, $\vec{r}$, $\vec{R}_q$ are the electronic and nuclear coordinates respectively and μ_B is the Bohr-magneton. The index i runs over all occupied molecular orbitals M, which in our case are four-component Dirac spinors. The four-component spin operator $\vec{\Sigma} = (\Sigma_x, \Sigma_y, \Sigma_z)$ is built from the two component Pauli matrices $\vec{\sigma}$.

t is the relativistic kinetic energy operator, V^N is the nuclear potential, and E^{xc} is the exchange-correlation energy functional. V^H is the electronic Hartree potential, the direct electric repulsion energy.

The variation of the energy functional (1) leads to the relativistic Kohn-Sham (KS) equations in their general form for the molecular Kohn-Sham orbitals ψ_i

$$\left\{\hat{t} + V^N + \tilde{V}^H + \frac{\delta E^{xc}[\rho, \vec{m}]}{\delta \rho} - \mu_B \beta \vec{\Sigma} \cdot \frac{\delta E^{xc}[\rho, \vec{m}]}{\delta \vec{m}}\right\} \psi_i = \epsilon_i \psi_i \qquad i = 1, ..., M' \tag{4}$$

This general formulation is called a non-collinear description which allows the magnetization density to point in any direction at any point of the system under consideration. Because often the z component of the magnetization density is physically important, an approximation of this expression is used which is called the collinear description. For details we refer here to Ref. [23].

At this point we would like to make a few general but important comments: Although physically incorrect, people often speak of 'spin up' and 'spin down' components in this collinear description. Of course the 'spin' has a strong contribution to the magnetization density. But one has to remember two important facts. First, orbital angular momenta also contribute to the magnetization density and second, spin as well as orbital angular momenta have no good quantum numbers anymore in relativistic theory and therefore, one should speak of magnetization densities only. The total angular momentum J and the angular momenta j of each electron are the only good quantum numbers in atoms.

In addition we would like to comment on the Kohn-Sham orbitals. They contribute to the charge resp. the magnetization density according to formulae (2) and (3). Because these densities are in principle exact, the Kohn-Sham orbitals cannot be compared to Hartree-Fock wave functions which are usually written in Slater determinants. Rather the density built from Kohn-Sham orbitals must be compared with a density built from an infinite sum of Slater determinants in the Hartree-Fock sense.

3 Results

Due to the fact that the practical solution of the Kohn-Sham equations in form of (4) is hard to achieve (independent of the special functional used), only very few results have been reported so far. We recently have developed a method to perform this kind of calculations [21, 23] which allows the magnetic moment to point in any direction at any point in space. In this non-collinear approximation nearly each electron is treated by its own wave function with a quantum number j and magnetic quantum number m_j in the atomic decomposition of the molecular wave function.

Due to the fact that not only the electric but also the magnetic density is included in the self-consistent iteration, each electron often converges to a non-degenerate energy eigenvalue and thus depends on the occupation of the Kohn-Sham orbitals with different total energies. We should mention here that all results which we present in the following are performed within the Becke 88 (B88) [15] for the exchange and Perdew 86 (P86) [14] for the correlation functionals. In addition, we compare all these results with the Perdew Wang 91 (PW91) [16] functionals which often lead to very similar values compared to the other functionals.

3.1 Atoms

Molecular dissociation energies depend on the total energy of the molecule as well as the total energy of the separated fragments or atoms. To be physically correct, all values of the potential energy curve, including the infinite distance values, have to be calculated with the same density functional method. In the non-relativistic description one gets the average of the multiplet, and in the relativistic description the average of the sub-multiplet. Thus up to now the atomic values had often to be corrected afterwards. In most cases the non-collinear description automatically reaches the atomic ground state, which means that one does not need to correct the potential energy curve at larger distances. As an example we present in Fig. 1 the atomic results of Pt for those levels which can be calculated here in an unambiguous way. These results are compared to experimental values [26] and results from Dirac-Fock calculations performed by using the Desclaux code [4]. The non-collinear DFT values are reasonably good and compare even better with experiment than the Dirac-Fock values. Of course, deviations are due to the approximations made in the density functional.

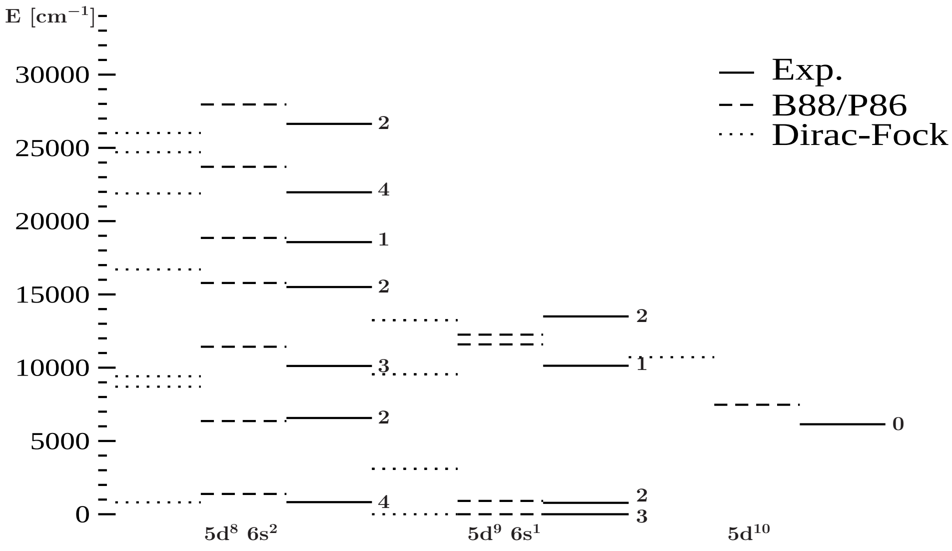

Figure 1: Level structure of Pt

3.2 Diatomic systems

Here we start with a molecule which has been investigated most intensively during the last decade using a number of relativistic approximations: Au_2. The argument for this choice is that this system behaves very relativistically, that is scalar relativistic effects are dominant and spin-orbit contributions are relatively small [22]. In Tab. 1 we present the results of Au_2 and a few other diatomic molecules from our non-collinear calculations. We compare them with the collinear approximation and other DFT and quantum chemical results as well as experiments. Nearly all these systems in Tab. 1 have an even number of electrons so that there is no resulting magnetic contribution in the molecule. As an example for an odd number of electrons in the molecule we include the results for the system NiAu in Tab. 1 with our non-collinear calculations. The molecular ground state of NiAu is of ${}^2\Delta_{5/2}$ symmetry [23].

Molecule	R_e(a.u.)	D_e (eV)	ω(cm^{-1})	Method	Reference
Ag_2	4.90	2.01	179	DKS (BLYP)	[32]
	4.81	1.71	190	B88/P86 (SP, col)	this work
	4.81	1.71	190	B88/P86 (SP, n-col)	this work
	4.79	1.65(3)	192	exp	[33]
Au_2	4.81	2.23	173	DKS (BLYP)	[32]
	4.73	2.30	192	B88/P86 (SP, col)	this work
	4.73	2.30	192	B88/P86 (SP, n-col)	this work
	4.67	2.29(2)	191	exp	[33]
Pt_2	4.42	3.28	225	B88/P86 (SP, col)	[21]
	4.42	3.12	224	B88/P86 (SP, n-col)	[21]
	4.4087(8)	3.14(2)	222.46(66)	exp	[34]
NiAu	4.43	2.49	280	B88/P86 (SP, col)	[23]
	4.44	2.49	276	B88/P86 (SP, n-col)	[23]
	4.443(2)	2.52(17)	–	exp	[35]

Table 1: Bond lengths, bond energies, and vibrational frequencies for a number of diatomic molecules.

As expected, spin-polarization is important for obtaining the right dissociation limit, however, for a closed-shell system like Au_2 the collinear approximation is sufficient. Anyway, the spin-polarized results agree well with experiment. A significant improvement is, however, obtained for Pt_2, where the non-collinear result for the dissociation energy is now in excellent agreement with experiment. In Tab. 2 we also present results for two Van der Waals systems, Hg_2 and $(112)_2$. Again, the non-collinear approximation has nearly no effect on the results, but the resulting binding energy is at least of the right order of magnitude. Only at this point we see a difference between the B88/P86 and PW91 functionals and the difficulties describing a Van der Waals system like Hg_2 by quantum chemical methods have been addressed intensively in the past (see for example ref.[24]). We should add that the search of suitable density functionals for describing Van der Waals systems is still in progress. Examples are refs.[27], [25] and [28].

The results in addition show that for all density functionals which are frequently used the singlet state remains the ground state although the triplet states splitting is not so small.

Mol.	R_e(Å)	D_e (cm^{-1})	ν_1 (cm^{-1})	Method	Reference
Hg_2	3.63	73	14	B88/P86	this work
	3.55	385	24	PW91	this work
	3.63(4)	350(20)	19.7(5)	exp	
	3.69(1)	380(25)	19.6(3)	exp	
$(112)_2$	3.45	315	25	B88/P86	this work
	3.39	649	30	PW91	this work

Table 2: Bond lengths, bond energies, and vibrational frequencies for a number of diatomic molecules.

3.3 Many atomic molecular systems

There are a few systems which we have calculated with this improved relativistic non-collinear density functional method. One of these systems were the tetrachlorides of Ti, Zr, Hf and Rf (element 104) because $RfCl_4$ is a molecule which shows up in the chemical separation of the superheavy element 104 [29]. The second example is the calculation of the magnetic behavior of three complicated bi-radical systems where our method was able to identify two as singlet and one as triplet ground state [30].

3.4 Simulation of surfaces

Another broad field to apply the density functional method is the simulation of physical processes like the adsorption energy of atoms on surfaces. There are two ways to do so: The first possibility is to calculate a cluster of a given size which is a part of the surface of a solid with the adatom in a "molecular" calculation. If the calculated value of the adsorption energy does not change any more with increasing cluster size a final value has been reached. The second method which leads to a faster convergence with size is to add additional electrostatic potential of atoms which are outside the cluster. This is the so-called embedded cluster method. To give a brief survey of one system we present in Tab. 3 the adsorption energy of Hg resp. 112 on a gold surface.

Molecule	Position	Binding energy (eV)
$HgAu_{14}$	top position	1.15 eV
$112Au_{14}$	top position	0.66 eV
$HgAu_{22}$	hollow position	1.26 eV
$112Au_{22}$	hollow position	0.88 eV

Table 3: Adsorption energy of Hg resp. element 112 on a cluster with the embedded atom method with a GGA (Ref. [14, 15]) functional

4 Conclusion

Within relativistic density functional theory the non-collinear approximation is the most sophisticated one currently available. We have given a number of examples which shows its importance and success. Of course, improvements still have to be made and the search for even better density functionals has not yet come to an end [31]. In addition an improved handling of the 4-current will one day improve the description.

In terms of a judgement of the non-collinear density functional calculations given in this paper we can state that the results often compare very well with the experimental results and show the same quality as the best known quantum chemical calculations for such systems. Due to the fact that wave function based four-component relativistic quantum chemical calculations cannot routinely be applied for large systems, this method seems to be the best available relativistic procedure for larger systems with high predictive power as demonstrated for the smaller systems.

Acknowledgments

J. A. gratefully acknowledges the financial support from the Deutsche Forschungsgemeinschaft (DFG). C. S.-T. gratefully acknowledges support by GSI Darmstadt and a grant from Dieter Spethmann.

References

[1] R. H. Thomas, Proc. Camb. Phil. Soc. **23**, 542 (1927)

[2] E. Fermi, Z. Phys. **48**, 73 (1928)

[3] D. A. Lieberman, D. T. Cromer, and J. T. Waber, Comp. Phys. Com. **2**, 107 (1970)

[4] J. P. Desclaux, Comp. Phys. Com. **9**, 31 (1975)

[5] I. P. Grant, B. J. Mc Kensie, P. H. Normington, D. F. Myers, and N. C. Paper, Comp. Phys. Comm. **21**, 2007 (1980) K. G. Dyall, I. P. Grant, C. T. Johnson, F. A. Parpia, and E. P. Plummer, Comp. Phys. Comm. **55**, 425 (1989)

[6] U. Kaldor, E. Eliav, and A. Landau, *Theoretical Chemistry and Physics of Heavy and Superheavy Elements.*, edited by U. Kaldor and S. Wilson, Kluwer Academic, Dordrecht, 2003; pg.171 John Wiley & Sons, 2001

[7] R. L. Matcha, J. Am. Chem. Soc. **95**, 7506 (1973)

[8] Y. S. Lee, W. C. Ermler, and K. S. Pitzer, J. Chem. Phys. **67**, 6851 (1977)

[9] B. A. Hess, C. M. Marian, and S. D. Peyerimhoff, *Modern Electronic Structure Theory*, edited by D. R. Yarkony, World Scientific, 1995; pg. 152.

[10] P. Pyykkö, Lecture Notes in Chemistry, Vol. 41, Springer, Berlin, 1986.

[11] P. Hohenberg and W. Kohn, Phys. Rev. **136**, 864 (1964)

[12] A. K. Rajagopal, J. Callaway, Phys. Rev. B**7**, 1912 (1973)

[13] S. H. Vosko, L. Wilk, M. Nusair, Can. J. Phys. **58**, 1200 (1980)

[14] J. P. Perdew, Phys. Rev. B**33**, 8822 (1986)

[15] A. D. Becke, Phys. Rev. A**38**, 3098 (1988)

[16] J. P. Perdew, in *Electronic Structure of Solids*, ed. by P. Ziesche and H. Eschrig, p.11, Akademie Verlag, Berlin 1991

[17] E. Engel, R. M. Dreizler, S. Varga, and B. Fricke, *Relativistic Effects in Heavy-Element Chemistry and Physics.*, edited by B. A. Hess, John Wiley & Sons, 2001

[18] E. Engel, and R. M. Dreizler, Top. Curr. Chem. **181**, 1 (1996)

[19] H. Eschrig and V. D. P. Servedio, J. Comput. Chem. **20**, 23 (1999)

[20] E. Engel, *Relativistic Electronic Structure Theory, Part 1: Fundamentals*, edited by P. Schwerdtfeger, Elsevier, Amsterdam, 2002

[21] J. Anton, T. Jacob, B. Fricke and E. Engel, Phys. Rev. Lett. **89**, 213001 (2002)

[22] R. Wesendrup, J. K. Laerdahl, and P. Schwerdtfeger, J. Chem. Phys. **110** 9457 (1999)

[23] J. Anton, B. Fricke, E. Engel, Phys. Rev. **A 69**, 012505 (2004)

[24] P. Schwerdtfeger, R. Wesendrup, G. E. Moyano, A. J. Sadlej, J. Greif, and F. Hensel, J. Chem. Phys. **115** 7401 (2001)

[25] W. Kohn, Y. Meir, and D. E. Makarov, Phys. Rev. Lett. **80**, 4153 (1998)

[26] C. E. Moore, *Ionization Potentials and Ionization Limits derived from the Analyses of Optical Spectra*; NSRDS-NBS24, NBS, Washington DC 1970

[27] E. Engel, A. Höck, and R. M. Dreizler, Phys. Rev. **A 61**, 032502 (2000)

[28] E. Hult, P. Hyldaard, J. Rassmeisel, and B. I. Lundquist, Phys. Rev. **B 64**, 195414 (2001)

[29] J. Anton, M. Hirata, B. Fricke, and V. Pershina, Chem. Phys. Lett. **380**, 95 (2003)

[30] J. Anton, T. Ishii, B. Fricke, Chem. Phys. Lett. **388**, 248 (2004)

[31] J. P. Perdew, S. Kurth, A. Zupan, and P. Blaha, Phys. Rev. Lett. **82**, 2544 (1999)

[32] T. Yanai, H. Iikura, T. Nakajima, Y. Ishikawa, and K. Hirao, J. Chem. Phys. **115**, 8267 (2001)

[33] K. P. Huber and G. Herzberg, *Constants of Diatomic Molecules*, van Nostrand Reinhold Company, New York 1979

[34] M. M. Airola and M. D. Morse J. Chem. Phys. **116**, 1313 (2002)

[35] E. M. Spain and M. D. Morse, J. Chem. Phys. **97**, 4605 (1992)

ELECTRONIC STRUCTURE OF ATOMS IN LASER PLASMA: THE DEBYE SHIELDING MODEL

Tokuei Sako, Hiroshi Okutsu, Kaoru Yamanouchi
Department of Chemistry, School of Science, The University of Tokyo,
7-3-1 Hongo, Bunkyo-ku, Tokyo 113-0033, Japan

ABSTRACT

The electronic structure and the energy spectra of multielectron atoms in laser plasmas are examined by the Debye shielding model. The effect of the plasma environment on the electrons bound in an atom is taken into account by introducing the *screened* Coulomb-type potentials into the electronic Hamiltonian of an atom in place of the standard nuclear attraction and electron repulsion potentials. The capabilities of this new Hamiltonian are demonstrated for He and Li in laser plasmas.

1 Introduction

Recent advances in ultrahigh power laser light sources has enabled us to generate a new type of plasma called *laser plasma* [1,2] in which the particle density could be as large as $10^{22} \sim 10^{25}$ cm^{-3}. It can be expected that the electronic structure of atoms in such an extremely high-density plasma could be largely perturbed owing to the Coulomb interaction among the charged particles in the plasma. Indeed, it has been reported recently that the emission lines from several atomic species in laser plasmas exhibited substantial red shifts as large as 3.7 eV [3,4].

One of the promising approaches to calculate electronic structure of atoms in such a high density plasma may be to focus on a single atom inside the plasma and simulate the surrounding plasma environment by introducing an *effective* interaction among charged particles [5,6]. By introducing an effective potential into an *N*-electron atomic Hamiltonian, the electronic structure of an atom could be evaluated in a mean-field approximation. In the present report, in order to derive the electronic structure of atoms in a laser plasma we introduce a new model Hamiltonian based on the Debye-Hückel theory [5,7,8].

2 The Debye-shielding model

In the classical theory of plasmas developed by Debye and Hückel, the interaction potential between two charged particles in a plasma is expressed by a Yukawa-type potential [5],

$$\phi(\mathbf{r}_a,\mathbf{r}_b)=\frac{Z_a Z_b}{|\mathbf{r}_a-\mathbf{r}_b|}\exp(-\mu\,|\mathbf{r}_a-\mathbf{r}_b|), \tag{1}$$

where $\mathbf{r}_a$ and $\mathbf{r}_b$ represent the spatial coordinates of the particles A and B, and Z_a and Z_b denote their charges. By comparing Eq. (1) with a Coulombic potential, it is understood that a plasma effect is incorporated into a shielding parameter μ describing the shape of the long range potential. The shielding parameter μ in the exponential decay factor is given as

$$\mu \quad = \sqrt{\frac{2e^2 n}{\varepsilon_0 kT}} \tag{2}$$

as a function of the temperature T and the particle density n of the plasma. In typical laser plasma conditions, $T \sim 1$ keV and $n \sim 10^{22}$ cm^{-3}, the μ parameter takes a value of the order of 10^{-1} in atomic unit.

By introducing the Yukawa-type nuclear attraction and electron repulsion potentials, the electronic Hamiltonian for an N-electron atom in a plasma is thus given in atomic unit as

$$H(\mathbf{r})=\sum_{i=1}^{N}\left[-\frac{1}{2}\nabla_i^2\right]+\sum_{i=1}^{N}\left[-\frac{Z}{|\mathbf{r}_i|}\exp\left(-\mu|\mathbf{r}_i-\mathbf{r}_j|\right)\right]+\sum_{i>j}^{N}\left[\frac{1}{|\mathbf{r}_i-\mathbf{r}_j|}\exp\left(-\mu|\mathbf{r}_i-\mathbf{r}_j|\right)\right]. \tag{3}$$

A standard quantum chemical program is modified so that it could treat the Yukawa-type one-electron and two-electron potentials introduced in Eq. (3). The total electronic energy and wavefunction of the system are calculated as the eigenvalue and eigenvector of the configuration interaction (CI) matrix of the Hamiltonian (3). A full CI and a multi-reference CI are adopted for He and Li, respectively.

A basis set needs to be designed carefully to describe a system in which the electrons are bound by a non-Coulombic potential. In the present study a large spherical Gaussian basis set consisting of s-, p-, and d-type functions is constructed using a universal basis set approach [9]. The optimal basis set is optimized so that a convergence of the electronic energies is achieved.

The total electronic energies of the low-lying states of He and Li are calculated in the range of $0.0 \le \mu \le 0.15$. It is found in both cases of He and Li that the electronic energy increases for all the electronic states as the μ parameter increases, while the relative energy measured from the electronic ground state decreases largely. This means that a substantial red shift is expected for the transition peaks in the emission spectra of atoms in a plasma. This interprets well the previous experimental reports on multiply charged atoms in laser plasmas [3,4].

Acknowledgments

The present study was supported by the fund from Japan Science and Technology Corporation and by the following grants from the Ministry of Education, Culture, Sports, Science and Technology, Japan; Grant-in-aid for Scientific Research in Priority areas, “Control of Molecules in Intense Laser Fields” (#14077205), Grant-in-aid for the 21st Century COE program for Frontiers in Fundamental Chemistry (Univ. of Tokyo).

References

[1] W.L. Kruer, Phys. Plasmas 10 (2003) 2087.
[2] F. Amiranoff, Meas. Sci. Technol. 12 (2001) 1795.
[3] O. Renner, D. Salzmann, P. Sondhauss, A Djanoui, E. Krouský, E. Förster, J. Phys. B: At. Mol. Opt. Phys. 31 (1998) 1379.
[4] A. Saemann, E. Eidmann, I.E. Golovkin, R.C. Mancini, E. Andersson, E. Förster, K. Witte, Phys. Rev. Lett. 82 (1999) 4843.
[5] P. Debye and E. Hückel, Physikalische Zeitschrift 24 (1923) 185.
[6] H. Nguyen, M. Koenig, D. Benredjem, M. Caby, G. Coulaud, Phys. Rev. A 33 (1986) 1279.
[7] X. Lopez, C. Sarasola, J.M. Ugalde, J. Phys. Chem. A 101 (1997) 1804.

[8] D. Ray, P.K. Mukherjee, J. Phys. B 31 (1998) 3479.

[9] S. Wilson, Electron Correlation in Molecules, Clarendon, Oxford, 1984.

Superexcited states studied by angle-resolved electron energy loss spectroscopy

Zhi-Ping Zhong[1], Jian-Min Sun[2],Lan-Lan Fan[2], Lin-Fan Zhu[2], Xiao-Jing Liu[2], Zhen-Sheng Yuan[2], Ke-Zun Xu[2]

[1]Department of Physics, Graduate School of the Chinese Academy of Sciences, P.O.Box 3908, Beijing 100039, China

[2]Laboratory of Bond--Selective Chemistry, Department of Modern Physics, University of Science and Technology of China, Hefei, Anhui, 230027, China

Abstract

Absolute double differential cross section density (DDCS) spectra of NO below 135 eV and O2 below 119 eV have been determined by an angle-resolved electron-energy-loss spectrometer with an incident electron energy of 2500 eV and an energy resolution of 100 meV [full width at half maximum (FWHM)]. Some features above the first ionization threshold, which are too weak to be observed in the photoabsorption spectrum, stand out at large scattering angles.

I. Introduction

Superexcited states, i.e., excited states of molecules above the first ionization threshold such as high Rydberg states, doubly or inner-shell excited, non-Rydberg states, and etc.[1,2,3], are fragmental due to the low cross sections and the difficulties in achieving required energy resolution. There are increasing interest about the dynamics of superexcited states because superexcited states play an important role as reaction intermediates in a variety of collision processes such as electron-ion, ion-ion recombination, penning ionization and electron attachment processes[1,2,4]. The three most common methods to investigate the structure of superexcited states are the photoelectron spectroscopy, photoion spectroscopy and fluorescence spectroscopy emitted from neutral fragments, each of which is related to one specific decay path of superexcited states. However, the spectra measured by angle-resolved electron-energy-loss spectroscopy include all possible decay paths for a specific state. Since the momentum transfer dependence of superexcited states are different, some superexcited states may stand out at large scattering angles. This is elucidated by recent work[5]. Therefore, angle—resolved electron--energy-loss spectroscopy with high energy resolution may provide helpful information for the structure and nature of superexcited states. This is our main interest in this paper.

II. Experimental Method

The angle-resolved electron-energy-loss spectrometer used in this experiment has been described in detail in Refs.[6,7,8]. Briefly, it consists of an electron gun, a hemispherical electrostatic monochromator made of aluminium, a rotable energy analyzer of the same type, an interaction chamber, a number of cylindrical electrostatic lenses, and an one--dimension position sensitive detector for detecting the scattered electrons. All of these components are enclosed in four separate vacuum chambers made of stainless steel. The impact energy of the spectrometer can be varied from 1 to 5 keV. For the present experiment it was set at 2.5 keV and the energy resolution was about 100 meV (FWHM). The angular resolution was about 0.8^o (FWHM) at present.

The spectrum measured at a mean angle of 0^O was converted into relative OOSD spectrum by multiplying the Bethe--Born conversion factor of the spectrometer [6,9]. The spectra at other scattering angles were converted into relative generalized oscillator strength density (GOSD) spectra, which is defined as (in atomic units)[10]

$$\frac{df(E,K)}{dE}=\frac{E}{2}\frac{p_0}{p_a}K^2\frac{d^2\sigma}{dEd\Omega},$$

where df(E,K)/dE and $d^2\sigma/dEd\Omega$ stand for relative GOSD and double differential cross section, respectively. E and K are the excitation energy and momentum transfer while p_0 and p_a are the incident and scattered electron momentum, respectively.

These relative GOSD spectra were made absolute independently by using the valence shell Bethe sum-rule[10,11]:

$$S_{val}(0) = N_{val} + N_{PE} = \int_{E'}^{\infty} \frac{df}{dE} dE,$$

where N_{val} is the total number of valence electrons in the target (11 for NO, 12 for O_2), N_{PE} is a small estimated correction (0.32 for NO,0.42 for O_2) of the Pauli--excluded transitions from the K shells to the already occupied valence shell orbitals [12,13], and E' is the lowest excitation energy. In the limit K→0, the relative GOSD is identical to the relative OOSD and the valence Thomas-Reiche-Kuhn (VTRK) sum-rule was used.

III. Results and Discussions

Figure 1 and 2 exhibit absolute double differential cross section spectra at scattering angles of 0^o, 2^o, 4^o,6^o and 8^o for NO and O_2, respectively.. Note that with the increasing of K^2, the energy position of the very broad feature, i.e., the Bethe ridge, moves to higher energy loss and the corresponding width becomes more diffuse. Such phenomena have also been observed in other molecules. Furthermore, some features stand out at large scattering angles. Through the comparison with the corresponding photoelctron spectroscopy, photoion spectra and fluorescence spectra, some of these features are firstly observed. Based on the multiple-scattering self-consistent-field (MSSCF) method, β feature in NO spectra and C feature in O_2 result from the inner-valence transition. More specifically, The calculated energy position for $2\pi \leftarrow 3\sigma$ of NO is 32.4 eV, which is close to the observed energy position 33 eV of β feature, and the calculated energy position for $1\pi_g \leftarrow 2\sigma_g$ of O_2 is 27.99 eV, which is close to the observed energy position 28.8 eV of C feature. As shown in figures 3 and 4, the calculated GOSs for the two transitions show the existence of a minimum followed by a maximum. Such GOS behavior would result in the corresponding feature stands out at large momentum transfers. Other features (α band for NO, A and B bands for O_2) may be assigned to high Rydberg states and doubly excited states. Further work is being done.

As elucidated in this paper, angle-resolved electron-energy-loss spectroscopy include all possible decay paths for a specific state, and some superexcited states may stand out at large scattering angles. Therefore, it is an important method supplementary to the three most common methods to investigate the structure of superexcited states, i.e., the photoelectron spectroscopy, photoion spectroscopy and fluorescence spectroscopy of neutral atomic fragments, each of which is related to one specific decay path of superexcited states.

Supports of this work by National Nature Science Foundation of China (10134010, 10004010) and the Youth Foundation of the University of Science and Technology of China are gratefully acknowledged.

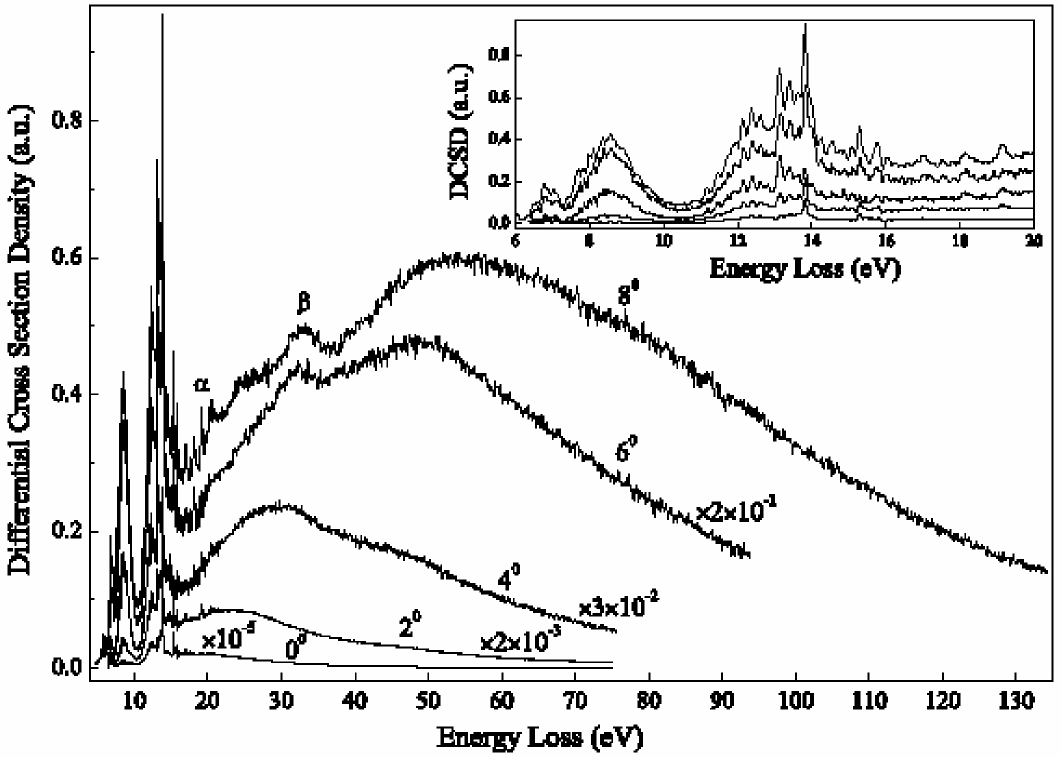

Figure 1 Absolute double differential cross section density of NO below 135 eV. α and β denote some features standing out at large scattering angle. The inset figure shows the expanded spectra in the energy region 6-20 eV.

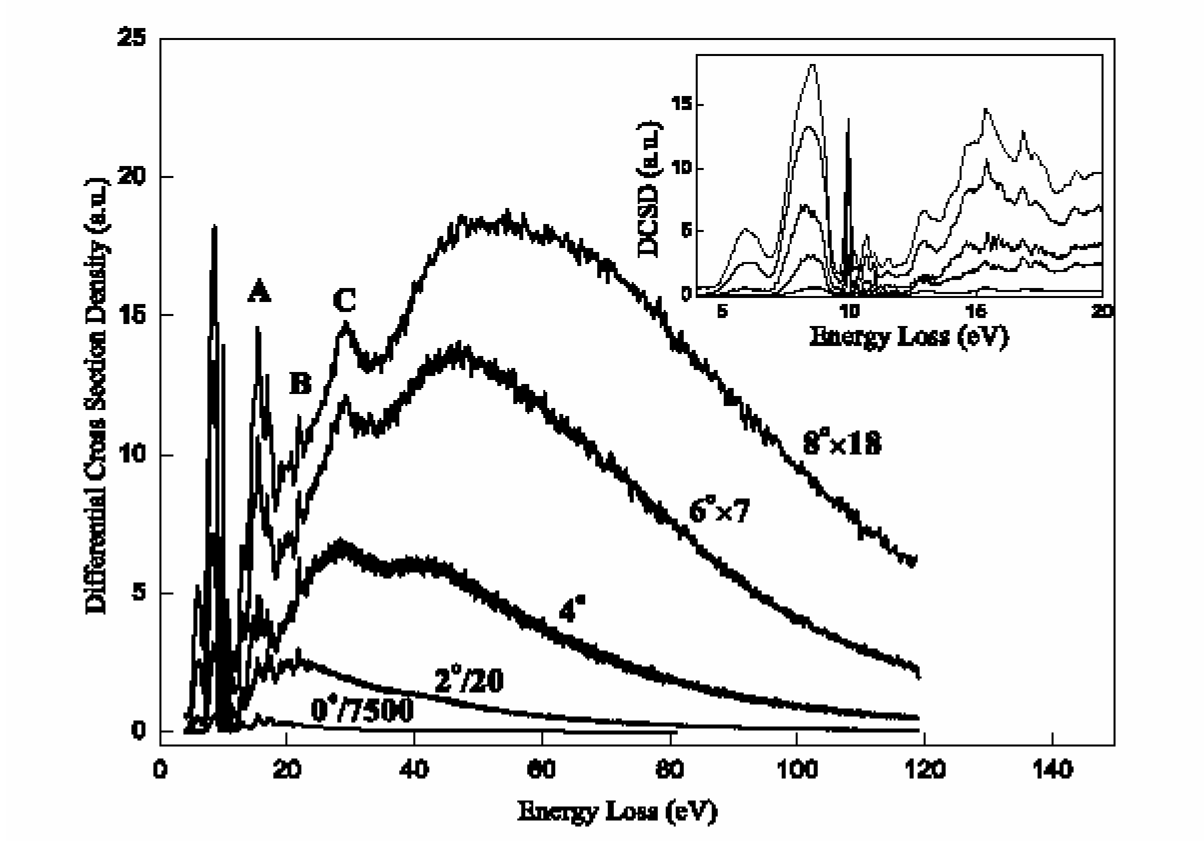

Figure 2 Absolute double Differential cross section of O_2 120 eV. A,B,and C denote some features standing out at large scattering angle. The inset figure shows the expanded spectra in the energy region 4-20 eV.

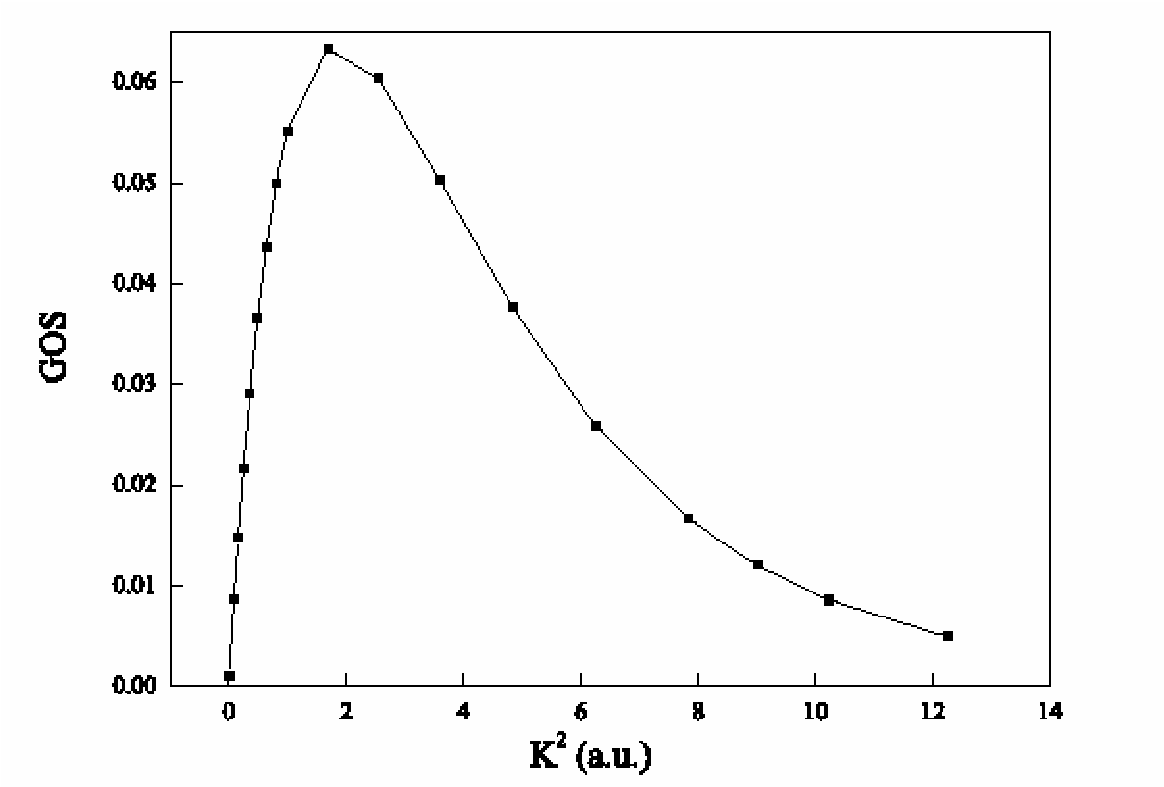

Figure 3 The calculated GOS for $2\pi \leftarrow 3\sigma$ transition of NO.

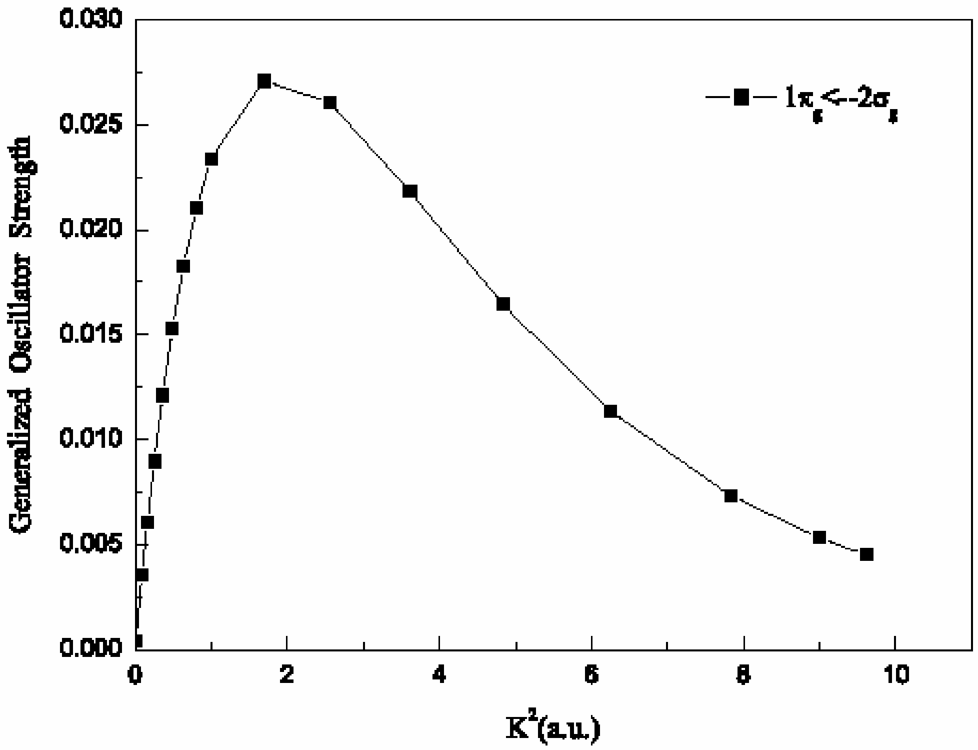

Figure 4 The calculated GOS for $1\pi_g \leftarrow 2\sigma_g$ transition of O_2.

[1] R. L. Platzman, Radiat. Res. **17**, 419(1962).

[2] R. L. Platzman, Vortex **23**, 372(1962).

[3] Y. Hatano, Phys. Rep. **313**, 109(1999).

[4] Y. Hatano, Radiation Physics and Chemistry **67**, 187(2003).

[5] Z. P. Zhong, X. Y. Han, W. H. Zhang, and J. M. Li, Chin. Phys. lett. **21**, 279(2004).

[6] S. L. Wu, Z. P. Zhong, R. F. Feng, S. L. Xing, B. X. Yang, and K. Z. Xu, Phys. Rev. A **51**, 4494(1995).

[7] K. Z. Xu, R. F. Feng, S. L. Wu, Q. Ji, X. J. Zhang, Z. P.Zhong, and Y. Zheng, Phys. Rev. A **53**, 3081(1996).

[8]X. J. Liu, L. F. Zhu, X. M. Jiang, Z. S. Yuan, B. Cai, X. J. Chen, and K. Z. Xu, Rev. Sci. Instrum. **72**, 3357(2001).

[9] W. F. Chan, G. Cooper, and C. E. Brion, Phys. Rev. A **44**, 186(1991).

[10] M. Inokuti, Rev. Mod. Phys. **43**, 297 (1971).

[11] Terry N. Olney, N. M. Cann, Glyn Cooper, C. E. Brion, Chem. Phys. **223**, 59(1997).

[12] J. A. Wheeler and J. A. Bearden, Phys. Rev. **46**,755(1934).

[13] J. L. Dehmer, M. Inokuti and R. P. Saxon,Phys. Rev. A **12**, 102(1975).

(e,2e) ionization-excitation experiment
with fixed-in-space H_2 molecules

M. Takahashi [a,b,*], N. Watanabe [a,b], Y. Khajuria [a], Y. Udagawa [b], and J.H.D. Eland [c]

[a] *Institute for Molecular Science, Okazaki 444-8585, Japan*
[b] *Institute of Multidisciplinary Research for Advanced Materials, Tohoku University,*
Sendai 980-8577, Japan
[c] *Physical and Theoretical Chemistry Laboratory, Oxford University,*
Oxford OX1 3QZ, United Kingdom
*Corresponding author: masahiko@ims.ac.jp, masahiko@tagen.tohoku.ac.jp (M. Takahashi)

ABSTRACT

This report will introduce an electron-electron-fragment ion triple coincidence spectrometer to the readers with our recent collision dynamics study on ionization-excitation processes of the hydrogen molecule. Following a description of the working principle of the spectrometer, results of the study will be discussed; this includes molecular frame (e,2e) cross sections that have been observed for the first time.

Keywords: (e,2e); ionization-excitation; fixed-in-space H_2 molecules; triple coincidence

1 Introduction

Through the last three decades of studies of binary (e,2e) spectroscopy or electron momentum spectroscopy (EMS), it has been demonstrated that the ionization reaction near the Bethe ridge is a sensitive probe for electronic structure and electron correlation [1]. The method involves coincident detection of the two outgoing electrons produced by the binary (e,2e) reaction. The ion recoil momentum $\boldsymbol{q}$ and the electron binding energy E_{bind} can be determined by coincident detection of the two outgoing electrons with the help of the laws of conservation of linear momentum and energy:

$$\boldsymbol{q} = \boldsymbol{p}_0 - \boldsymbol{p}_1 - \boldsymbol{p}_2 \tag{1}$$

and

$$E_{\mathrm{bind}} = E_0 - E_1 - E_2 \,. \tag{2}$$

Here the $\boldsymbol{p}_{\mathrm{j}}$'s and E_{j}'s (j=0,1,2) are momenta and kinetic energies of the incident and two outgoing electrons, respectively. Under the high-energy Bethe ridge conditions [1-4], the collision kinematics can be described by the so-called electron Compton scattering [5], analogous to X-ray Compton scattering, that most nearly corresponds to collision of two free electrons with the residual ion acting as a spectator. Then the momentum of the target electron before ionization $\boldsymbol{p}$ is equal in magnitude but opposite in sign to the ion recoil momentum $\boldsymbol{q}$.

$$\boldsymbol{p} = -\boldsymbol{q} = \boldsymbol{p}_1 + \boldsymbol{p}_2 - \boldsymbol{p}_0 \tag{3}$$

Thus EMS cross section can be measured as a function of binding energy and target electron momentum, providing full electronic structure information on atoms and molecules. In other words, EMS allows us to observe individual molecular orbitals in momentum space.

In spite of the remarkable feature of the technique, however, EMS has not yet reached the stage of full use of its ability for intensive investigation on electronic structure of molecules. The reason for this may have been twofold; (1) a more complete knowledge of the binary (e,2e) reaction mechanism is an ever-increasing necessity as sophistication of experiments increases, and (2) the present EMS experiments measure averages over all orientations of gaseous molecules, resulting in enormous loss of information on electronic structure, anisotropy of the target wavefunction in particular. However, small cross section involved in the binary (e,2e) reaction has hindered one from developing EMS satisfactorily.

Under these circumstances, we have constructed an electron-electron-fragment ion triple coincidence spectrometer [6]. The spectrometer features remarkably high sensitivity for the two outgoing electrons by simultaneous detection in energy and momentum, and further it enables us to carry out (e,2e) experiments with fixed-in-space linear target molecules for discussing scattering in the molecular frame. In the present paper, details and performance of the spectrometer are presented, together with our recent collision dynamics study on ionization-excitation processes of the hydrogen molecule.

2 Electron-electron-fragment ion triple coincidence spectrometer

In Fig. 1 we show a schematic diagram of the symmetric noncoplanar geometry that has been widely used for EMS experiments. In this kinematic scheme, two outgoing electrons having equal energies (E_1=E_2) and making equal polar angles (θ_1=θ_2=45°) with respect to the incident electron beam axis are detected in coincidence. Then magnitude of the ion recoil momentum q is expressed by

$$q = \sqrt{\left(p_0 - \sqrt{2}p_1\right)^2 + \left(\sqrt{2}p_1 \sin(\Delta\phi/2)\right)^2} \tag{4}$$

where $\Delta\phi$ (=ϕ_1−ϕ_2+π) is the out-of-plane azimuthal angle difference between the two outgoing electrons. Basically, EMS probes the momentum component perpendicular to the incident electron momentum vector. Thus, by detecting dissociation of the molecular ion perpendicular to the incident electron beam axis, three-dimensional momentum densities can be determined from the measurements of vector correlations among the two outgoing electrons and the fragment ion, because the linear target has rotation symmetry about the molecular axis.

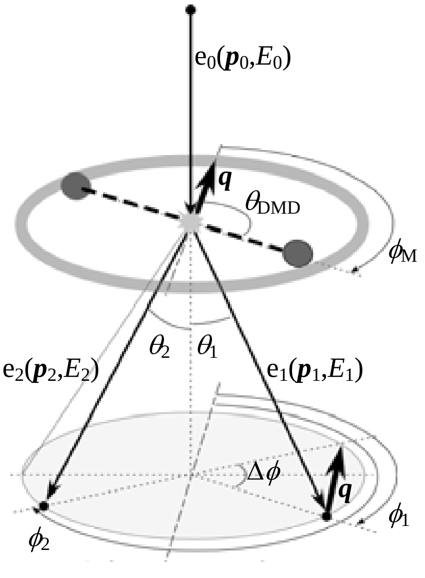

Fig. 1. Symmetric noncoplanar geometry for the binary (e,2e) reaction.

Fig. 2 shows a schematic of the electron-electron-fragment ion triple coincidence spectrometer. Major sections of the spectrometer are an electron gun, a sample inlet system with eight nozzles, seven ion-channel-detectors, a spherical analyzer, and two position-sensitive detectors (PSDs). Except for the use of the ion detectors, the present (e,2e+M) spectrometer is essentially the same as our (e,2e) spectrometer [7] which features high sensitivity by taking advantages of multiparameter techniques. Briefly, incident electron beam is produced by the electron gun incorporating a tungsten filament and is collected with the Faraday cup. Electron impact ionization occurs where the incident electron beam collides with targets from the multi-nozzles. Scattered electrons leaving the ionization point are limited by a pair of apertures so that the spherical analyzer accepts those with θ=45° over the azimuthal angle ϕ_1 and ϕ_2 ranges from 70 to 110° and from 250 to 290°. The electrons passing through the apertures are energy analyzed and dispersed by the analyzer, and then detected by the two PSDs placed behind the exit. Since a spherical analyzer maintains azimuthal angles for the electrons, both energies and angles can be determined from their arrival positions at the detectors. Furthermore, if the incident electron energy E_0 and momentum $\boldsymbol{p}_0$ are fixed, a given ionization transition (E_{bind}) can be selected simply by the choice of detection energy (E_1=E_2) and then magnitude of the ion recoil momentum can be determined only by the azimuthal angle difference. Thus, by combining a spherical analyzer with PSDs, it is possible to sample the EMS cross sections over a wide range of binding energy and ion recoil momentum simultaneously. This technique significantly improves sensitivity and accuracy of the data compared with the conventional single channel measurements, as drifts in electron beam current and fluctuations in target gas density affect all channels in the same way.

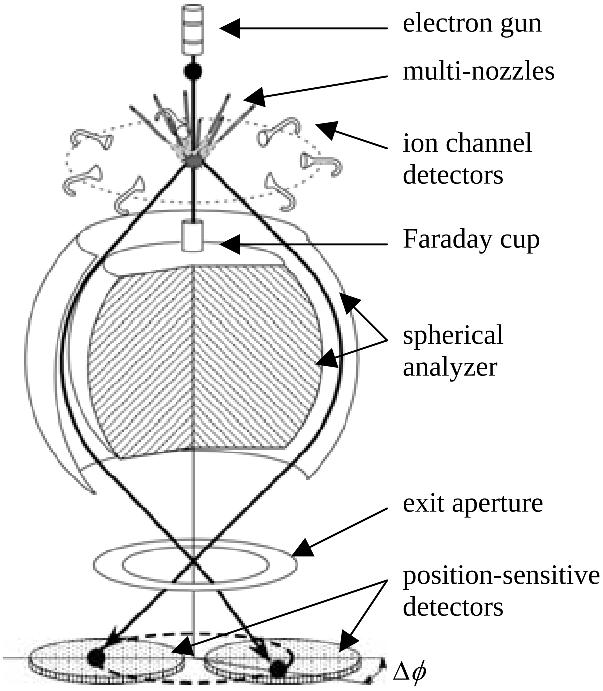

Fig. 2. Schematic of an electron-electron-fragment ion triple coincidence spectrometer.

Fragment ions are detected by an array of the seven ion-channel-detectors that are placed at ion azimuthal angle ϕ_M of 0, 45, 90, 150, 195, 240, and 285° in the perpendicular plane. This arrangement corresponds to covering full 2π in the perpendicular plane at 15° intervals in the case of homonuclear diatomic targets that have the inversion symmetry and rotation symmetry about the molecular axis. The same is true for heteronuclear targets when the mass resolution is sufficient to separate individual fragment ion species. In front of each detector, a retarding electric field is applied to collect only axial-recoil fragments with large translational energies. Kinetic energy of the fragment ion detected can be obtained from its time-of-flight.

3 Ionization-excitation processes of H_2

The show case measurements have been made for ionization-excitation processes of H_2 that leave the residual ion in excited state of H_2^+, under experimental conditions where a retarding voltage of 2.5 V and an impact energy of 1200 eV have been employed. There are three motivations behind this. First, the two electron system H_2 is the simplest molecule that is always the subject of accurate calculations. Secondly, as all the transitions to the final excited ion states are followed by direct dissociation, their axial recoil fragmentation is unambiguous. The use of the 2.5 V retarding voltage ensures that energetic fragments H^+ from the excited ion states are detected but those from the $1s\sigma_g$ ground ion state with up to 1eV kinetic energy are entirely removed from the detection [8-10]. Thirdly, it has been found from our previous EMS study on ionization-excitation of H_2 [11] that the second-order two-step mechanism [12,13] plays a crucial role for understanding of the striking discrepancies between first-order plane-wave impulse approximation (PWIA) calculations and experiment observed at the impact energy of 1200 eV. The two-step mechanism, which leads to a joint change of state of the two target electrons, involves two successive half-collisions, a single (e,2e) ionization process and a single excitation process. Thus contribution of the mechanism to the (e,2e) cross section must show stereo dynamics in the binary (e,2e) reaction. For example, the Dunn selection rules [14] about electronic transitions by electron impact may work at the single excitation process involved. The (e,2e+M) experiments of H_2 are therefore expected to reveal geometry effect on the molecular frame (e,2e) cross section.

3. 1 Three-dimensional time spectrum

A three-dimensional time spectrum obtained is shown in Fig. 3, which represents arrival time difference between the two outgoing electrons Δt_{ee} and that between either of the electrons and the H^+ fragment Δt_{eM}. Since the three charged particles that we want to detect are produced in a single event, they must have correlation in arrival time. Certainly we see the sharp, true coincidence peak centered at Δt_{ee}~0 and Δt_{eM}~1000 ns. Substantial background is due to false coincidences that correspond to detection of uncorrelated electrons and ions at nearly the same time. This originates mainly from a huge number of fragment ions by forward scattering of the electron projectile, which are not distinguishable from the relatively few fragments produced by the binary (e,2e) reaction. Despite the experimental difficulty, however, time correlations among the three charged particles have been successfully observed by accumulation of data for 3 months runtime.

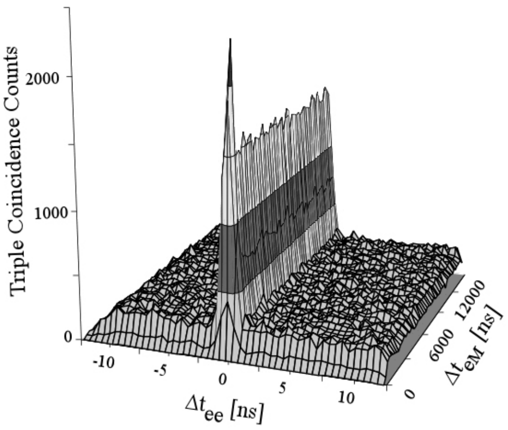

Fig. 3. Three-dimensional time spectrum.

3. 2 Binding energy spectra

Further evidence for our successful experiment is given by constructing binding energy spectra from the genuine triple coincidence events. Fig. 4 shows an (e,2e+M) binding energy spectrum that has been obtained by integrating all the true triple coincidence intensities over both of the azimuthal angle difference and ion azimuthal angle ranges covered. Also included in the figure is the corresponding (e,2e) spectrum that also has been obtained from the (e,2e+M) data but has been constructed from contributions of accidental coincidence detection of the fragment ions with the two outgoing electrons detected in true coincidence. Here the (e,2e) spectrum is scaled so that it has almost the same intensity in the ionization-excitation region as that of the (e,2e+M) spectrum for ease of comparison.

It is evident from Fig. 4 that the structure of the (e,2e+M) spectrum is as expected; since the relatively small kinetic energy fragments from the $1s\sigma_g$ ground ion state are not involved in the present (e,2e+M) data, the $1s\sigma_g$ band with the conspicuously large intensity in the (e,2e) spectrum has totally disappeared and contributions of the ionization-excitation become prominent. This confirms us in unwavering confidence that successful measurements of vector correlations between the two outgoing electrons and the fragment ion can and have been achieved.

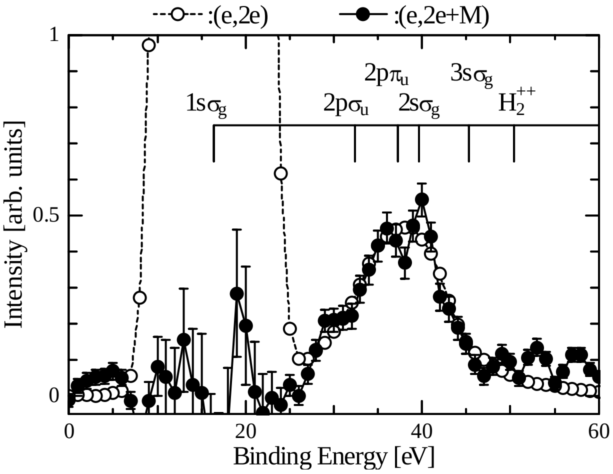

Fig. 4. Experimental (e,2e) and (e,2e+M) binding energy spectra of H_2 obtained at an impact energy of 1200 eV.

Also evident from the figure is that the ionization-excitation structures of the two spectra are similar to each other. This may be surprising in terms of stereo dynamics of collision. As discussed above, the present (e,2e+M) experiment is restricted to measurements of collision between the electron projectile and molecular targets with orientation perpendicular to the incident electron beam axis. Hence the (e,2e+M) binding energy spectrum, integrated over the ion azimuthal angles, approximately represents averages over all perpendicular orientations of the targets. Thus, by considering that the two-step mechanism should be sensitive to the orientation of the target with respect to the incident and outgoing electron momentum vectors, one may expect that the (e,2e+M) spectrum may be different from the completely spherically-averaged (e,2e) spectrum. Against this expectation, however, the present results show that there are no discrepancies between the two spectra within the experimental uncertainties. The (e,2e+M) experiments for the targets with various orientations are clearly called for.

3. 3 *Molecular frame (e,2e) cross sections*

Finally, we present molecular frame (e,2e) cross sections of H_2 in Fig. 5. The experimental cross sections have been obtained by summing all the ionization-excitation intensities of an (e,2e+M) binding energy spectrum over the entire azimuthal angle difference range and by repeating this procedure for a series of spectra at the seven ion azimuthal angles. In the figure, the inversion symmetry and the rotation symmetry about the molecular axis are assumed for the (e,2e) cross sections and the results are plotted so that distance from the origin to the data point represents relative magnitude of the cross section with the molecular axis being in the vertical direction. To our best knowledge, this is the first observation of (e,2e) cross sections from fixed-in-space molecules.

Also included in the figure are PWIA calculations that are shown by the solid line. In the calculations contributions from the dominant $2s\sigma_g$ and $2p\sigma_u$ ionization-excitation transitions [11,15,16] only are considered. The experimental and theoretical molecular frame (e,2e) cross sections are placed on a common scale by using the ratio of the sum of the spherically-averaged ionization-excitation intensities integrated over the entire momentum range, to that of theory [6]. Although the statistics of the data are not satisfactory, it can be seen that the experiment exhibits larger cross section than theory at every ion azimuthal angle. Furthermore, we clearly see some anisotropy of the molecular frame (e,2e) cross sections; the experiment shows more significant deviation from theory in the direction of the molecular axis.

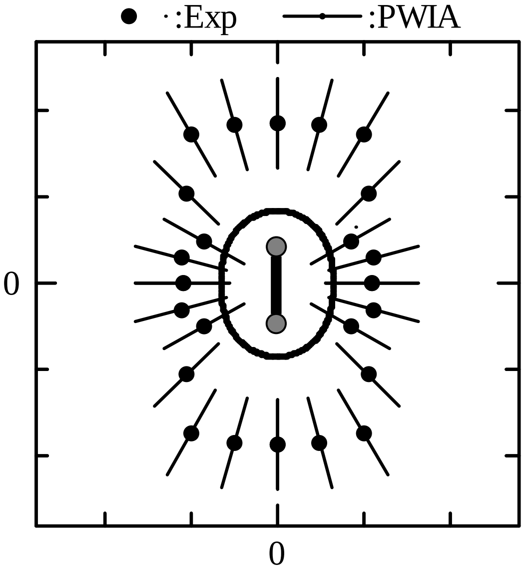

Fig. 5. Comparison of experimental and theoretical Molecular frame (e,2e) cross sections for H_2. The molecular axis is in the vertical direction.

If this observation is real, it would indicate that the two outgoing electrons escape preferentially so as to leave the ion recoil momentum vector along the molecular axis. In other words, roughly speaking, the binary (e,2e) reaction favors molecular orientation perpendicular to the scattering plane, defined by the incident and outgoing electron momentum vectors, rather than parallel. Since extent of the intensity difference from the first-order PWIA calculations would be a rough measure of contributions from the second-order two-step mechanism, the present results must reveal strong geometry effect of molecular orientation in the mechanism. However, we leave full discussion of it for later publication, because further attempt is now in progress to obtain the molecular frame (e,2e) cross sections for individual ionization-excitation transitions separately and to examine the observation more closely [17]. A preference for the larger (e,2e) cross section along the molecular axis is expected to be much more prominent for the $2p\sigma_u$ channel than for $2s\sigma_g$ [11].

In short, a new method for complete imaging of directional momentum densities has been proposed for molecules, based on the axial recoil fragmentation. Our apparatus demonstrates that the capability to measure vector correlations among the two outgoing electrons and the fragment ion simultaneously is a useful advance for (e,2e) and it has already been used to explore the phenomenon of H_2 for which detailed theoretical explanations are eagerly awaited.

Acknowledgements

One of the authors MT gratefully thanks the organizing committee for giving him the opportunity to be involved in the exciting China/Japan Joint Symposium on Atomic and Molecular Processes in Plasma (Lanzhou, 2004 March 6-11). This research was partially supported by the Ministry of Education, Science, Sports and Culture, Grant-in-Aid's for Scientific Research (B), 13440170, 2001 and for Exploratory Research, 14654069, 2002.

References

[1] I.E. McCarthy and E. Weigold, Phys. Rept. C **27** (1976) 275.
[2] C.E. Brion, Int. J. Quantum Chem. **29** (1986) 1397.
[3] M.A. Coplan, J.H. Moore, and J.P. Doering, Rev. Mod. Phys. **66** (1994) 985.
[4] E. Weigold and I.E. McCarthy, *Electron Momentum Spectroscopy* (Kluwer Academic /Plenum Publishers, New York, 1999).
[5] R.A. Bonham and H.F. Wellenstein, in: B. Williams (Ed.), *Compton Scattering* (McGraw-Hill, New York, 1977).
[6] M. Takahashi, N. Watanabe, Y. Khajuria, K. Nakayama, Y. Udagawa, and J.H.D. Eland, J. Electron Spectrosc., submitted.
[7] M. Takahashi, T. Saito, M. Matsuo, and Y. Udagawa, Rev. Sci. Instrum. **73** (2002) 2242.
[8] A.K. Edwards, R.M. Wood, J.L. Davis, and R.L. Ezell, Phys. Rev. A **42** (1990) 1367.
[9] K. Ito, R.I. Hall, and M. Ukai, J. Chem. Phys. **104** (1996) 8449.
[10] Y. Hikosaka and J.H.D. Eland, Chem. Phys. **277** (2002) 53.
[11] M. Takahashi, Y. Khajuria, and Y. Udagawa, Phys. Rev. A **68** (2003) 042710.
[12] T.A. Carlson and M.O. Krause, Phys. Rev. **140** (1965) 1057.
[13] R.J. Tweed, Z. Phys. D **23** (1992) 309.
[14] G.H. Dunn, Phys. Rev. Lett. **8** (1962) 62.
[15] E. Weigold, I.E. McCarthy, A.J. Dixson, and S. Dey, Chem. Phys. Lett. **47** (1977) 209.
[16] N. Lermer, B.R. Todd, N.M. Cann, Y. Zheng, C.E. Brion, Z. Yang, and E.R. Davidson, Phys. Rev. A **56** (1997) 1393.
[17] M. Takahashi, N. Watanabe, Y. Khajuria, and Y. Udagawa, to be submitted to Phys. Rev. Lett.

ELECRON AND MOLECULAR ION COLLISIONS RELEVANT TO DIVERTOR PLASMA

H. Takagi

Center for Natural Science, Kitasato University,
1-15-1 Kitasato, Sagamihara, Kanagawa, 228-8555 Japan

Abstract

We introduce the concept of the multi-channel quantum defect theory (MQDT) and show the outline of the MQDT newly extended to include the dissociative states. We investigate some molecular processes relevant to the divertor plasma by using the MQDT: the dissociative recombination, dissociative excitation, and rotational-vibrational transition in the hydrogen molecular ion and electron collisions.

1. INTRODUCTION

As the research of fusion plasma is extending to the low temperature plasma like the detached plasma in the gas divertor, data of molecular processes are required. For example, the dissociative recombination (DR) process is indispensable in the molecular assisted recombination in edge plasma. The DR of hydrogen molecular ion is

$$H_2^+(v, N) + e \longrightarrow H(1s) + H(nlm),$$

where v and N respectively indicates the vibrational and rotational state and n, l, and m are sequentially the principal, azimuthal, and magnetic quantum numbers of the electronic states. The state specific data — v, N, n dependent cross section — is quite important for the molecular assisted recombination. [1] Besides the DR, dissociative excitation (DE),

$$H_2^+(v, N) + e \longrightarrow H(1s) + H^+ + 2e,$$

and vibrational-rotational transition by electron impact,

$$H_2^+(v, N) + e \longrightarrow H_2^+(v', N') + e ,$$

are the processes of molecular ions relevant to the gas divertor. On the molecular species, the H_3^+ is important besides the hydrogen molecular ions. [1]

Since the experimental study of electron and molecular ion collisions are especially difficult to study compared with neutral molecular case, there had been few reliable data. Recently, the storage ring experiments have given much reliable and state specific cross-section (cs) of the DR, although the specific initial state is almost limited to the ground vibrational state [2]. Theoretical calculation is indispensable to compile the state specific data of those molecular processes besides the DR. It also makes clear those mechanism and systematics of the state-dependence. In this lecture, we are introducing the method of theoretical calculation, especially the concept of electron and molecular ion collisions by the multi-channel quantum defect theory (MQDT). For the theoretical calculation, the three processes listed above depend on each other: all three types of channels are coupled together. The DR has been experimentally investigated most in detail and there are most reliable experimental data on the DR. Thus, we shall begin to introduce the MQDT for the DR.

2. WHAT IS MQDT

The quantum defect theory enables a unified description on the Rydberg and electronic continuum states. It gives the relation between the quantum defect (μ) and the phase shift (δ) of the continuum electron as is $\delta = \pi\mu$ at the zero energy. The quantum defect, of course, presents the energy of the Rydberg state E.

$$E = E_{ion} - \frac{1}{2(n-\mu)^2},$$

where E_{ion} denotes the energy of the ion, n is the principal quantum number of the Rydberg state, and we employ atomic units hereafter. The phase shift represents the electron scattering by the ion core. The reactance matrix (K) is given by $K = \tan\delta$.

The essential idea of the quantum defect theory is transformation relation between two good representations in inner and outer regions. The inner means the region where the strong Coulombic interaction acts and that electronic state is almost independent of the asymptotic boundary condition. In the outer region, the state is sensitive to the asymptotic boundary condition, especially whether the energy of logging electron is negative or positive. There remains only the one-center Coulombic interaction. Good basis functions for representing the inner region are two independent Coulombic functions, which are regular and singular solutions at the Coulombic center. Those of outer region are mutually independent standing Coulombic wave functions normalized on the energy. The relation of those two basis sets gives the energy eigen values and the reactance matrix, which are represented by only one invariant quantity called quantum defect. This quantum defect theory has been extended to multi-channel system by M. J. Seaton[3] and the MQDT was established formally.

In molecular system, the good basis functions of the inner region are composed of the Born-Oppenheimer expansion (adiabatic approximation). Those of the outer region are composed of the channels expanded by the target states as the close-coupling method[4]. The relation between the two basis sets is called *frame transformation*. The frame transformation gives not only the cross section of vibrational-rotational transition by the electron impact of the molecular ions but also the autoionization rate of the rotationally-vibrationally excited Rydberg state.

3. MQDT FOR THE DR

Theoretical study of DR is originated in a model proposed by D. Bates[5], where the DR starts by the capture of the incident electron into an two-electron excited state of molecules and it completes with the relaxation of that excited state by dissociation. The dotted curve assigned by $(2p\sigma_u)^2$ in Fig. 1 is the potential energy curve of the lowest two-electron excited state of hydrogen molecule. Since the two-electron excited state is not Rydberg state, we should take into account the configuration interaction (CI) between the two- and one- electron excited states separately from the MQDT. This was achieved by the 'two-step method' proposed by A. Giusti[6]. First, the basis functions diagonalizing the CI are generated, and next, those basis functions are used as the basis of the inner region of the MQDT. This method enables to take into account the non-adiabatic interaction including the Rydberg states together with the CI. The flame transformation of the MQDT enables to represent the rotational motion of the electron and molecular ion [7].

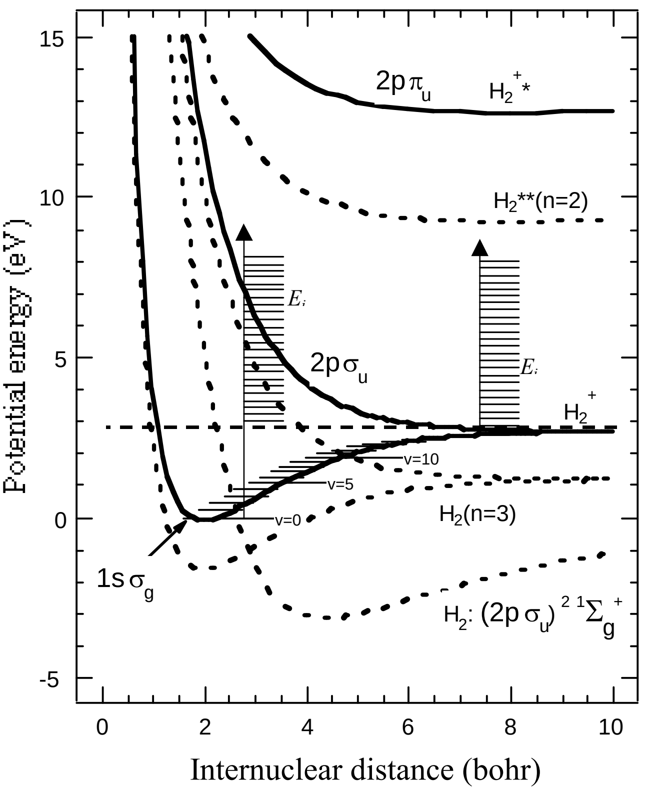

Fig. 1 Potential energy curves of hydrogen molecule and scheme of vibrational and discretized dissociative states' energies.

The reactance matrix **K** is given by the Lippmann-Schwinger equation.

$$\mathbf{K} = -\pi\mathbf{V} + \mathbf{V}\mathbf{G_0}\mathbf{K}, \tag{1}$$

where **V** denotes the matrix of the CI and $\mathbf{G_0}$ is green function for the interaction free. It has found recently that this equation can be solved stably by applying Chebyshev integral method. [8-10] . We can get the reactance matrix more easily but approximately if we adopt the first order perturbation theory, that is the first term of the right hand side of Eqn. 1.

According to the two-step method, we diagonalize the matrix **K**.

$$\sum_{\alpha',\beta'} U_{\alpha,\alpha'} K_{\alpha',\beta'}\left(E_\alpha, E_\alpha\right) U_{\beta'\beta} = -\frac{1}{\pi}\delta_{\alpha,\beta}\tan\eta_\alpha, \tag{2}$$

where η_α is eigen-pahseshift and $U_{\alpha,\alpha'}$ is the unitary matrix composed of its eigen-vectors. The frame transformation gives the invariant reactance matrix R, which smoothly depends on the energy [7],

$$\mathrm{R} = \sum_{\Lambda} G^{J\Lambda}\left(\mathrm{SC}^{-1}\right)^{JN^+\Lambda} G^{J\Lambda} \tag{3}$$

where

$$G^{J\Lambda}\left(N^+\mathbf{l}^+\right) = \sqrt{\frac{2N^+ + 1}{2J + 1}}\, C(\mathbf{l}^+ N^+ J; \Lambda - \Lambda^+, \Lambda),$$

$$G^{J\Lambda}\left(J_d \Lambda_d\right) = \delta_{J,J_d}\delta_{\Lambda,\Lambda_d},$$

$$C_{v^+\mathbf{l}^+,\alpha}^{JN^+\Lambda} = \sum \left\langle \chi_{v^+}^{N^+\Lambda^+}(R) \middle| \cos\left(\pi\mu_{\bar{\mathbf{l}}\Lambda}(R) + \eta_\alpha^{J\Lambda}\right) M_{\mathbf{l}^+\bar{\mathbf{l}}}(R) \middle| \chi_v^{J\Lambda}(R) \right\rangle U_{v\bar{\mathbf{l}},\alpha}^{J\Lambda},$$

$$C_{d,\alpha}^{JJ_d\Lambda} = \cos\left(\eta_\alpha^{J\Lambda}\right) U_{d,\alpha}^{J\Lambda}, \tag{4}$$

and S is obtained by replacing cos function to sin in the above two eqns. The adiabatic quantum defect is denoted by $\mu_{\bar{\mathbf{l}}\Lambda}(R)$ and vibrational wave function is $\chi_v^{\Lambda J}(R)$ with the total angular momentum (AM) *J*, electronic AM around the molecular axis *Λ*, and vibrational state *v*. The superscripts + means the quantity of molecular ion or incident electron, and suffix *d* indicates the quantity of the dissociative state. In the present case, the mixing matrix *M* of electronic partial waves $\mathbf{l}^+$ becomes unit matrix since we consider one partial wave *dσ* only. The reactance matrix **R**, which satisfies the boundary conditions, are given as the following.

$$R = \mathrm{R}_{\mathrm{oo}} - \mathrm{R}_{\mathrm{oc}}\left[\mathrm{R}_{\mathrm{cc}} + \tan\pi\nu\right]^{-1}\mathrm{R}_{\mathrm{co}}, \tag{5}$$

where we represent the open (closed) channel by the suffix o (c) and the energy of closed state is measured by the effective quantum number ν. The cs σ is represented using the S matrix $\mathrm{S} = (1-\mathrm{R})^{-1}(1+\mathrm{R})$, the statistical weight *ρ*, and the wave number of incident electrons *k*.

$$\sigma_{d,v^+N^+} = \frac{\pi}{k^2}\rho\sum_J \frac{2J+1}{2N^+ + 1}\sum_{\mathbf{l}^+}\left| S_{Jd,v^+N^+\mathbf{l}^+}^{J} \right|^2. \tag{6}$$

4. MQDT WITH DISSOCIATIVE CHANNELS

In order to represent the dissociation of the Rydberg states, we extend the MQDT including energy discretized dissociative states [11,12]. In the usual MQDT, only the vibrational wave functions are used for the nuclear relative motion of the molecular ion. A straightforward extension of the MQDT is to add dissociative wave functions normalized for each state as the vibrational functions, which are the energy discretized dissociative states:

$$\chi_{E_i}^{st}(R) = \frac{1}{\sqrt{\Delta}}\int_{E_i-\Delta/2}^{E_i+\Delta/2}\chi_E^{enr}(R)\,dE, \tag{7}$$

where E_i denotes the discretized energy with the integer i and $\Delta = E_{i+1} - E_i$ is constant. The superscripts *st* denotes the normalization by state and the *enr* does the normalization by energy.

We show a scheme of vibrational and discretized dissociative states' energies in fig. 1 besides the potential energy curves of hydrogen molecule. In this figure we consider two electronic states of molecular ion ($1s\sigma_g$ and $2p\sigma_u$), which contribute to the dynamics at the collision energies lower than 10 eV. There are two kinds of dissociative states associating with those two electronic states. Adopting those two discretized dissociative state to the MQDT, we represent not only the dissociation of the Rydberg states but also the DE. The dissociative states associated with the electronically excited states represent the dissociation of Rydberg manifolds of the two-electron excited states. Those highly excited two-electron excited states play an important role at the collision higher than 1 eV or for the vibrationally excited states.

The kinetic energy of the dissociating atoms becomes discrete for the definite total energy because the electronic states are discrete in the DR. The total energy is definite if we identify the initial target states and the incident energy of the electrons. There are some discretized dissociative functions which do not satisfy the energy conservation low, since we arbitrarily discretized the energy. Such unphysical dissociative functions should decay in the outer region, where the physical boundary condition must be satisfied. We call such functions closed dissociaitve channels (CDCs). In the inner region, the adiabatic states should be represented by the complete set of the functions including all bound and continuum functions. The flame transformation between the two regions is introduced for each discretized channel.

5. CALCULATION AND RESULT

5.1. DR and DE

The CI occurs between the electronic configurations constituted by the ground ($1s\sigma_g$) and the lowest excited ($2p\sigma_u$) states of the molecular ion. In the configuration of neutral molecule, the states having the largest CI matrix element V are the states of $^{1,3}\Pi_g$, $^1\Sigma_{u,g}$, $^3\Pi_u$, and $^1\Sigma_g(2p\sigma_u)^2$ according to the result by Tennyson [13]. We obtained the reactance matrix R of the lowest two-electron excited state $^1\Sigma_g(2p\sigma_u)^2$ by solving the Lippmann-Schwinger eauation (Eqn. 1) [7]. For others, the first order perturbation method was adopted.

Fig 2 shows the DR and DE of HD$^+$(v=0), where v is intial vibrational state and the rotational motion was neglected. We can see the large effect of CDC for the DE. A systematic investigation varying v is found in the reference [12].

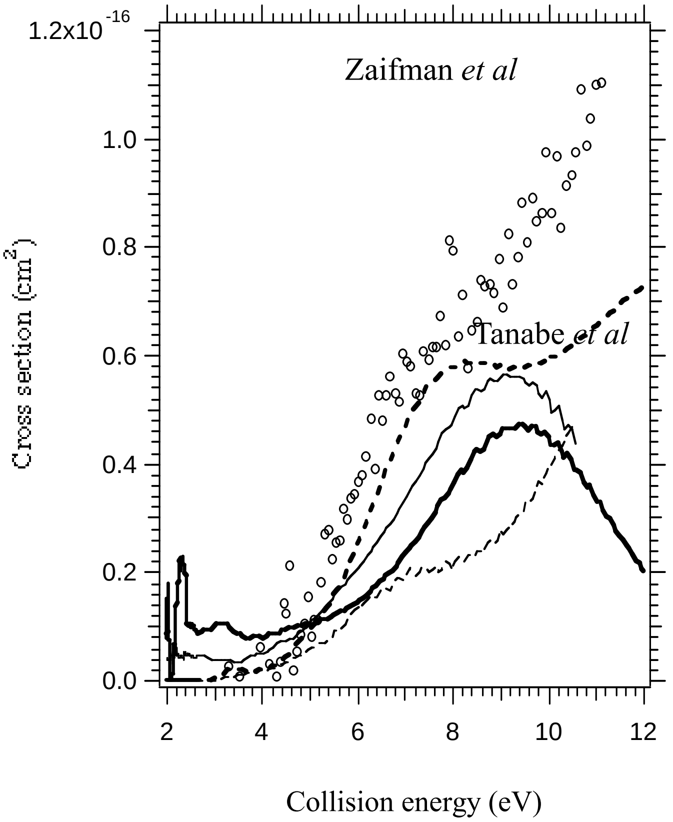

Fig. 2 DR and DE cross section of HD$^+$. The solid curves present the DR and broken one do the DE. The bold (thin) curves indicate the calculation with (without) CDC. The experiments are Tanabe *et al* [14] (DR) and Zaifman *et al* [15] (DE).

Fig. 3 shows an example of the DR cs of H$_2^+$ for v=2 and 3. The curves of smallest cs present the contribution from the lowest two-electron excited state. We can see the contribution from the higher two-electron excited states even for low v at the low collision energies. For the v higher than three, that contribution becomes over one order of magnitude. The v dependence

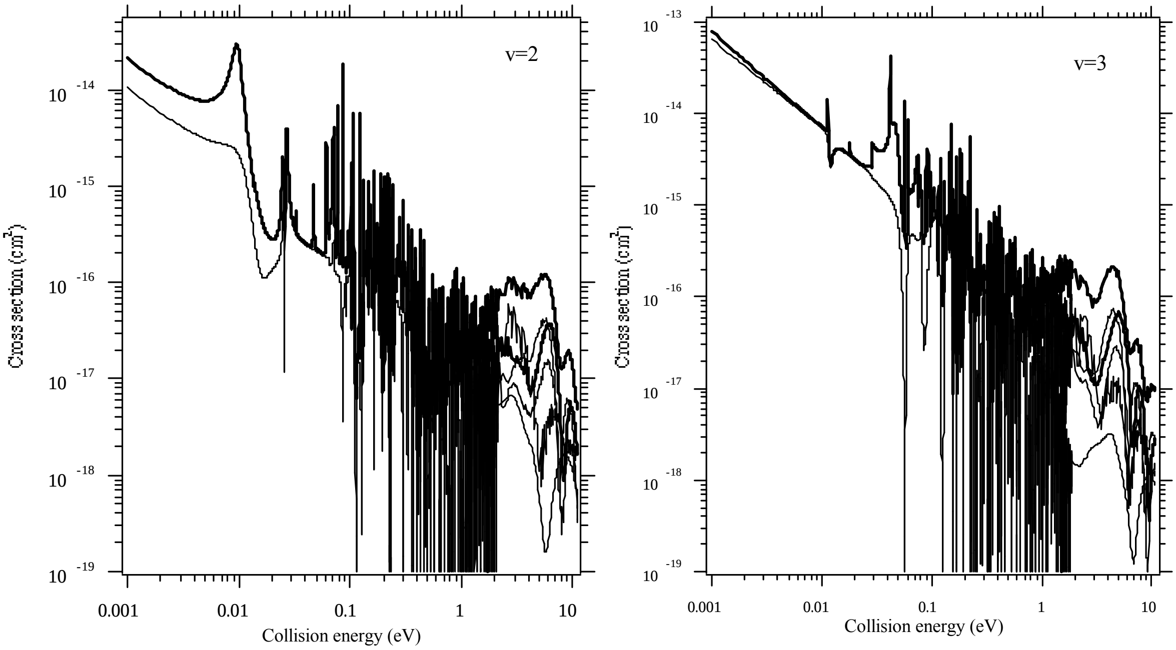

Fig. 3 DR cross section of H_2^+(v). The bold curve (largest cs) shows the total cs. The thin sold curves does the contribution from the lowest two-electron excited state. The curves between those two curves show the contribution of the two-electron excited Rydberg states of n=2, 3, 4, 5, and larger than 5.

of the DR cs is outstanding in both the magnitude and the energy dependence. The calculated DR cs has sharp resonance structure owing to the vibrationally excited Rydberg states. This structure is seen at the energies below the dissociation limit (about 3eV). Very fine resolution about 1meV is necessary in order to read the calculated cs values on the graph.

One of the hydrogen atoms of the dissociative product is in the ground electronic state, but another is in the excited state, whose principle quantum number is $n \geq 2$.

$$H_2^+(v) + e \longrightarrow H(1s) + H(n \geq 2)$$

The product of $n = 2$ is dominantly produced only for the low vibrational molecular ion and at low collision energies. If we assume the n of the fragment atom equal to the principal quantum number of two-electron excited state, Fig. 2 shows the n-distribution of fragment atom.

5.2 Rotational motion

If only the dσ partial wave contributes to the DR, the molecular system has strong anisotropy, which induces rotational transition of molecular ions. Owing to the conservation of the angular momentum $\vec{J} = \vec{N}^+ + \vec{\mathbf{l}}^+$, change of the rotational quantum number ΔN^+ is restricted to $\Delta N^+ = 0, \pm 2, \pm 4$ for $\mathbf{l}^+ = 2$ [7]. The present calculation shows that the magnitude of the rotational transition is the same order as the DR.

The DR is also affected by the rotational motion. Fig. 4 shows the rotational state dependence of the DR rate coefficient for $H_2^+(v=0)$. The DR is largely enhanced by the rotational motion at the energies lower than 0.2 eV. It sensitively depends on the initial rotational state.

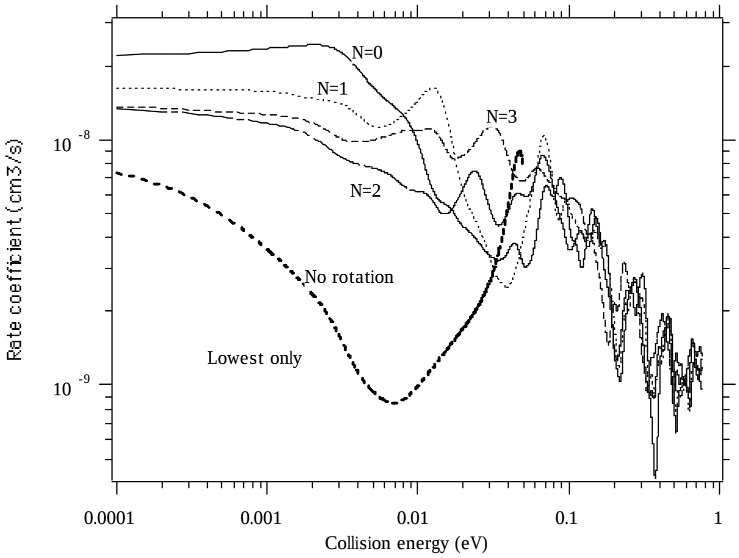

Fig. 4 The rotational motion dependence of the DR rate coefficient for the $H_2^+(v=0) + e$. The initial rotational state is indicated by N. Only the lowest two-electron excited state is included except for the 'No rotation' calculation.

5.3 Vibrational transition

In Fig. 5, we show the cs of vibrational transition. On the initial rotational state, we assume the thermal distribution of 300K. The magnitude of the cs is as large as the DR. It is worthwhile to point out that the transition with a large change of vibrational quantum number is not suppressed although the vibrational transition without electronic resonance is almost restricted within the change of one vibrational quanta, which is known as the propensity rule.

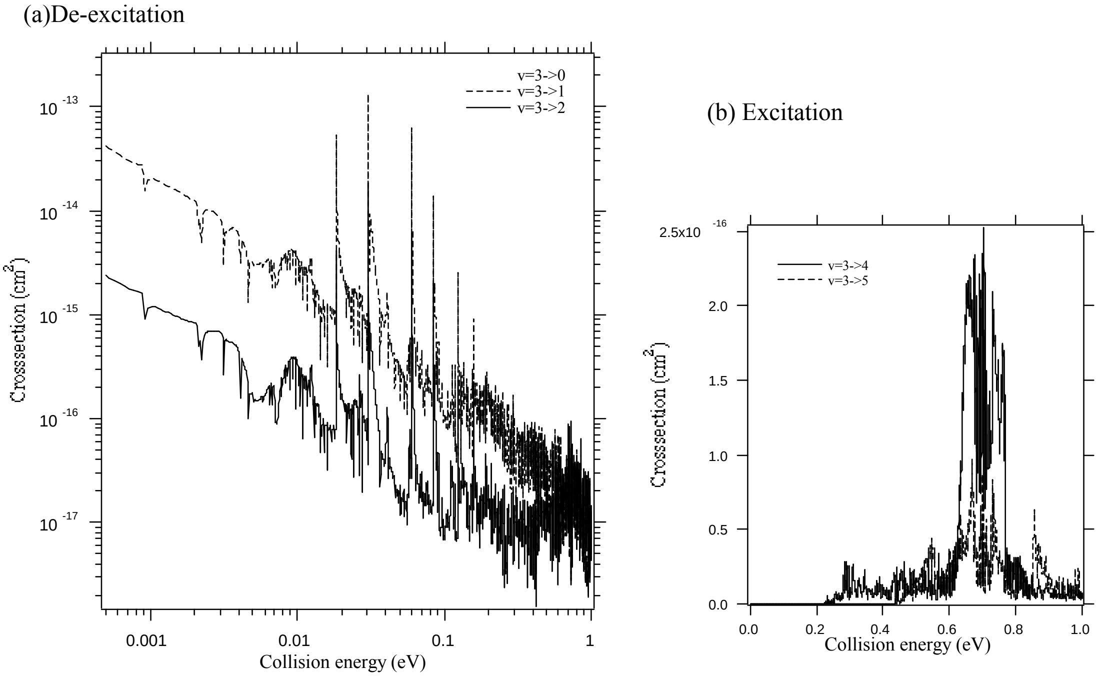

Fig. 5 Vibrational transition of H_2^+

6. REMARKS

By introducing discretized dissociatve functions to the MQDT, we can calculate on the various molecular processes taking into account the higher two-electron excited states, which play an important role. It is, however, difficult to take into account the (1)rotational motion, (2)higher order contribution of the CI dynamics, and (3)non-adiabatic transition together with those highly excited electronic states because we lack the information of those electronic states as the contributing partial waves and their quantum defects, or the off-the-energy-shell information of the CI. The dynamics concerning the highly excited electronic states is a problem in the future.

The state specific molecular data becomes so large that we could not provide them without electronic data file. The data presented here will be provided through the web site of the NIFS data base.

Acknowledgements

The author thanks Dr. Toshizo Shirai (JAERI, the departed) for introducing and helping him to study the atomic and molecular data. He also thanks prof. Tetsumi Tanabe (KEK) for discussing various problems especially on the experiments.

References

[1]Pigarov A. Yu, Phys. Scr. **T96**,16 (2002)
[2] Tanabe, T. et al., Phys. Rev. Lett., **70**, 422 (1993).
Larson, M. et al., Phys. Rev. Lett., **70**, 430 (1993).
[3] Seaton, M J., Proc. Phys. Soc., 88, 815 (1966), Rep. Prog. Phys., **46**, 167 (1983).
[4] Jungen Ch. And Atabek O., J. Chem. Phys., **66**, 5584 (1977)
[5] Bates, D. R., Phys. Rev., **78**, 492 (1950)
[6] Giusti, A., J. Phys. B, **13**, 3867 (1980).
[7] Takagi, H., J. Phys. B, **26**, 4815 (1993).
[8]Pichl, L. and Horacek, J., J. Phys. A, **29**, L405 (1996).
[9] Takagi, H., "Dissociatve Recombination: Theory, Experiment, and Applications IV" (World Scientific 2000), p180.
[10] Pichl, L., Nakamura, H. and Horacek, J., Comp. Phys. Commun., **124**, 1 (2000)
[11] Takagi, H., "Dissociatve Recombination: Theory, Experiment, and Applications III" (World Scientific 1996), p174.
[12]Takagi H., Phys. Scr. T96 42 (2002)
[13]Tennyson, J., At. Data Nucl. Data Tables, **64**, 253 (1996).
[14]Tanabe, T. et al., "Dissociatve Recombination: Theory, Experiment, and Applications IV" (World Scientific 2000), p170.
[15]Zajfman, D. and Amitay Z., "Dissociatve Recombination: Theory, Experiment, and Applications III" (World Scientific 1996), p114.

Calculations of ATI and HHG spectrum of one-dimensional atom in the intense laser field

Xiao-xin Zhou [1) 2)]　Song-feng Zhao [1)]

[1)](College of Physics and Electronic Engineering ,North-West Normal University ,Lanzhou, 730070)
[2)](Center of Theoretical Nuclear Physics,National Laboratory of Heavy Ion Accelerator of Lanzhou, Lanzhou 730000)

Abstract: We investigate ATI and HHG spectrum of one-dimensional atom in intense laser fields by solving time-dependent Shrödinger equation of one-dimensional atom in intense laser fields with linear-least-squares-fitting method and pseudo-spectral method. Our results are very good agreement with those of split-operator method.

Key words: Linear-least-squares-fitting method; pseudo-spectral method; Intense laser field; Above-threshold ionization; High order harmonic generation

1 Introduction

When atoms are exposed to the intense laser field, many interesting multi-photon phenomena such as the above-threshould ionization(ATI) and high-order harmonic generation(HHG) have been observed in experiments[1-3]. In order to describe these phenomena theoretically, perturbation approaches are not useful when the intensity of the laser field exceed 10^{12}~10^{13}W/cm^2. The method used commonly to describe the pheno- mena is the direct numerically solution of time-dependent Shrödinger equation[4-8].

2 Theory and method

We present linear-least-squares-fitting method[9] and pseudo-spectral method[10] to solve the time-dependent Shrödinger equation of a one-dimensional model atoms in an intense laser field by introducing the eigen-functions which are constructed from the linear combination of the B-spline functions and the truncated Fourier series. We calculate above-threshold ionization electron spectrum and high-order harmonic generation of one-dimensional atom in intense laser fields. Our results are in very good agreement with those of split-operator method.

3 Results and discussion

In our calculations, we choose the following laser field profile

$$E(t) = \begin{cases} E_0 \sin^2\left(\dfrac{\pi t}{6T}\right)\sin\omega t & 0 \le t \le 3T \\ E_0 \sin\omega t & t > 3T \end{cases} \tag{1}$$

where E_0 is the amplitude of the laser field.

In Fig.1, we show the normalized harmonic generation spectra for E_0=0.1 a.u., ω=0.148 a.u at t=16T with linear-least-square-fitting method. our results are very good agreement with the calculation using split-operator method (dashed line). In Fig.2, we show the ATI spectrum for E_0=0.05 a.u.,0.07071 a.u., 0.085 a.u. with ω=0.148 a.u fixed at t=4.25T with pseudo-spectral method and split-operator method, our results are very good agreement with those using split-operator method (dotted line).

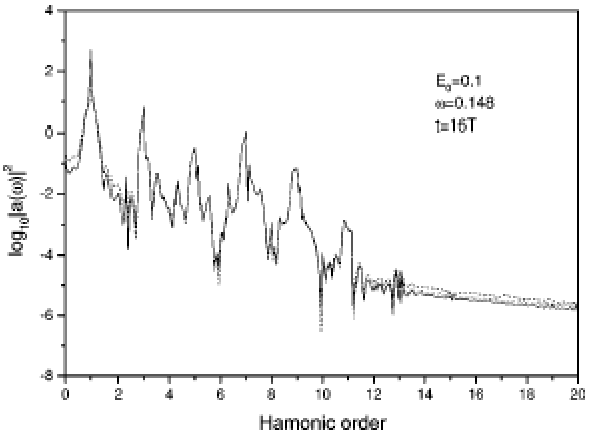

Fig.1. Harmonic generation spectra calculated with pseudo-spectral method (solid line) and split-operator method (dashed line).

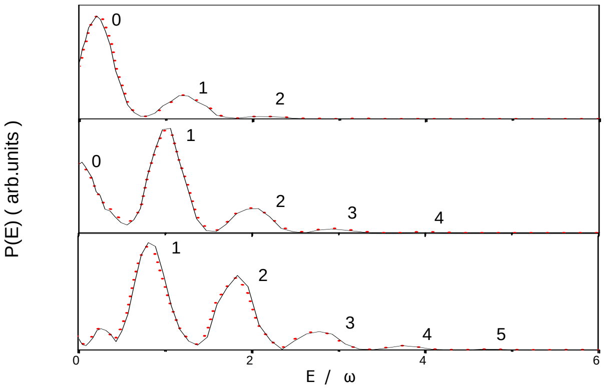

Fig.2 ATI spectrum for E_0=0.05 a.u.,0.07071 a.u.,0.085 a.u.(from top to bottom) with ω =0.148 a.u fixed, for t=4.25T. The solid line is the results by using pseudo-spectral method, the dotted line is the results by using split-operator method.

4 Conclusion

We investigate ATI and HHG spectrum of one-dimensional atom in intense laser fields by solving time-dependent Shrödinger equation of one-dimensional atom in intense laser fields with linear-least-squares-fitting method and pseudo-spectral method. Our results are very good agreement with those of split-operator method.

Acknowledgements

This work is supported by the National Natural Science Foundation of China(Grant No.10274063), by the Foundation of Science and Technology Research of the Ministry of Education of China (Grant No.03126) and by the Foundation of the Northwest Normal University(Grant No.NWNU- KJXGC-214).

References

[1] Atoms in Intense Laser Fields, Adv. At. Mol. Phys, Suppl.1 (1992) , edited by M.Gavrila.

[2] K.Burnett, V.C.Reed, and P.L.Knight, J. Phys. B.,26,561 (1993) .

[3] M.Protopapas, C.H.Keitel and P.L.Knight, Rep. Prog. Phys.60**,** 389 (1997) .

[4] M. R. Hermann and J. A. Fleck, Phys. Rev. A, 38 , 6000 (1988).

[5] J. L. Krause, K. J. Schafter, and K. C. Kulander, Phys. Rev. A, 45 , 4998 (1992).

[6] K. J. LaGattuta, J. Opt. Soc. Am. B7, 639 (1990) .

[7] P. L. Devries, J. Opt. Soc. Am. B7, 517(1990) .

[8] J. H. Eberly, Q. Su and J. Javanainen, Phys. Rev. Lett., 20 , 881 (1989) .

[9] X.X. Zhou, C. D. Lin, Phys. Rev. A. 61**,** 053411 (2000) .

[10] S. F. Zhao , X. X. Zhou, P. C. Li, G. L. Wang, Chinese Journal of Atomic and Molecular Physics, 2004,21 (2): 304

,

MULTIPLE IONIZATION DYNAMICS OF MOLECULES IN INTENSE LASER FIELDS

Atsushi Ichimura*[1] and Tomoko Ohyama-Yamaguchi†[2]

**Institute of Space and Astronautical Science, JAXA,*
Yoshinodai, Sagamihara, Kanagawa 229-8510, Japan

†Tokyo Metropolitan College of Technology,
Higashi-Ohi, Shinagawa, Tokyo 140-0011, Japan

Abstract

A classical field-ionization model is developed for sequential multiple ionization of diatomic and linear triatomic molecules exposed to intense ($\sim 10^{15}$W/cm^2) laser fields. The distance $R_{\rm ion}$ of Coulomb explosion is calculated for a *combination* of fragment charges, by considering nonadiabatic excitation followed by field ionization associated with the inner and outer saddle points. For diatomic molecules (N_2, NO, and I_2), the model explains behaviors observed in experiments, as $R_{\rm ion}(21 \to 31) < R_{\rm ion}(21 \to 22)$ between competing charge-asymmetric and symmetric channels, and even-odd fluctuation along a principal pathway. For a triatomic molecule CO_2, a comparison of the model with an experiment suggests that charge-symmetric (or nearly symmetric) channels are dominantly populated.

1 Introduction

Interwoven electronic and nuclear dynamics emerges in a molecule when exposed to an intense ($\sim 10^{15}$W/cm^2) laser field [1, 2]. Since its peak field strength is comparable to an internal field in an atom, a small molecule will be multiply ionized and subsequently dissociated into atomic fragment ions (Coulomb explosion). This process has been extensively and intensively investigated with the recent technique of ion-momentum imaging for a variety of diatomic (NO, I_2, N_2, ...) [3—6] and linear triatomic (CO_2, CS_2, OCS, ...) [7—9] molecules.

Of particular interest thereby is a phenomena called *enhanced ionization*, *i.e.*, remarkable enhancement of ionization rate in comparison with that for an isolated constituent atom. This phenomena has been basically explained for a homonuclear diatomic molecule with a classical field-ionization model developed by Posthumus *et al* [10]. They take account of the effect of bond stretching as a result of initial excitation and ionization. As the bond length R is elongated during the laser pulse duration ($\sim 10^{-13}$ s), the outermost electron remaining will get localized into atomic sites to be Stark shifted. Accordingly, the appearance field strength $F_{\rm ap}(R)$ of multiple ionization is lowered until reaching a minimum at a *critical distance* $R_{\rm cr}$, which turns out a few times as large as the equilibrium distance, weakly depending on ionization stages. These behaviors are supported by experimental observations [3 — 7] and also by quantum mechanical calculations carried out for one- and two-electron systems [11 — 13].

---

[1] e-mail: ichimura@pub.isas.ac.jp

[2] e-mail: yamaguti@tokyo-tmct.ac.jp

In the formulation by Posthumus *et al.* [10], the active electron is assumed to move around in a diatomic molecular ion $\mathrm{AB}^{(q-1)+}$ with a double-well potential determined by ion core charges $(q_\mathrm{A}, q_\mathrm{B}) = (q/2, q/2)$. Consequently, the model describes *charge-symmetric* evolution with total charge $q = q_\mathrm{A} + q_\mathrm{B}$, actually applicable to a principal pathway as $(q_\mathrm{A}, q_\mathrm{B}) = (1,0) \to (1,1) \to (2,1) \to \cdots$. The recent experiments [4—6], however, demonstrate the behaviors associated with the freedom of *charge-asymmetry* $\mathit{\Delta} = |q_\mathrm{A} - q_\mathrm{B}|$. In common to the results for NO [4], I_2 [5], and N_2 [6], asymmetric products ($\mathit{\Delta} = 2$) have been observed along with competing symmetric products ($\mathit{\Delta}$ =0). The distance R_ion at which multiple ionization occurs is measured to be definitely shorter for $\mathit{\Delta} = 2$ than for $\mathit{\Delta}$ =0, such as $R_\mathrm{ion}(3,1) < R_\mathrm{ion}(2,2)$ [4—6]. This fact would be a puzzle in a framework of the model [10] because the third outermost electron in one atom is ionized earlier than the second in another atom (*i.e.*, the fifth in the molecule earlier than the fourth). Moreover, the distance R_ion exhibits slight but systematic even-odd fluctuation with q superposed on a mean trend along the principal pathway, more elongated for even-q ($\mathit{\Delta}$ =0) than for odd-q ($\mathit{\Delta}$ =1). Automatic application of the model would predict an inverse fluctuation through the even-odd fluctuation in the binding energy of q-th molecular electron. These observations need to be clarified.

In the present report, we reformulate the classical field ionization model for a diatomic molecule so as to derive the distance $R_\mathrm{ion}(q_\mathrm{A}, q_\mathrm{B})$ of Coulomb explosion for a *pair* of fragment charges $(q_\mathrm{A}, q_\mathrm{B})$; the freedom of charge-asymmetry $\mathit{\Delta}$ is incorporated as well as total charge q, while the mechanism responsible for enhanced ionization is retained. This treatment is shown to explain the even-odd fluctuation and the relation as $R_\mathrm{ion}(3,1) < R_\mathrm{ion}(2,2)$. Furthermore, we extend the model to a linear triatomic molecule ABC along the same lines for deriving the distance $R_\mathrm{ion}(q_\mathrm{A}, q_\mathrm{B}, q_\mathrm{C})$ for a *combination* of three fragment charges. Comparison of the model with an experimental result for CO_2 [9] suggests that charge-symmetric (or nearly symmetric) channels are dominantly populated.

2 Reformulation and extension of the model

We address the multi-electron dissociative ionization of diatomic and linear triatomic molecules in an intense laser field applied along the molecular axis $\hat{\boldsymbol{R}}$. The molecule is assumed to be sequentially ionized; a single active electron is removed in respective steps. In general, electronic motion (velocity ~ 1 au) in a molecule is much faster than dissociating nuclei ($\sim 10^{-2}$ au), and also than the field oscillation (angular frequency $\sim 10^{-2}$ au). Hence, the many-electron dynamics is treated as a sequence of the over-the-barrier electron-releasing processes, each described by an appearance laser intensity for a fixed bond distance. Such a treatment is justified when the Keldysh parameter is small enough that the ionization probability is almost unity within half a laser cycle [2].

In the previous treatment by Posthumus *et al* [10] for a diatomic molecule AB, the active electron is uniquely taken in respective ionization steps to be the outermost (least binding) electron in a *molecular* ion $\mathrm{AB}^{(q-1)+}$. By contrast, we consider two possible pathways for the production of a pair of ions $(q_\mathrm{A}, q_\mathrm{B})$, as $(q_\mathrm{A} - 1, q_\mathrm{B}) \to (q_\mathrm{A}, q_\mathrm{B})$ and $(q_\mathrm{A}, q_\mathrm{B} - 1) \to (q_\mathrm{A}, q_\mathrm{B})$; the active electron is taken to be either an outermost electron in an *atomic* ion $\mathrm{A}^{(q_\mathrm{A}-1)+}$ or that in $\mathrm{B}^{(q_\mathrm{B}-1)+}$.

Hence, the single electron dynamics is described for both pathways with a two-center

Coulomb potential generated by core charges $(q_{\rm A}, q_{\rm B})$ plus the field F applied, as

$$U(\boldsymbol{r}; R, F) = -\frac{q_{\rm A}}{|\boldsymbol{r} + \boldsymbol{R}/2|} - \frac{q_{\rm B}}{|\boldsymbol{r} - \boldsymbol{R}/2|} - F\hat{\boldsymbol{R}} \cdot \boldsymbol{r}. \tag{1}$$

This potential has two saddle points, $U_{\rm in}(R, F)$ inside the molecule, and $U_{\rm out}(R, F)$ outside either beyond B or beyond A according to the sign of the field F. The energy level is given, when the electron is localized in site A, as

$$E_{\rm A}(R, F) \;=\; -I_{\rm A} - \frac{q_{\rm B}}{R} + \frac{FR}{2}, \tag{2}$$

with the $q_{\rm A}$-th ionization potential $I_{\rm A}$ of an isolated atom A. Hence, a phase diagram is constructed in the R-F plane, as shown in Fig.1, with boundaries as

$$E_{\rm A}(R, F) \;=\; U_{\rm in}(R, F), \tag{3}$$

$$U_{\rm out}(R, F) \;=\; U_{\rm in}(R, F). \tag{4}$$

As shown in the figure, the solution of Eq.(4) has two branches, $F^{(+)}(R)$ (> 0) and $F^{(-)}(R)$ (< 0), both proportional to R^{-2} because of a character of the Coulomb potential. Eq.(3) has a single branch $F_{\rm A}(R)$, which negatively diverges more rapidly than $F^{(-)}(R)$ in the limit of $R \to 0$, and converges to the atomic appearance field $I_{\rm A}^2/(4q_{\rm A})$ in $R \to \infty$. In between, the curve $F_{\rm A}(R)$ crosses the axis of $F = 0$ at a distance $R_0 = (q_{\rm A} + 2\sqrt{q_{\rm A}q_{\rm B}})/I_{\rm A}$, which turns out to be a few times longer than the equilibrium length $R_{\rm eq}$ in a covalent molecule. The phase diagram for ionization from site B is constructed in the same way as that from site A, but taking the equation of $E_{\rm B}(R, F) = U_{\rm in}(R, F)$ with the energy of

$$E_{\rm B}(R, F) \;=\; -I_{\rm B} - \frac{q_{\rm A}}{R} - \frac{FR}{2}, \tag{5}$$

in stead of Eq.(3) with Eq.(2).

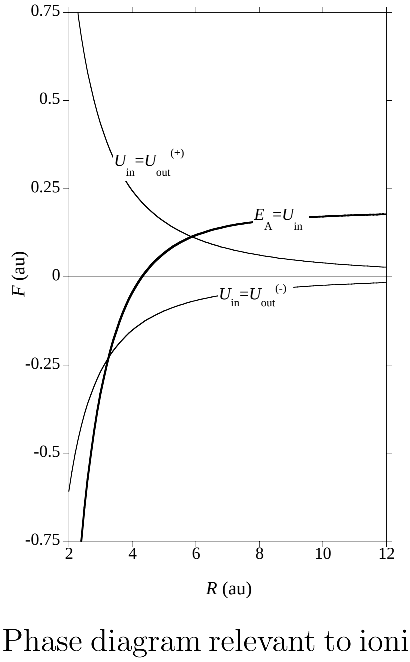

Fig.1. Phase diagram relevant to ionization $(2, 1) \to (3, 1)$ with $I_{\rm A} = 0.5 \times q_{\rm A}$ au.

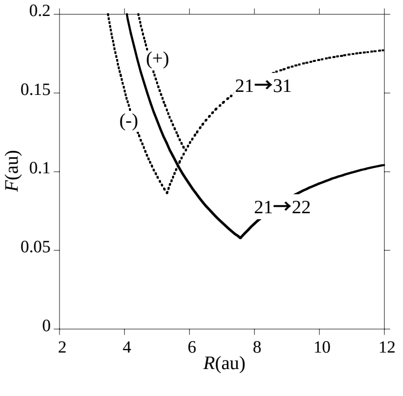

Fig.2. Appearance field curves for $(2, 1) \to (3, 1)$ and $(2, 1) \to (2, 2)$.

We suppose that the bond distance is stretched near to R_0 during the laser pulse duration. For a given laser strength F_0 (> 0), the field F is oscillated over a range of $-F_0 \leq F \leq +F_0$, which will cover the localized ($F < F_{\mathrm{A}}(R)$) and delocalized ($F > F_{\mathrm{A}}(R)$) domains. Hence the field oscillation is expected to induce nonadiabatic excitation to an energy around the inner saddle, and subsequently causes field ionization over the outer saddle if $U_{\mathrm{in}}(F, R) \geq U_{\mathrm{out}}(F, R)$ is satisfied either at $F = +F_0$ or at $F = -F_0$. This mechanism derives the appearance strength curve $F_{\mathrm{ap}}(R)$ (> 0) as shown in Fig.2. It is seen that the negative phase ($F = -F_0$) is favored when $q_{\mathrm{A}} > q_{\mathrm{B}}$, and that the charge asymmetric ($\Delta = 2$) channel has smaller appearance strength than the competing symmetric ($\Delta = 0$) channel. We note that this ionization mechanism requires a two-step process in two half cycles of field oscillation, as illustrated in Fig.3.

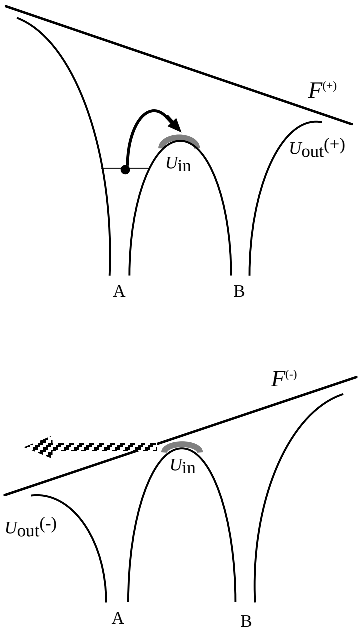

Fig.3. Optimum two-step ionization mechanism in a diatomic molecule AB from site A.

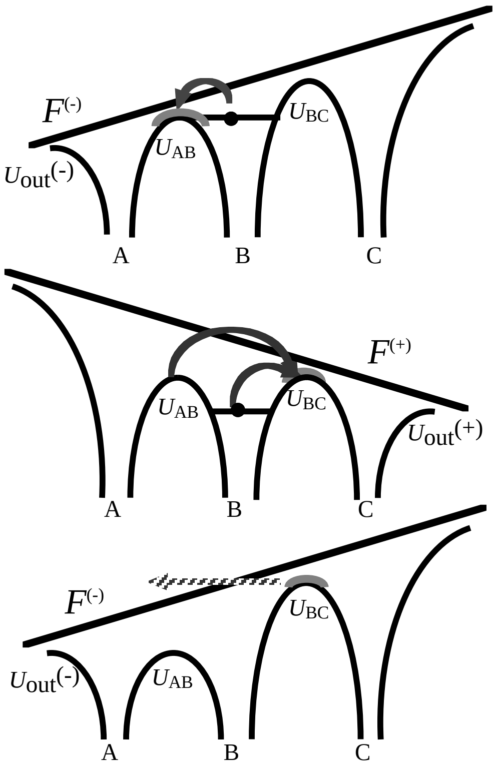

Fig.4. Optimum three-step ionization mechanism in a linear triatomic molecule ABC from site B.

The model is extended to a linear triatomic molecule ABC by assuming symmetric stretching (equal bond length). The active electron is taken to be an outermost electron at one of the three atomic sites and described with a three-center Coulomb potential. The field oscillation induces nonadiabatic excitation followed by field ionizaition in a similar way to that for a diatomic molecule, but in more complicated manner associated with two inner and one outer saddle points in the potential. The appearance field curve is determined through comparison among many different curves corresponding to possible mechanisms. The optimum ionization mechanism from the central site B requires three half cycles of field oscillation, as illustrated in Fig.4.

3 Results and Discussion

The appearance field curves $F_{\text{ap}}(R)$ is given in the model as proportional to R^{-2} for diatomic and linear triatomic molecules. From $F_{\text{ap}}(R)$ obtained, the distance R_{ion} of Coulomb explosion is calculated at a given laser intensity.

In a diatomic molecule, the distances obtained for different fragment pairs are plotted and compared with experimental result [4] for NO molecule in Fig. 5. As indicated in Fig.5, the model explains the experimental observations of even-odd fluctuation with q along a symmetric pathway ($\mathit{\Delta} \leq 1$) and of a relation as $R_{\text{ion}}(3,1) < R_{\text{ion}}(2,2)$ between competing symmetric ($\mathit{\Delta} = 0$) and asymmetric ($\mathit{\Delta} = 2$) pathways. These behaviors are related to a general rule derived from the model that, the larger the charge asymmetry $\mathit{\Delta}$, the smaller the distance R_{ion}, for a given total charge q.

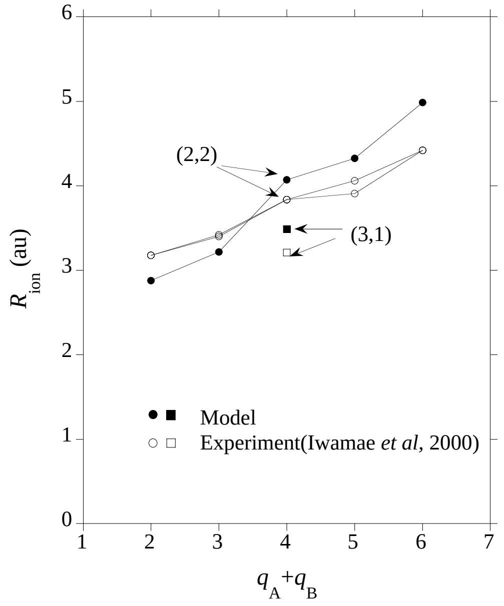

Fig.5. Comparison of the present model with an experiment [4] for the distances of ionization of NO molecule at a laser intensity of 1.4 PW/cm^2.

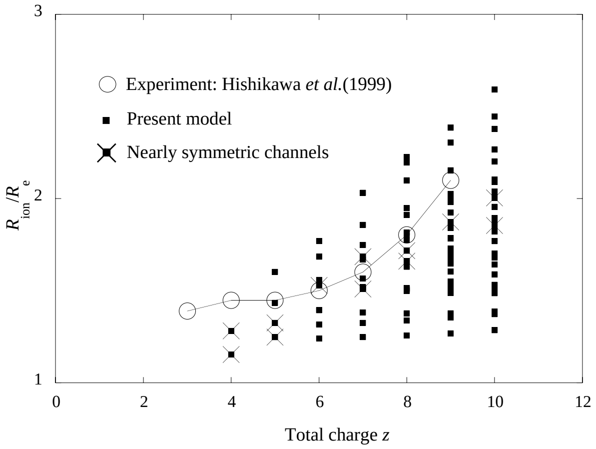

Fig.6. Comparison of the present model with an experiment [7] for the distances of ionization of CO_2 molecule at a laser intensity of 1.4 PW/cm^2.

In a linear triatomic molecule, the effect of enhanced ionization manifests itself more prominently than in a diatomic molecule through more complicated mechanisms involving more saddle points. Comparison of $F_{\text{ap}}(R)$ among ionization pathways permits us to predict which fragmentation channel is produced at a smallest bond length from a common initial channel. A propensity rule is found that the central site B is ionized earliest from left-right asymmetric ($q_A \neq q_C$) channels, while the terminal sites A and C are earliest from symmetric ($q_A = q_C$) channels.

Distances R_{ion} obtained for different channels are plotted and compared with an experiment [7] for CO_2 molecule in Fig.6. It is seen from the comparison in the figure that, although fragmentation channels are not clearly resolved in the experiment, its result is consistent with dominant population in charge symmetric or nearly symmetric channels ($\mathit{\Delta} \leq 1$ for any pair among the three fragment charges). It is also noted in the figure that the distance increases linearly with the total charge in the model, while nonlinearly in the experiment. This observation may be due to a defect of the model ignoring the bending freedoms of nuclear motion.

References

[1] K. Yamanouchi, Science **295** 1659 (2002).
[2] J.H. Posthumus and J.M. McCann, in *Molecules and Clusters in Intense Laser Fields*, ed. J.H. Posthumus (Cambridge Univ. Press, Cambridge, 2001).
[3] J.H. Posthumus, L.J. Frasinski, A.J. Gilles, K. Codling, *J. Phys. B: At. Mol. Opt. Phys.* **28** L349 (1995).
[4] A. Iwamae, A. Hishikawa, and K. Yamanouchi, *J. Phys. B: At. Mol. Opt. Phys.* **33** 223 (2000).
[5] G.N. Gibson, M.Li, G.Guo, and J.P. Nibarger, *Phys. Rev. A* **58** 4723 (1998).
[6] J.P. Nibarger, S.V. Menon, and G.N. Gibson, *Phys. Rev. A* **63** 053406 (2001).
[7] A. Hishikawa, A. Iwamae, and K. Yamanouchi, *Phys. Rev. Lett.* **83** 1127 (1999).
[8] A. Hishikawa, H. Hasegawa and K. Yamanouchi, *Chem.Phys.Lett.* **388** 1 (2004).
[9] J.H.Sanderson, T.R.J.Goodworth, A.El-Zein, W.A.Bryan, W.R.Newell, A.J.Langley, and P.F.Taday, *Phys.Rev.* A**65** 043403 (2002).
[10] J.H. Posthumus, L.J. Frasinski, A.J. Gilles, and K. Codling, *J. Phys. B: At. Mol. Opt. Phys.* **29** L525 (1996); J.H. Posthumus, A.J. Gilles, M.R. Thompson, and K. Codling, *J. Phys. B: At. Mol. Opt. Phys.* **29** 5811 (1996).
[11] T. Seideman, M. Ivanov, and P. Corkum, *Phys. Rev. Lett.* **75** 2819 (1995); M. Ivanov, T. Seideman, P. Corkum, F. Ilkov, and P. Dietrich, *Phys. Rev* A**54** 1541 (1996).
[12] S. Chelkowski and A.D. Bandrauk, *J. Phys. B: At. Mol. Opt. Phys.* **28** L723 (1995); T. Zuo and A.D. Bandrauk, *Phys. Rev.* A**52** R2511 (1995); H. Yu and A.D. Bandrauk, *Phys. Rev.* A**56** 685 (1997).
[13] I. Kawata, H. Kono, and A.D. Bandrauk, *Phys. Rev.* A**64** 043411 (2001); K. Harumiya, H. Kono, and Y. Fujimura, *Phys.Rev.* A**66** 043403 (2002).

GEOMETRY EFFECTS ON THE (e,2e) CROSS SECTION OF IONIC TARGETS

Y. Khajuria
Institute for Molecular Science, Okazaki 444-8585, Japan

ABSTRACT

The three body distorted wave Born approximation (DWBA) with spin averaged static exchange potential has been used to calculate the electron impact triple-differential cross section of Li^+, Na^+ and K^+ ions in different geometries and kinematics. In coplanar geometry at high incident energy (≥ 500 eV) and scattering angle ~10º, both recoil and binary peaks in case of p-orbital electrons splits into two. The value of the binary to the recoil peak ratio for the specific value of the momentum transfer has been determined to understand the collision dynamics. In the non-coplanar geometry a strong interference resulting in a dip in triple differential cross section (TDCS) has been noticed.

Keywords: (e,2e), TDCS, DWBA

Email: khajuria@ims.ac.jp

1. Introduction:

It is well known that collisions of electron projectile with ionic targets play key roles in a variety of fields such as plasma, astrophysics and controlled nuclear fission. The (e,2e) technique is a powerful means to seek detailed information on the collision dynamics. However, the technique can not be readily applied to ionic targets because of the experimental difficulty in producing the sufficient target density. Furthermore, the theoretical attempts also have been scarce as yet for the ionic targets.

The difficulty that arises in studying the electron impact ionization of ionic targets, as compared to neutral one, is the presence of long range coulomb interaction. Roy et al [1] have made calculation for He^+ ion neglecting electron-electron correlation in the final channel. Thus their final state wavefunction does not satisfy the proper three body boundary condition. Biswas and Sinha [2] suggested a model in which the scattered electron is treated in the framework of the eikonal approximation, while the ejected electron is represented by a coulomb wave. The correlation between the two electrons is taken into account through the eikonal phase term and coulomb parameters. Xingfu et al [3] extended the Brauner-Briggs-Klar (BBK) model [4] for hydrogen and helium ions, in which the incident electron is described by coulomb wave and the final channel is represented by the BBK wavefunctions. Their results are in good agreement with the theoretical calculations of Biswas and Sinha [5]. Rasch [6] studied the (e,2e) process for the hydrogenic ion targets using the distorted wave Born approximation (DWBA) in order to see whether the recoil peak is enhanced with the increase in nuclear charge as in neutral atoms. The triple differential cross section (TDCS) caused by the electron impact ionization largely depends on both geometry as well as kinematics, and therefore, a proper understanding of their roles is essential for explaining the collision dynamics. All the above mentioned studies are limited only to the coplanar asymmetric geometry and hence, the complete knowledge about the collision process can not be obtained from these studies.

The present work therefore aims at understanding of the different geometries effects for the process of electron impact ionization of alkali ions by using DWBA method. The TDCS has been determined with different geometries and at different sets of kinematical variables. In the coplanar asymmetric geometry a splitting of binary and recoil peak in case of p-orbital electrons is seen at higher incident energy with in the specified range of ejected electron angles. A strong interference dip in the TDCS cross section in non-coplanar geometry has been noticed for each orbital. The present work not only exhibits various geometry effects but also demonstrates that DWBA is a reliable method to describe the electron impact ionization of ions.

2. Theory:

The TDCS is a measure of the probability that an (e,2e) reaction at an incident electron energy of E_0 and momentum $\boldsymbol{k}_0$, upon collision with the target produces two electrons (ejected and scattered) with energies E_1 and E_2 having momentum $\boldsymbol{k}_1$ and $\boldsymbol{k}_2$ satisfying the relation,

$$E_{incident}=E_1+E_2+\varepsilon\,,$$

where ε is the ionization potential of the target.

It is essential to distinguish between several kinematical arrangements here. In the coplanar asymmetric geometry the momentum $\boldsymbol{k}_0$, $\boldsymbol{k}_1$ and $\boldsymbol{k}_2$ are in same plane; θ_1 (scattered electron angle) is kept normally small, and θ_2 (ejected electron angle) is varied. In coplanar symmetric geometry again $\boldsymbol{k}_0$, $\boldsymbol{k}_1$ and $\boldsymbol{k}_2$ are in same plane, but $\theta_1=\theta_2=\theta$ is varied. Another important distinction is made between asymmetric and symmetric geometries: in asymmetric geometry both the outgoing electrons are kept at different energies ($E_1 >> E_2$), while in symmetric geometry the two outgoing electrons are kept at same energy.

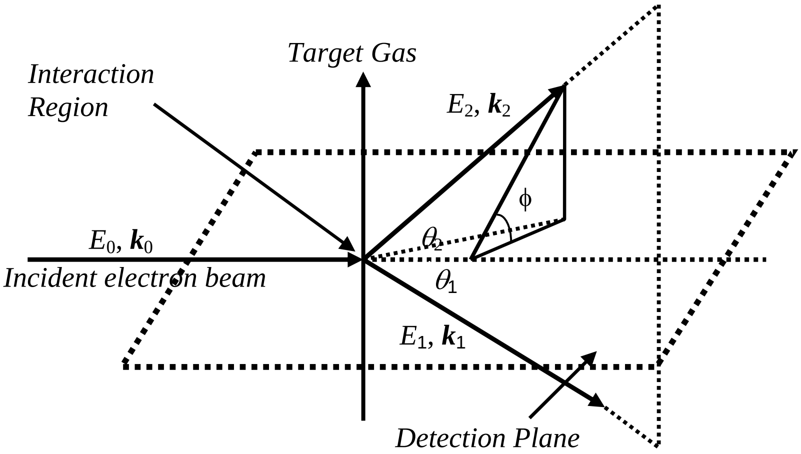

Fig. 1: Diagrammatically representation of (e,2e) process.

The TDCS for the ionization can be written as

$$\frac{d^3\sigma}{d\Omega_1 d\Omega_2 dE_1} = (2\pi)^4 \frac{\boldsymbol{k}_1\boldsymbol{k}_2}{\boldsymbol{k}_0}\left\langle \chi^{(-)}(\boldsymbol{k}_1)\chi^{(-)}(\boldsymbol{k}_2)\middle|V\middle|\chi^{(+)}(\boldsymbol{k}_0)\psi_{nl}\right\rangle$$

V is the electron-electron potential. $\chi^{(\pm)}$ are the distorted wave for the incident and outgoing electrons and have been generated in the static exchange potential of initial state ion and final state ion respectively. ψ_{nl} is the orbital wave function under consideration.

3. **Results and discussions**:

The TDCS calculations for the ionization of all the targets here are made with various kinematical parameters has been carried out. The representative results are given here.

A. **Coplanar asymmetric geometry**:

Figure 2 shows the DWBA results for the (e,2e) TDCS of Li^+ at 250, and 1000 eV for θ_1=10° and E_2=10eV. The recoil and binary peaks lie opposite to each other i.e. they are separated by 180° being in the direction of momentum transfer. From figure it can be seen that the recoil peak becomes broaden and shifts towards the higher scattering angles with increase in the incident energy and. The binary to the recoil peak ratio is always larger than unity and increases with the increase in incident energy (for details see table 1).

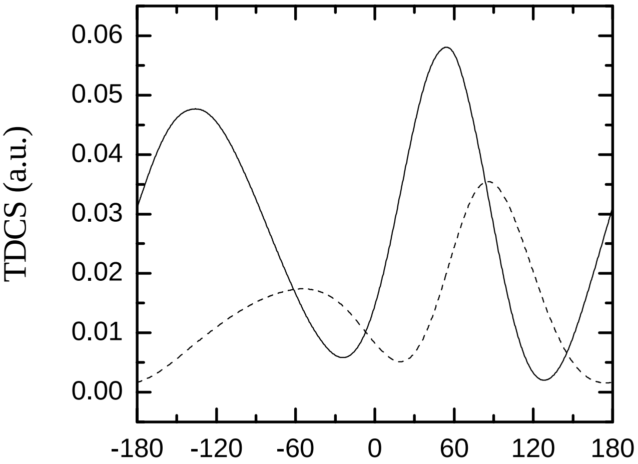

Fig. 2 TDCS for the ionization of Li^+ at impact energy of 200 eV (solid line) and 1000 eV (dotted line) for θ_1=10° and E_2=10eV

Figure 3 shows the TDCS for the ionization of the p-orbital of Na^+ ion at 250, 500 and 1000 eV for θ_1=10° and E_2=10eV. The TDCS for 500 (dashed line) and 1000 eV (dotted line) have been multiplied by factor of 2 and 5 respectively for ease of shape comparison. There is a bump in the cross section for the binary peak at 250 eV, which splits at 500 eV and becomes more pronounced at 1000 eV. The recoil peak also splits at higher impact energy. Similar behavior of the cross section has been observed for K^+ ion.

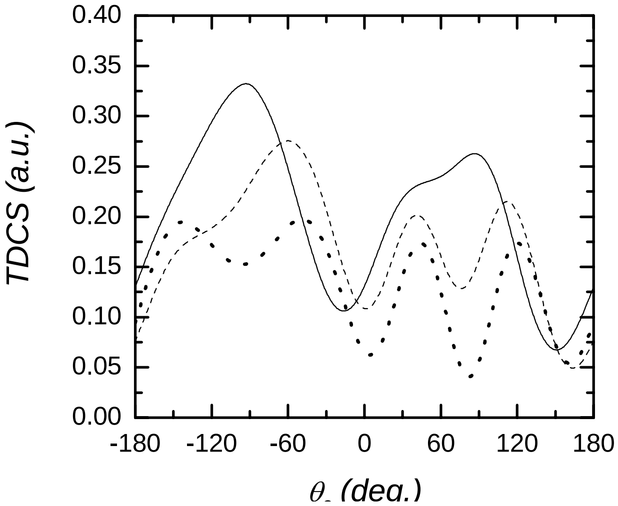

Fig. 3 TDCS for the ionization of Na^+ at impact energy of 200 eV (solid line, 500 eV (dashed line) and 1000 eV (dotted line) for θ_1=10° and E_2=10eV

Parameters			Li$^+$		Na$^+$		K$^+$	
E_0	E_2	θ_1	$\boldsymbol{q}$	*b/r*	$\boldsymbol{q}$	*b/r*	$\boldsymbol{q}$	*b/r*
250	5	4	0.80	0.69	0.55	0.65	0.43	0.76
250	10	4	0.85	0.83	0.59	0.81	0.47	0.77
250	10	10	1.05	1.18	0.87	0.88	0.80	0.78
50 0	5	4	0.65	0.99	0.52	0.71	0.47	0.77
500	10	4	0.67	1.18	0.54	0.88	0.48	0.98
500	10	10	1.14	1.76	1.08	B	1.06	B
1000	5	4	0.68	1.13	0.63	0.68	0.61	0.84
1000	10	4	0.69	1.35	0.64	0.90	0.62	1.07
1000	10	10	1.51	2.05	1.49	B	1.48	B

*Table1. Binary to the recoil (b/r) peak ratio intensity, momentum transfer (**q**) in a.u. The energies E_0 and E_2 in a.u. and θ_1 are in degrees. B indicates the case, where peak is splitted*

The splitting of binary peak for the p-orbital targets can be understood in terms of the Bethe-ridge condition, which is satisfied in the two electron collision when the momentum transferred to the fast electron is equal to the slow electron. It has been seen that when the difference between the momentum transferred and the momentum of the slow electron is small, only binary peak splits and when difference becomes large the recoil peak also splits. The full explanation for this along with the kinematical details is given in Ref. [7] in case of Ar(3p) system, to a large extent are also found to hold in case of ionic targets. A detailed discussion in the present case is therefore not warranted.

The complete information about the ionic targets presented here can be seen from the table 1, where the binary to recoil peak ratio (b/r) and momentum transfer ($\boldsymbol{q}$) corresponding to different kinematical parameters is given.

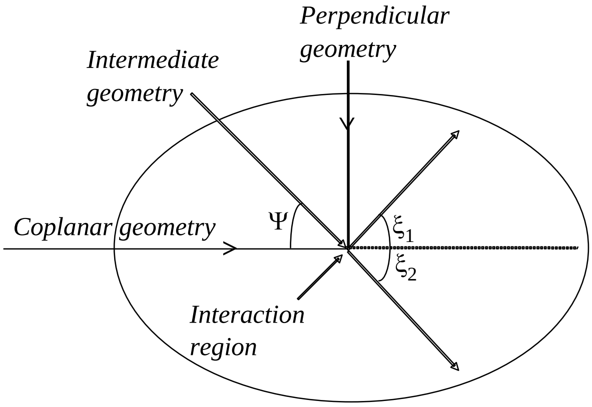

Fig 4. Sketch of *Coplanar to perpendicular plane geometry:*

B. Coplanar to intermediate geometry:

In this geometry (shown in fig. 4) the incident electron angle (Ψ) has been changed from 0° (Coplanar geometry) to 67.5° (intermediate geometry) and the scattering angles $\xi_1=\xi_2=\xi$ is varied.

The scattering angles ξ and incident electron angle Ψ (figure 4) are related to scattering angle θ and azimuthal angle ϕ defined in figure 1 are related by the following equations.

$$\tan\phi = \cot\xi \, \sin\Psi ,$$

$$\cos\theta = \cos\xi \, \sin\Psi .$$

The DWBA calculations have been carried at 40 eV above the ionization potential of all the targets, with symmetric and asymmetric detection energies of the out going electrons. For example in case of Li$^+$, the incident electron energy is set to 115.6 eV and the threes sets of out going electrons energies symmetric [(20 and 20) eV], asymmetric [(15 and 25) eV] and highly asymmetric [(5 and 35) eV]. The trend of cross sections for all the ionic targets and for all the sets of detection energy is almost same. Hence, only the results for the Li$^+$ ion will be presented here.

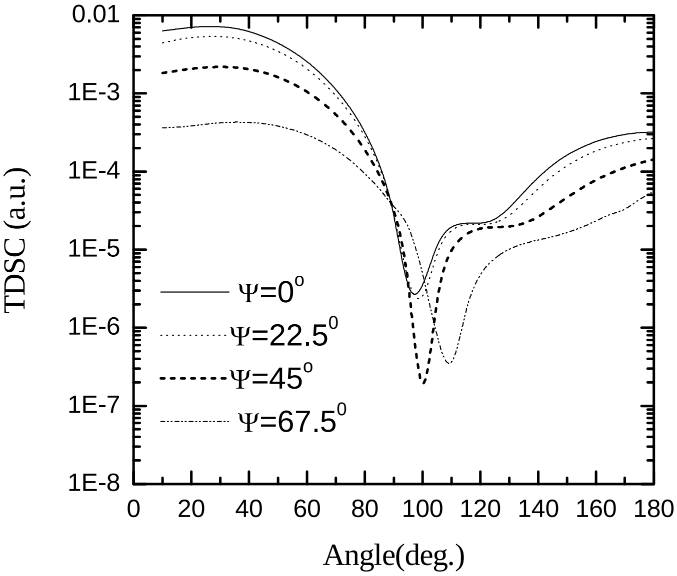

Fig. 5 TDCS for Li$^+$ at 155.6 eV for different incident electron angles (Ψ) indicated

Fig.5 shows the TDCS for the electron impact ionization of Li$^+$ at 115.6 eV incident energy and symmetric energies of the outgoing electrons. There exists a deep minimum in the cross section as reported in the studies of e-He system [8, 9] in which the deep dip always lies at the incident electron angle (Ψ) of 67.5°. However, here it lies at Ψ =45° (dashed line in

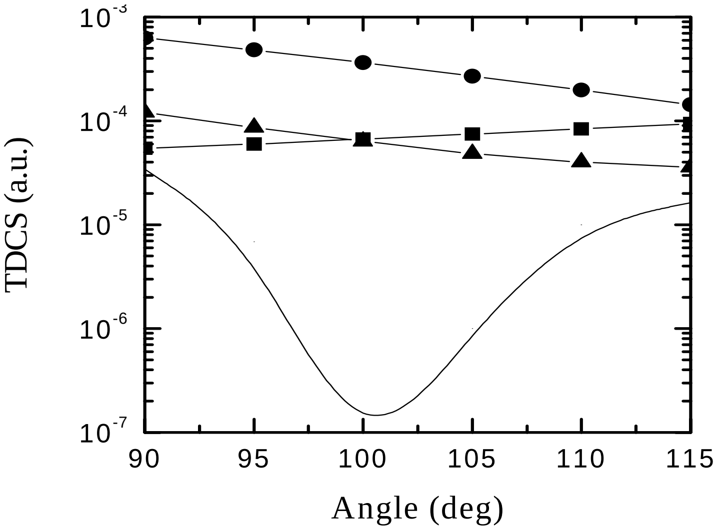

Fig. 6 TDCS for Li$^+$ in the region where the deep minimum has been observed. For details see the text.

figure 5) for symmetric case, at Ψ =45° and Ψ =22.5° for asymmetric and highly asymmetric cases respectively (figures for asymmetric and highly asymmetric case are not presented, for detail see [10]). The reason for the occurrence of the dip in the cross section has been ascertained to the strong interference between the different scattering amplitudes. In order to elucidate this point, TDCS's are calculated, when from the total distorting potential (i) incident electron-nucleus interaction (—▲—) (ii) incident electron-passive electron interaction (—■—) (iii) and both of these (—●—) being stitched off one at a time; this is shown in figure 6. The TDCS with the sum of the above three i.e. with full interaction potential (solid line) is also shown in the angular region of deep minimum. It is seen that the individual cross sections curves are smooth; meaning that switching off any of the potential in either the initial or final channels causes the dip to disappear. This clearly indicates that the deep minimum in the cross section arises due to the strong interference between the different scattering amplitudes constituting the total distorting potential. The same is true for the minimum observed with the other ionic targets.

Conclusion:

The DWBA with suitable interaction potential has been presented for the (e,2e) process with carious kinematical conditions. In the coplanar asymmetric geometry the splitting of the binary and recoil peak in case of p-electron targets has been explained, as usual, in terms of Bethe-ridge condition. In the coplanar to intermediate geometry a clear interference dip in the cross section has been noticed for each target. The present work highlights the geometry effects on the (e,2e) triple differential cross section of ionic targets.

Acknowledgement:

The author is grateful to the organizing committee for giving the chance to present this work at the China/Japan Joint Symposium on Atomic and Molecular Processes in Plasma (Lanzhou, 6th March-11th March 2004.) The help provided by Prof. M. Takahashi and Dr. N. Watanabe (IMS) in presenting this work is highly acknowledged.

References:

[1]. Roy, K. Roy, and N. C. Sil, J. Phys. B. **15**, 1289 (1982).

[2]. R. Biswas and C. Sinha, J. Phys. B. **28**, 1311 (1995).

[3]. J. Xingfu, S. Qicun, C. Zhang Jin, C. Ji, and X. Kezun, Phys. Rev. A **55**, 1971 (1997).

[4]. M. Brauner, J. S. Briggs, and H. Klar, J. Phys. B. **22**, 2265 (1989).

[5]. R. Biswas and C. Sinha, Phys. Rev. A **50**, 354 (1994).

[6]. J. Rasch, Ph.D. thesis, University of Cambridge, 1996.

[7]. H. Ehrhardt, K. H. Hesselbacher, K. Jung, E. Schubert, and K. Willmann, J. Phys. B. **7**, 69 (1974).

[8]. Y. Khajuria and D. N. Tripathi, J. Phys. B. **31**, 2359 (1998) and Phys. Lett. A **260** 360 (1999).

[9]. A. J. Murray and F. H. Read, J. Phys. B. **26**, L369 (1993).

[10]. Y. Khajuria, L. Q. Chen, X. J. Chen, and K. Z. Xu, J. Phys. B. **35**, 93 (2002).

THE MOMENTUM TRANSFER DEPENDENCE OF DOUBLE EXCITATIONS OF HELIUM

Lin-Fan Zhu, Xiao-Jing Liu, Zhen-Sheng Yuan, and Ke-Zun Xu

Hefei National Laboratory for Physical Sciences at Microscale, Laboratory of Bond-Selective Chemistry, Department of Modern Physics, University of Science and Technology of China, Hefei, Anhui, 230026, China

ABSTRACT

The momentum transfer dependence of fundamental double excitation processes of helium is studied with high resolution and fast electron impact. It elucidates the dynamical correlations, in terms of internal correlation quantum numbers, K, T and A. The Fano profile parameters q, f_a, ρ^2, f and S of doubly excited states $_2(1,0)_2^{+}\,{}^1S^e$, $_2(0,1)_2^{+}\,{}^1P^o$ and $_2(1,0)_2^{+}\,{}^1D^e$ are determined as functions of momentum transfer K^2.

1 INTRODUCTION

Electron correlation effect is the fundamental physics for the interaction among electrons in an atom. It has raised the general and continuous interest of both theoreticians and experimentalists in the realm of atomic and molecular physics since the pioneer experimental work of Madden and Codling [1] and the corresponding theoretical investigation of Cooper et al [2,3] on the doubly excited states of helium, which has been reviewed by Tanner et al [4]. Helium is the simplest system to study electron correlation effect because of the two-electron nature.

The doubly excited states lie above the first ionization threshold. But till 1963, the two Rydberg series of double excitations of helium, i.e., $(sp,2n+)\,{}^1P^o$ and $(sp,2n-)\,{}^1P^o$, had been revealed by the photoabsorption experiment of Madden and Codling who used the NBS 180 MeV electron synchrotron [1]. Although it was an undoubtedly excellent advance in atomic physics, the sequent problem arose: according to the theoretical work[5-7], there should be three series excited from the ground state ${}^1S^e$ to final states ${}^1P^o$ below N=2 threshold of He$^+$, i.e., $(sp,2n+)$, $(sp,2n-)$ and pd namely. So the pd series was missing in Madden and Codling's investigation [1]. There after, lots of experimental studies were carried out on the double excitations of helium until the first observation of the missing Rydberg series by Domke *et al* [8]. Then, all the three series below N=2 threshold of He$^+$ predicted by theory were observed. With the development of the synchrotron radiation technique, more sophisticated photoionization experiments were performed to achieve the higher Ryderg series above the N=2 [9], the decay paths of two-electron excitations [10], photoelectron angular distributions [11], threshold energies [12], interseries interferences [13], and the dipole-quadrupole interference [14], etc.

Rather than the above optical experiments (mostly by synchrotron radiation method), there were also lots of investigations on doubly excited states of helium by charged-particle (including electron, proton and other positive ion) impact method. Unlike the optical method, it is possible to observe both the optically allowed and forbidden transitions and so to reveal the full richness of the spectrum. Among these studies, the ejected electron spectroscopy was normally used [15]. Relatively few experiments used energy loss spectroscopy [16]. One can appeal the review by Schulz [17] for detailed information in this field. In the fast-electron impact and electron energy loss experiments, as early as in 1963, Silverman and Lassettre observed the double excitation $(2s2p)^1P$ and had some discussions of its strength depending on the momentum transfer from 0 to 1.0 a.u. [17]. Later, Wellenstein and collaborators [18] got the Bethe surface for helium by use of 25 keV incident electrons with the scattering angle from 0° to 10°. Although the low energy resolution (2 eV FWHM) precluded the authors from ruling out contributions from some of the optically forbidden transitions, Wellenstein et al alluded to the possible interest and significance in the momentum-transfer dependence of the Fano parameters in these doubly excited transitions. Using 2.5 keV incident energy with resolution of 0.7 eV FWHM, Fan and Leung [19] measured the generalized oscillator strength density (GOSD) and deconvolved the Fano parameters of $(2s2p)^1P^o \leftarrow (1s^2)^1S^e$ resonance. Compared with the present electron impact work by 2.5 keV incident energy and 80 meV FWHM resolution [20], although Fan and Leung's result is not accurate, it was the first time to give the momentum-transfer dependent behavior of Fano parameters of $(2s2p)^1P^o$ resonance.

Besides the experimental investigations, lots of theoretical works were carried out as a role to interpret, to predict, and to deeply understand the experimental results. The interference between a discrete state and a continuum around an autoionization state was illustrated theoretically by Fano and Cooper [3]. In Burke and McVicar's calculation [5], resonance states other than the normally known plus-minus series appeared. Sequentially, atomic theoreticians developed various theoretical methods to deal with doubly excited states of helium, including configuration-interaction (CI) methods, hyperspherical coordinate methods, close-coupling approximations, complex coordinate method, saddle-point technique and others [3-7].

In the above methods, most of these calculations presented the resonant energy positions, the resonant width, photoabsorption cross sections of these resonances, and very few gave the momentum transfer dependent behavior related parameters in the collision of charged particles with helium, such as the generalized oscillator strength (GOS), whose properties play the central role in the theory of collisions of fast charged particles with atoms and molecules. GOS can be written as [21]:

$$f(K,E)=\frac{2E}{K^2}\left|\left\langle \psi_f \left| \sum_{j=1}^{n} e^{e\vec{K}\cdot\vec{r}_j} \right| \psi_0 \right\rangle\right|^2 = \frac{E}{2}\frac{p_0}{p_a}K^2\frac{d\sigma(K,E)}{d\Omega}. \qquad (1)$$

For the case of fast electron impact, E is the excitation energy, p_0 and p_a are the momenta of the incident electron and scattered electron, respectively, K^2 is the momentum transfer square, ψ_i and ψ_f are the N-electron wavefunctions of the initial (ground) and the final state, respectively, and $\vec{r}_j$ is the position vector of the jth atomic electron. The above equation also gives the relationship between GOS and differential cross section (DCS, $d\sigma(K,E)/d\Omega$).

In Eq. (1), ψ_f is a discrete state. When the discrete state locates above the first ionization threshold, interference will occur between the discrete state and the corresponding continuum, which leads to the autoionization in the photoabsorption process. Fano worked out the configuration interaction theory for discrete-continuum interaction and introduced the famous Fano formula to describe the photoabsorption cross section (or the optical oscillator strength density spectrum, OOSD) around the resonance. Here we can generalize Fano's theory to the case of non-optical excitation, we write the GOSD near the resonances [3]:

$$\frac{df}{dE}=\sum_i f_{ai}\left(\frac{(q_i+\varepsilon_i)^2}{1+\varepsilon_i^2}-1\right)+f_c\,, \qquad (2)$$

here f_{ai} represents the relevant continuums involving interfere with the ith resonance, q_i represents the ratio of transition amplitude to the ‘‘modified’’ discrete state and to the unperturbed continuum states. $f_c(E)$ is the total continuum GOSD, which includes both parts that interfere and does not interfere with resonances, $\varepsilon_i=(E-E_{ri})/(\Gamma/2)$ stand for the departure of the excitation energy E from an idealized resonance energy E_{ri} which pertains to a discrete auto-ionizing level of the atom, this departure is expressed in a scale whose unit is the half-width $\Gamma/2$ of the line.

The ratio parameter ρ^2 is defined as:

$$\rho^2=\left.\frac{f_{ai}(K,E)}{f_c(K,E)}\right|_{E=E_{ri}}. \qquad (3)$$

For a specific resonance, the integrated GOS f_i of the ‘‘modified’’ embedded discrete state is expressed as [3]:

$$f_i=\left.\frac{\pi\Gamma_i}{2}f_{ai}q_i^2\right|_{E=E_{ri}}, \qquad (4)$$

since f_{ai} varies very slowly with E. Note that, for a window-type resonance, f_{ai} always is 0 because $q_i=0$, in spite of the degree of the interference between the discrete and the continuum. In order to elucidate the relevant strength involving interference between the embedded discrete state and the relevant continuum as a whole, an integrated resonance strength S_i can be defined as:

$$S_i=\frac{\pi\Gamma_i}{2}f_{ai}\big|_{E=E_{ri}}(q_i^2+1)\,. \qquad (5)$$

In present work, using the fast-electron energy loss spectrometer(EELS) [22,23], we measured the GOSDs for the doubly excited states of helium below the $N=2$ threshold of He$^+$ and obtained the parameters q_i and f_{ai} in Eq. (2). Both of the two parameters show the behaviour of momentum-transfer dependence, which indicate the dynamical electron correlation effect for the two highly excited electrons. And the parameters ρ^2, f_i and S_i are also calculated by Eq.(3-5).

2 EXPERIMENTAL METHODS

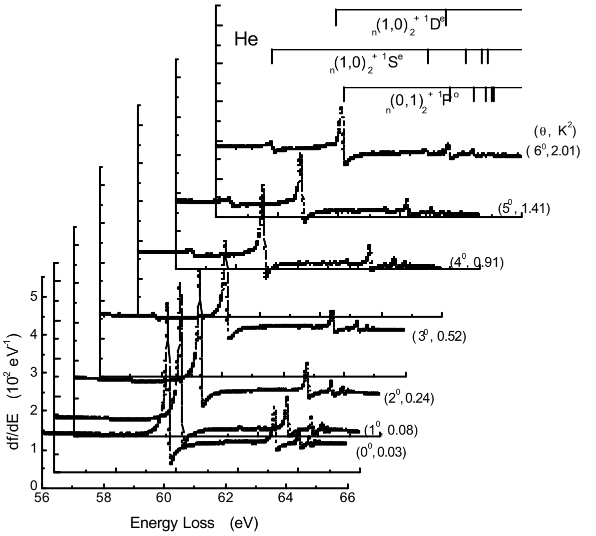

Fig. 1 The absolute GOSDs of the double excitations of helium from 0° to 6°.

Because the presently used high-resolution and angular-resolved fast-electron energy-loss spectrometer has been described in detail elsewhere [22,23], only a brief description is given here. The electrons are produced by a heated thorium-tungsten filament, after energy monochromized by an electrostatic hemispherical monochromator, they meet the target gases at the collision chamber. Then the scattered electrons are detected by a microchannel-plate based position sensitive detector (PSD) after they passed a rotatable electrostatic hemispherical analyzer. Compared with the previously used channeltron detector [22], the PSD gives a great increase in measurement efficiency for about 20 times [23], thus makes this investigation possible, especially at larger scattering angles and higher excited energies, where the differential cross sections are very small. The spectrometer was operated in the constant incident energy mode with incident energy at 2.5 keV, then energy loss caused by inelastic scattering was compensated by a scanning voltage with the step interval of 10 mV, and the energy resolution was 80 meV. In the present experiment, the background pressure in the collision chamber was 5×10^{-5} Pa, and the spectra were measured at the sample pressure of 8×10^{-3} Pa.

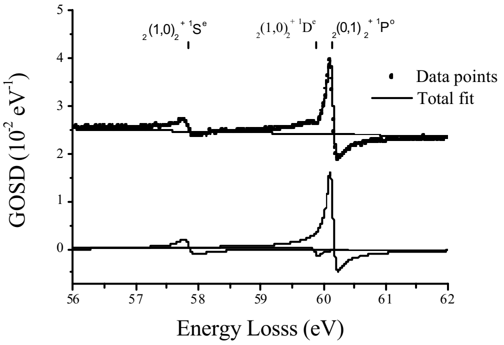

Fig. 2 The fitting result near the resonance of $_2\left(0,1\right)_2^{+}\,{}^1P^o$ at 6°

The spectra at scattering angles from 0° to 6° were recorded from 56 to 66 eV, which covers the $N=2$ doubly excited states of helium. The absolute energy scale is calibrated by the well-known resonance energy of $_2(0,1)_2^{+}\,{}^1P^o$, and the scattering angles were determined relating to the physical 0° which was calibrated by the symmetric angular distribution of the differential cross section for He 2^1P around 0°.

The normalization of the spectra was made by measuring the ratio of the intensity at θ to that at 4°. Then the spectra at non-0° were converted to the generalized oscillator strength densities (GOSDs), and the one at 0° was converted to the optical oscillator strength densities (OOSDs)[22]. The absolute GOSDs are illustrated in Fig.1. The assignments in Fig. 1 are adopted from the classification in Ref. [7]. In this classification, a doubly excited state ${}^{2S+1}L^{\pi}$ with one inner electron (principal quantum number N and one outer electron (principal quantum number n) can be represented as ${}_{n}(K,T)_{N}^{A}\,{}^{2S+1}L^{\pi}$, where K, T and A are new internal quantum numbers to describe the correlation between the two excited electrons [7].

After we measured the GOSD spectra, a numerical deconvolution procedure [24] based on least-squares fitting was used to obtained the parameters q_i and f_{ai} in Eq. (2). In order to show the reliability of the present fitting procedure, we give a illustration of the fitting result at 6° scattering angle in Fig. 2.

3 RESUTLS AND DISCUSSION

In Fig. 1, we show the GOSDs spectra measured by the present EELS method. It shows the momentum transfer K^2 dependence of the overall structures from 56 to 66 eV, which consist of series of Fano resonances. At scattering angle 0°, the momentum transfer is very small ($K^2 = 0.03$ a.u.), so this spectra can be taken as the OOSD spectra. As can be seen in Fig. 1, the Rydberg series of ${}_{n}(0,1)_{2}^{+}\,{}^{1}P^{o}$ have the dominative contributions to the total OOSD at 0°, and no other resonances show visible strength expect for two small fluctuations around 62.2 eV and 62.8 eV. When the scattering angle is increased, there are two dipole-forbidden series arise, i.e., ${}_{n}(1,0)_{2}^{+}\,{}^{1}S^{e}$ and ${}_{n}(1,0)_{2}^{+}\,{}^{1}D^{e}$, especially at large angles. The K^2 dependent behaviour of the three series are evidently different. Using a least-squares fitting program [24], we obtained the parameters in Eq. 1 at each scattering angle.

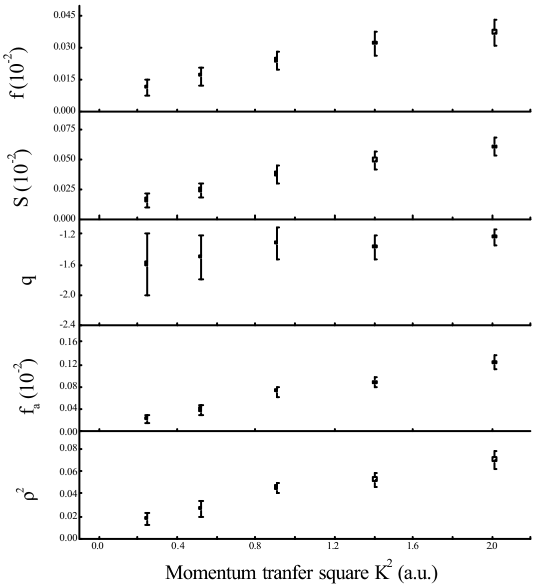

Fig. 3 The fitted Fano parameters of ${}_{2}(1,0)_{2}^{+}\,{}^{1}S^{e}$ as a function of K^2

The fitted Fano parameters of the ${}_{2}(1,0)_{2}^{+}\,{}^{1}S^{e}$ resonance are shown in Fig. 3. It can be seen that the $|q|$ varies a little and smoothly with K^2, it indicates that the transition amplitude into the ``modified" discrete state has a similar behavior as that into the relevant continuum with K^2. While the ρ^2, f and S of ${}_{2}(1,0)_{2}^{+}\,{}^{1}S^{e}$ increase with K^2, it shows the typical behaviors of dipole-forbidden transitions.

The fitted Fano parameters of the dipole-allowed ${}_{2}(0,1)_{2}^{+}\,{}^{1}P^{o}$ resonance are shown in Fig. 4. It can be seen that the sign of q is negative for all K^2, and $|q|$ decreases slowly with K^2. It indicates that the transition amplitude into the ``modified" discrete state decreases more quickly than that into the relevant continuum. As K^2 increases, the GOS f and the resonance strength S decrease, showing typical behaviors of dipole-allowed transitions. The ρ^2 decreases with K^2 because the contributions of dipole-forbidden transitions increase with K^2. It is interesting to note that in Fig. 4 there are discrepancies between ourfitted ρ^2 and those by Fan and Leung [19]. Their results

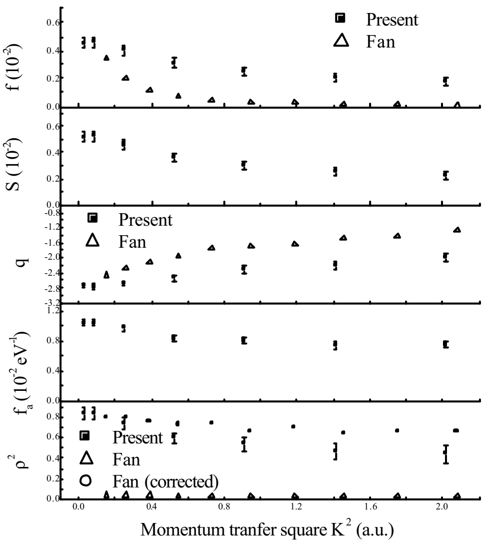

Fig. 4 The fitted Fano parameters of $_2(0,1)_2^{+}\,{}^1P^o$ as a function of K^2

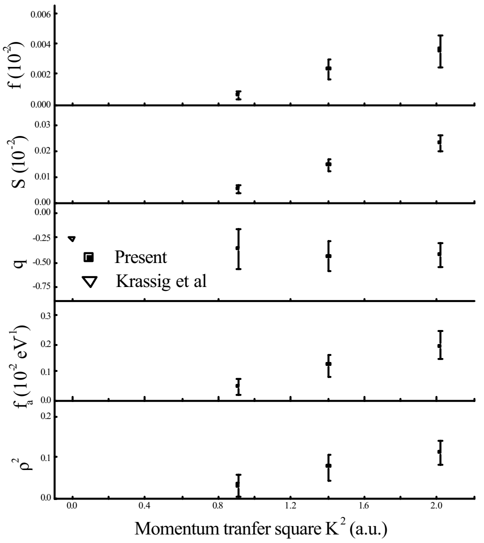

Fig. 5 The fitted Fano parameters of $_2(1,0)_2^{+}\,{}^1D^e$ as a function of K^2

were obtained by adopting for Γ their energy resolution of 0.7 eV directly. The importance of the energy convolution with the instrumental function can be understood by the energy folding integration with a Lorentzian function, i.e.

$$\int f_{ai}\left(\frac{\left(q_i+\frac{E-E_{ri}-E'}{\Gamma_i/2}\right)^2}{1+\left(\frac{E-E_{ri}-E'}{\Gamma_i/2}\right)^2}-1\right)\frac{2}{\pi\Omega}\frac{1}{1+\left(\frac{E'}{\Omega/2}\right)^2}dE'=\frac{f_{ai}\Gamma_i}{\Gamma_i+\Omega}\left(\frac{\left(q_i+\frac{E-E_{ri}}{(\Gamma_i+\Omega)/2}\right)^2}{1+\left(\frac{E-E_{ri}}{(\Gamma_i+\Omega)/2}\right)^2}-1\right)$$

(6)

here Ω is the Lorentzian width. Thus, the fitted f_{ai} without taking into account the convolution will be underestimated by a factor $(\Gamma_i+\Omega)/\Gamma_i$, about 20, the same for the corresponding ρ^2. We plot the corrected values in Fig. 4, which are then consistent with our fitted ρ^2. The values of q and f, reported in [19] with the energy resolution about 0.7 eV insufficient to observe the nearby resonances are generally smaller than ours especially at large K^2. Such experimental discrepancies require further studies.

The fitted Fano parameters of the $_2(1,0)_2^{+}\,{}^1D^e$ resonance are displayed in Fig. 5. The sign of presently experimental q is negative and $|q|$ varies very slowly with K^2 with a value 0.37±0.18, which is consistent with the experimental electric dipole-quadrupole interference value of -0.25 [14]. Note though that Krassig *et al.* [14] said that ``the value of q can not be unambiguously determined from electron scattering experiments because all multipoles are present''. It seems that at present incident energy of 2.5 keV, the other multipoles contribute much less to the excitations. The f, S, f_a and ρ^2 of $_2(1,0)_2^{+}\,{}^1D^e$ increase with K^2, showing typical behaviors of quadrupole transitions.

In order to show the high resolution spectra near the $_2(0,1)_2^{+}\,{}^1P^o$ and $_3(0,1)_2^{+}\,{}^1P^o$ resonances, after removing the ``smooth ionization continuum'' (i.e., $f_c(E)$ in Eq. (1)), the GOSDs at 0°, 2°, 4° and 6° are displayed in Fig. 6. It clearly reveals the weak resonances ($_{2,3}(1,0)_2^{+}\,{}^1S^e$, $_{2,3}(1,0)_2^{+}\,{}^1D^e$, $_2(-1,0)_2^{+}\,{}^1S^e$ and $_3(1,0)_2^{-}\,{}^1P^o$). As K^2 increases, the dipole-forbidden transitions $_{2,3}(1,0)_2^{+}\,{}^1S^e$ and $_{2,3}(1,0)_2^{+}\,{}^1D^e$ arise higher, while $_2(-1,0)_2^{+}\,{}^1S^e$ has relatively slower variation with K^2. And it is obvious that the strength of the dipole-allowed transition $_3(1,0)_2^{-}\,{}^1P^o$ decreases slowly with K^2. The above

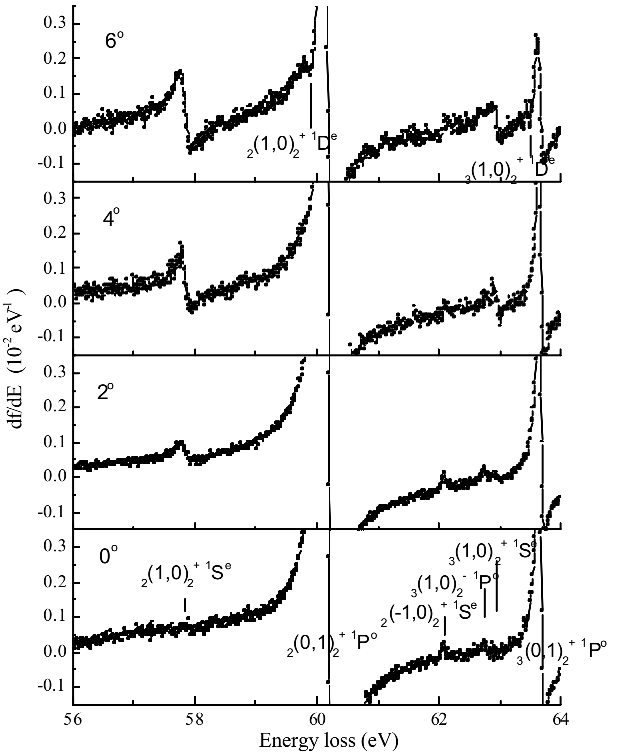

Fig. 6 The GOSDs of double excitations of helium at 0°, 2°, 4° and 6° with smooth ionization continuum removed.

momentum-transfer dependent behaviour is the typical characteristic for the dipole-allowed and dipole-forbidden transitions.

Let us focus on the two weak resonances $_2(-1,0)_2^{+\,1}S^e$ and $_2(1,0)_2^{+\,1}S^e$ in Fig. 6 to elucidate excitation dynamics according to the internal correlation quantum numbers, K, T and A. We pay attention to the K^2 dependence of these two resonances. Based on Fermi's Golden rule, the transition strength is proportional to the square of the transition matrix element, i.e., the transition-operator-weighted overlap integral between the initial ground state $(1s)^2\,{}^1S^e$ and the final doubly excited state $_2(K,T)_2^{+\,1}S^e$. At large angles (e.g., $\theta \sim 4^\circ$ with $K^2 \sim 0.91$ a.u.), the transition matrix element results mainly from the interactions in an inner region (e.g., $R=\sqrt{r_1^2+r_2^2} \leq 1$ a.u.). At small angles (e.g., $\theta \sim 0^\circ$ with $K^2 \sim 0.03$ a.u.), the transition matrix element results mainly from the interactions in an outer region (e.g., $R \geq 5$ a.u.). For the initial ground state, the wave function, in the inner region, has a broad peak at ($\theta_{12} = 180^\circ$, $\alpha = \tan^{-1}(r_1/r_2) = 45^\circ$) while it, in the outer region, has two ridges at (θ_{12} from 0° to 180°, $\alpha \sim 20^\circ$ and 70°) respectively owing to the two electron ``breathing'' correlations in the hyperspherical coordinate [7]. In both inner and outer regions with respect to the initial ground state (i.e., $R \leq$ about 7 a.u. because negligible contribution to the overlap integral owing to exponential decay of the ground state wave function), the wave function of $_2(1,0)_2^{+\,1}S^e$ has a broad peak at ($\theta_{12} = 180^\circ$, $\alpha = 45^\circ$), while that of $_2(-1,0)_2^{+\,1}S^e$ has one major broad peak at ($\theta_{12} = 30^\circ$, $\alpha = 45^\circ$) and two minor rising ridges at (θ_{12} from 0° to 180°, $\alpha \sim$ 20° and 70° with two peaks at $\theta_{12} = 180^\circ$) respectively [7]. Thus, the strength variation of the transition $_2(-1,0)_2^{+\,1}S^e$ with K^2 should be slow because the wave functions of $(1s)^2\,{}^1S^e$ and $_2(-1,0)_2^{+\,1}S^e$ has a definite overlap in spite of K^2. In contrast, the strength variation of the transition $_2(1,0)_2^{+\,1}S^e$ with K^2 should be fast because the wave functions of $(1s)^2\,{}^1S^e$ and $_2(1,0)_2^{+\,1}S^e$ has a very different overlap according to different K^2. This momentum-transfer dependence can be seen from Fig. 6. However, it is strange that the transition $_2(-1,0)_2^{+\,1}S^e$ has an exorbitant strength even at $K^2 \sim 0.03$ a.u.. Furthermore, the width ($\Gamma_{1,0} \sim V_{1,0}^2$) of $_2(1,0)_2^{+\,1}S^e$ is lager than the width ($\Gamma_{-1,0} \sim V_{-1,0}^2$) of $_2(-1,0)_2^{+\,1}S^e$. This can be understood as follows: Because of $_2(1,0)_2^{+\,1}S^e$ with the major configuration as $(2s)^2$ and $_2(-1,0)_2^{+\,1}S^e$ with the major configuration as $(2p)^2$, the squared interaction matrix element ($V_{1,0}^2 \sim R^0(2s,2s;1s,\varepsilon s)^2$) should be lager than the squared interaction matrix element ($V_{-1,0}^2 \sim R^1(2p,2p;1s,\varepsilon s)^2$), where $R^l(2l, 2l; 1s, \varepsilon s)$ are Slater integrals. Fig. 6 also exhibits the well known phenomena that the resonance ${}_3(0,1)_2^{+1}P^o$ with $A=1$ is much stronger than the resonance ${}_3(1,0)_2^{-1}P^o$ with $A=-1$.

[1] Madden R. P. and Codling K., Phys. Rev. Lett. **10**, 516(1963).

[2] Cooper J. W., Fano U. and Prats F., Phys. Rev. Lett. **10**, 518(1963).

[3] Fano O., Phys. Rev. 124, 1866(1961); Fano U. and Cooper J. W., Phys. Rev. **127**, A1364(1965).

[4] Tanner G., Richter K. and Rost J. M., Rev. Mod. Phys. 72, 497(2000).

[5] Burke P. G. and McVicar D. D., Proc. Phys. Soc., London 86, 989(1965).

[6] Chung K. T. and Chen I. H., Phys. Rev. Lett. 28, 783(1972).

[7] Lin C. D., Phys. Rev. A 47, 1019(1984); Phys. Rev. A 25, 76(1982).

[8] Domke M., Remmers G. and Kaindl G., Phys. Rev. Lett. 69, 1171(1992).

[9] Domke M., Schulz K., Remmers G., Kaindl G. and Wintgen D., Phys. Rev. A 53, 1424(1996) and the references therein.

[10] Odling-Smee M. K., Sokell E., Hammond P. and MacDonald M. A., Phys. Rev. Lett. 84, 2598(2000) and the references therein.

[11] Menzel A., Frigo S. P., Whitfield S. B., Caldwell C. D. and Krause M. O., Phys. Rev. A 54, 2080(1996).

[12] Thompson D. B., Bolognesi P., Coreno M., Camilloni R., Avaldi L. Prince K. C., de Simone M., Karvonen J. and King G. C., J. Phy. B: At. Mol. Opt. Phys. 31, 2225(1998).

[13] Puttner R., Domke M., Gremaud B., Martins M., Schlachter A. S. and Kaindl G., J. Elect. Spect. Rel. Phen. 101-103, 27(1999).

[14] Krassig B., Kanter E. P., Southworth S. H., Guillemin R., Hemmers O., Lindle D. W., Wehlitz R. and Martin N. L. S., Phys. Rev. Lett. 88, 203002(2002).

[15] Moretto-Capelle P., Bordenave-Montesquieu, Bordenave-Montesquieu A., Godunov A. L. and Schipakov V. A., Phys. Rev. Lett. 79, 5230(1997) and the references therein.

[16] Htwe W. T., Vajnai T., Barnhart M., Gaus A. D. and Schulz M., Phys. Rev.Lett. 75, 1348(1994); Schulz M, Inter. J. Mod. Phys. B9,3269(1995).

[17] Silverman S. M. and Lassettre E. N., J. Chem. Phys. 40,1265(1963).

[18] Wellenstein H. F., Bonham R. A. and Ulsh R. C., Phys. Rev. A8, 304(1973).

[19] Fan X. W. and Leung K. T., J. Phys. B 34, 811(2001).

[20] Liu X. J., Zhu L. F., Yuan Z. S., Li W. B., Cheng H. D., Huang Y. P., Zhong Z. P., Xu K. Z. and Li J. M., Phys. Rev. Lett. 91, 193203(2003).

[21] Inokuti M., Rev. Mod. Phys. 43, 297(1971).

[22] Xu K. Z., Feng R. F., Wu S. L., Ji Q., Zhang X. J., Zhong Z. P. and Zheng Y., Phys. Rev. A53,3081(1996).

[23] Liu X. J., Zhu L. F., Jiang X. M., Yuan Z. S., Cai. B., Chen X. J. and Xu K. Z., Rev. Sci. Instrum. 72, 3557(2001).

[24] Liu X. J., Huang Y. P., Zhu L. F., Yuan Z. S., Li W. B. and Xu K. Z., Nucl. Instrum. Nucl. Instrum. Meth. A 508, 448(2003.)

Dielectronic recombination in Highly charged ion-electron collision

X. Ma[1], P. Mokler[2]

1 Institute of Modern Physics, Chinese Academy of Sciences, Lanzhou 730000, China
2 Gesellschaft für Schwerionenforschung mbH, Darmstadt, D-64291, Germany

In recent years, dielectronic recombination (DR) processes have been studied intensively for heavy ion-electron collisions due to the advent of cooler storage rings. On these novel devices recombination experiments between ions selected charge state and cold electrons are performed with very high energy resolution [1,2]. Most studies of DR were focused on medium heavy ions and lithium-, sodium-like ions, and resonant energy spectra were measured, no x-ray spectra have been measured due to experimental setup environment. At EBIT devices, x-ray spectra were recorded for DR-cascade processes but no angular distributions were studied. In this paper we report the KLL-DR processes for collisions between H-like uranium ions and quasi-free electron target. In this process doubly excited He-like ions with two K-vacancies were formed, the cascade two characteristic K x-rays, namely the hyper-satellite and the satellite Kα-lines, were detected with germanium detectors at various angles. The measured angular distributions of the cascade x-rays were compared with fully relativistic theories [3,4]. Strong alignment was found for the hyper-satellite radiation in the KLL resonance.

[1] C. Brandau, T. Bartsch, K. Beckert, et al., Nucl. Instr. Meth. B205 pp66-69 (2003).
[2] G. Gwinner, D. W. Savin, D. Schwalm, et al., Physica Scripta T92 pp319-321 (2001)
[3] X. Ma, P. H. Mokler, F. Bosch, et. al., Phys. Rev. A68: 042712-1 (2003)
[4] S. Zakowicz, Z. Harman, N. Gruen, W. Scheid, Phys. Rev. A68: 042711 (2003)

Atomic Processes in Ultra-Short Pulse Laser Interaction

Richard M. More, H. Yoneda(*), H. Morikami(*)
National Institute for Fusion Science, Toki, Gifu, Japan T 503-5292
(*) University of Electro-communication, Chofu, Japan T 182-8585

Ultra-short pulse laser absorption experiments can measure the behavior of matter in the transition region between solid and plasma. These measurements provide a new type of experimental data and may reveal unexpected physical phenomena such as new phases or new states of organization of matter. Naturally, we attempt to interpret the experiments by combining ideas from plasma physics and solid-state physics. For the most interesting materials, such simple interpretation does not succeed and new ideas are needed.

Recent experiments on gold targets show a remarkable time-variation of the optical properties of the target material. We believe this variation is a consequence of ionization and recombination. We develop a practical model for the effect of recombination on the dielectric function, and combine this with hydrodynamic simulation of the gold plasma expansion and solution of Maxwell equations for the laser-plasma interaction.

The experiments have given evidence for two novel and remarkable phenomena: dramatically inhibited conductivity of free electrons, probably due to a localization phenomenon, and creation of an anomalous electronegative plasma containing both positive and negative ions of gold.

Generalized oscillator strengths of nitric oxide for the valence shell excitations

Yasuhiro Sakai
Dept. of Physics, Toho University 2-2-1 Miyama, Funabashi, Chiba, 274-8510 Japan

The generalized oscillator strength (GOS) is a fundamental quantity of atoms and molecules and related to other important physical constants. In order to study perfectly the atomic and molecular processes in plasma, it is necessary to understand the behavior of GOS for various transitions of atoms and molecules. There are many works reported about the GOS, which had been carried out from 1960's to 1970's. In particular, Lassettre et.al. showed remarkable results.[1] Recently, a group of Xu in USTC works vigorously and new results are made one after another.[2] By our group, the GOS's of some rare gas atoms have been measured.[3] Since the electron spectrometer used by us is rotatable around the collision center from –5 to 110 deg and it is possible to use the impact energies from about 100 to 500 eV, we can get the GOS from near the squared momentum transfer K^2 equals zero to higher side of K^2. On the other hand, the impact energy of the electron spectrometer of Xu's group can be varied from 1 to 5 keV and small scattering electron signal can be detected. So we started the collaborating projects about the GOS behavior and the optical oscillator strength (OOS) value as a limited ones at $K^2 = 0$, from 2001 by one of the project of the JSPS-CAS Core-University Program. In this time, I pick up a topic for the behavior of GOS of nitric oxide for the valence shell excitations. Nitric oxide is a simple diatomic molecule, which has the valence shell of $(2\pi)^1$ in the grand $X^2\Pi$ state. The determined GOS's from the electron energy-loss spectra are for the transition of $\gamma(X \rightarrow A^2\Sigma^+)$, $\delta(C^2\Pi)$, and $\varepsilon(D^2\Sigma^+)$ bands except for $\beta(B^2\Pi)$. The GOS curves for only γ band have a peak at $K^2 \sim 0.2$. This behavior is similar to that of $CO(X^1\Sigma^+ \rightarrow B^1\Sigma^+)$ and $N_2(X^1\Sigma_g^+ \rightarrow B^1\Sigma_g^+)$ transitions. What is same and what is different? These experiments and projects are still in progress.

[1] For example, K.N.Klump and E.N.Lassettre, J.Chem. Phys., **53**, 3806(1970).
[2] For example, K.Z.Xu et.al., Phys.Rev.A, **53**, 3081(1996).
[3] For example, T.Y.Suzuki et.al., Phys.Rev.A, 57, 1832(1998).

China-Japan Symposium on Atomic and Molecular Processes in Plasma (AMPP)

March 6 - 11, 2004
Northwest Normal University, Lanzhou, China

The symposium is one of the activities of NSFC-JSPS Scientific Cooperation Program entitled "Atomic and molecular processes in plasma". The symposium is organized for discussions on the atomic and molecular processes related to the plasma physics and also on the plasma analysis in close relation to the atomic and molecular physics.

Scope of the Symposium:

In the nuclear fusion plasma, there are quite a variety of atomic processes such as ionization, excitation, radiative recombination, non-radiative recombination (di-electronic recombination, collisional electron transfer), cascade radiation, and cascade Auger decay over the wide range of plasma temperature. The knowledge of such processes is indispensable for the evaluation and improvement of the plasma properties. And, to determine the profile of reactor core plasmas, we need to know the abundance of the impurity ions, the ionicity of multiply charged ions doped in high temperature plasmas, radiation transfer, and opacity against the radiation. Furthermore, we may consider the usage of atomic processes in plasma as the tool of plasma diagnostics. We may use, for example, the X-ray spectroscopic measurement of the spectator satellite lines and/or participator satellite lines of the multiply charged ions to gain the various plasma properties. To accomplish such subjects, we need elaborate evaluation of the probe device atoms, and also need extensive study to obtain high precision atomic structure data, which are desirable to be carried out by international collaboration groups.

The aim of the joint symposium is for variety of researchers working in atomic and molecular processes in plasmas to get together, and to exchange the recent progress of the research activities. The joint symposium is also been expected extensive discussions about the view of the future cooperation activities between the both countries.

The symposium will include the following subjects for discussion:

1. Spectroscopic properties of ions and atoms in plasma
2. Collisions of electronic and atomic ions in plasma
3. Analysis and diagnostics of the confinement plasma
4. Atomic data compilation and database construction
5. Molecular processes in confinement plasma

Scientific Sessions and Publication of the Proceedings

1. All the participants who give a contribution are arranged an oral presentation for about 40 minutes; 30 minutes will be for talk, and 5-10 minutes for discussion.
2. For presentations, the screen display system that may be connected by a mobile PC with Windows XP, Windows 2000/98 is available. A Windows-based PC with Acrobat Reader and PowerPoint 2000 is also available. The Microsoft Power Point files can be used for presentations. The users are requested to supply them by floppy discs, CD-ROMs, or USB memory sticks. The conventional Over Head Projector (OHP) is available.
3. The contributions to this symposium will be published as one of the issues in the NIFS report series. The details of the instruction for the submission will be announced at the conference.

Symposium Site

Situated near China's geographic center, Lanzhou is the capital of Gansu Province and a regional communications and transportation hub. The city has a population of around 2,270,000. The geography has shaped the city into a narrow stripe along the southern banks of the Yellow River. Lanzhou is also an important stopover in the ancient Silk Road, which stretches 1,600 km from eastern Gansu westward through the province. The Mogao Grottoes in Dunhuang, renowned as the art treasure house of the East, is located 1200 km west from Lanzhou. For more details of Lanzhou, please refer to http://www.travelchinaguide.com/cityguides/gansu/lanzhou/. And, for details of Mogao Grottoes, please refer to http://www.travelchinaguide.com/attraction/gansu/dunhuang/.

The symposium will be held at the Academic Report Hall in the Physics Building of Northwest Normal University. On the available equipments for presentation, see the entry “Scientific Sessions and Publication of the Proceedings” above.

Accommodations

Lanzhou Friendship Hotel (see http://www.sinohotelguide.com/lanzhou/friendship for details) is selected for symposium participants and their families. The Lanzhou Friendship Hotel (Lanzhou youyi binguan) is located in the western end of the town at the bank of the Yellow River, and just near to the western railway station. The distance from the Lanzhou airport is about 60 km. The hotel is 20 minutes away from the Northwest Normal University by bus. The cost of the hotel is expected to be 240 RMB per night for single room with 2 beds. Current exchange rates are approximately 1 Chinese Yuan = 12.83 Japanese Yen. The hotel accepts the visa credit card. And the hotel can cash the Japanese currency.

The address of the hotel is

Address: 16, Xijin Xi Road, Lanzhou
Postal Code: 730050
Tel: 0086-931-2333051

Below is for the hotel's Chinese address and telephone number. This image may help you to return to the hotel from any place in Lanzhou.

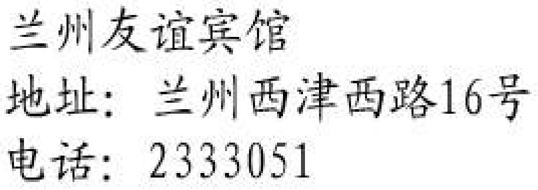

兰州友谊宾馆
地址：兰州西津西路16号
电话：2333051

The local organizers will meet the participants at the airport. All the attendees arriving at Lanzhou airport in the afternoon on March 6 are advised to find out a person who shows the sign “China-Japan Joint Symposium on Atomic and Molecular Processes in Plasmas” after passing through the exit gate, which is unique at the airport. He (or she) will guide you to a bus to the Friendship Hotel. For the convenience of the arrangement, all the attendees are encouraged to inform their arrival date, time, and the flight number to dongcz@nwnu.edu.cn in well advance.

Conference Outing

We will have a one day trip to Ta'er Monastery (Kumbum Monastery) on March 10. Ta'er Monastery is one of the six biggest monasteries of the Yellow Hat Sect (Gelugpa Sect) of Tibetan Buddhism (http://www.travelchinaguide.com/attraction/qinghai/xining/taer_monastery.htm). It is located about 30 kilometers southwest of Xining city, the capital of Qinhai Province, the neighborhood of Gansu.

We also have a short round trip in Lanzhou city in the afternoon of March 11. The details will be announced at the symposium.

Symposium Fees and Supports

The major part of the symposium cost is supported by NSFC and JSPS, and also by Northwest Normal University. The participants will be charged a small symposium fee of about 2000 Yuan RMB, which includes the fee of all the conference meals, two formal banquets, and the outing.

Advisory Committee

Takako Kato, National Institute for Fusion Science, Japan
F. Koike, Kitasato University, Japan
A. Ichimura, Institute of Space and Astroneutical Science, Japan
Li Jiaming, Tsinghua University, China
Wan Baonian, Institute of Plasma Physics, Chinese Academy of Science, China
Dong Chenzhong, Northwest Normal University, China

Local Committee

Wang Liming, Northwest Normal University
Deng Hualin, Northwest Normal University
Dong Chenzhong, Northwest Normal University
Zhou Xiaoxin, Northwest Normal University
Ma Xinwen, Institute of Modern Physics, Chinese Academy of Science
Zhang Youming, Northwest Normal University
Li Yongxiang, Northwest Normal University

Contact:

Prof. Dong Chenzhong
Email: dongcz@nwnu.edu.cn
Phone: +86-931-7972416, 7971503
Fax: +86-931-7971277
Mail: Northwest Normal University,
Anning East Road 805, Anning, Lanzhou
730070 China

Dr. Fumihiro Koike
Email: koikef@kitasato-u.ac.jp
Phone: +81-(0) 42-778-9225, 8029
Fax: +81-(0) 42-778-8441
Mail: Kitasato University,
Kitasato 1-15-1 Sagamihara
228-8555 Japan

Scientific Program

Saturday, March 6: Welcome

08:30 – 18:00 Arrival and Registration

18:00 – 19:30 Welcome Reception

Sunday, March 7: Sessions 1 - 4

07:00 – 08:10 Breakfast

08:10 – 08:30 Move to NWNU

08:30 – 09:10 Opening Remarks (Chair: T. Kato)

i. T. Kato, NIFS
ii. Deng Hualin, Vice-President of NWNU
iii. Li Jiaming, Academician of Chinese Academy of Sciences, Tsinghua University
iv. Take a photo of all the participants

9:20 – 10:40 Session 1 (Chair: F. Koike)

1. Relativistic calculations for multiple and highly charged ions
   S. Fritzsche, Kassel University
2. Energy－crossing and its effects on spectra of the neon-like ions,
   Dong Chenzhong , Northwest Normal University

10:40 – 11:00 Coffee break

11:00－12:20 Session 2 (Chair: S. Fritzsche)

3. The need of precise atomic structure calculations for the study of plasma processes
   F. Koike, Kitasato University
4. Relativistic multi-channel treatment of radiative transition process
   Qu Yizhi, Graduate School of the Chinese Academy of Sciences, Beijing

12:20 – 14:10 Lunch Break

14:10 – 14:30 Move to NWNU

14:30 – 16:30 Session 3 (Chair: R. More)

5. Impurity emissions measured from Large Helical Device
   T. Kato, NIFS
6. Influence of the detailed line treatment on the calculated opacity of hot plasmas
   Yuan Jianming, National University of Defense Technology, Changsha
7. Plasma spectroscopy of hydrogen ice pellets in the Large Helical Device
   M. Goto, NIFS

16:30 – 16:50 Coffee break

16:50 – 18:10 Session 4 (Chair: Wang Jianguo)

8. Formation Mechanism and Emission Spectrum of AlO Radicals in Reaction of Laser-ablated Al atom and Oxygen.
   Zhang Shudong, Northwest Normal University
9. Excited hydrogen atom formed by non-adiabatic electron transfer from metal surfaces
   D. Kato, NIFS

18:10 – 20:00 Conference Banquet by NWNU

Monday, March 8: Session 5 - 8

07:00 – 08:10 Breakfast

08:10 – 08:30 Move to NWNU

08:30 – 10:30 Session 5 (Chair: H. Takagi)

10. Spectroscopic Study of Ions transmitted from Microcapillary Tube
    Y. Kanai, Riken
11. Electron Transfer and Decay Processes of Highly Charged Iodine Ions
    H. Sakaue, NIFS
12. Spectroscopic study of charge transfer in collisions of multicharged ions
    H. Tanuma, Tokyo Metropolitan University

10:30 – 10:50 Coffee break

10:50 – 12:10 Session 6 (Chair: M. Takahashi)

13. Elastic and inelastic processes in H^++CH_2 collisions below the 1.5-keV regime
    H. Suno, Yamaguchi University
14. Theoretical Study of Vibrationally Selective Charge Transfer Cross Section
    Wang Jianguo, Institute of Applied Physics and Computational Mathematics, Beijing

12:10 – 14:10 Lunch Break

14:10 – 14:30 Move to NWNU

14:30 – 16:30 Session 7 (Chair: Yuan Jianming)

15. Dielectronic recombination in highly charged heavy ion-electron collision
    Ma Xinwen, Institute if Modern Physics, Chinese Academy of Sciences, Lanzhou
16. Recent progress of atomic & molecular database
    Yan Jun, Institute of Applied Physics and Computational Mathematics, Beijing
17. Polarization Plasma Spectroscopy
    A. Iwamae, Kyoto University

17:10 – 20:00 Going out for dinner with local dishes

20:00 – 22:00 Enjoy the dance drama “The Silk Road dotted with flower”

Tuesday, March 9: Session 8 – 11

07:00 – 8:10 Breakfast

08:10 – 08:30 Move to NWNU

08:30 – 10:30 Session 8 (Chair: A. Ichimura)

18. Improved density functional calculations for atoms and small molecules
    Burkhard Fricke, Kassel University
19. Electronic structure of atoms in laser plasma: the Debye shielding model
    T. Sako, Tokyo University
20. Superexcited states studied by angle-resolved electron energy loss spectroscopy
    Zhong Zhiping, Graduate School of the Chinese Academy of Sciences

10:30 – 10:50 Coffee break

10:50 – 12:10 Session 9 (Chair: Ma Xinwen)

21. (e,2e) ionization-excitation experiments with randomly oriented and fixed-in-space H2 molecules
M. Takahashi, Institute for Molecular Science

22. Electron and molecular ion collisions relevant to divertor plasma.
H. Takagi, Kitasato University

12:10 – 14:10 Lunch Break

14:10 – 14:30 Move to NWNU

14:30 – 16:30 Session 10 (Chair: B. Fricke)

23. Atomic Processes in Ultra-Short Pulse Laser Interaction
R. More, NIFS

24. Above-threshold ionization spectrum of a model Atom in Intense Laser Field
Zhou Xiaoxin, Northwest Normal University

25. Multiple ionization dynamics of molecules in intense laser fields.
A. Ichimura, and T. Yamaguchi, ISAS, and Tokyo Metropolitan College of Technology

16:30 – 16:50 Coffee break

16:50 – 18:50 Session 11 (Chair: Yan Jun)

26. Geometry Effects on the (e,2e) Cross Sections of Ionic Targets
Y. Khajuria, Institute for Molecular Science

27. The momentum transfer dependence of double excitations of helium
Zhu Linfan, University of Science and Technology of China, Hefei

28. Generalized Oscillator strengths of nitric oxide for the valence shell excitations
Y. Sakai, Toho University

18:50 – 20:00 Conference Banquet by the Organizing Committee of the Symposium

Wednesday, March 10

Conference Tourism

Thursday , March 11: Session 12
14:30 – 16:30 Sightseeing tour through the city of Lanzhou
16:30 – 18:30 Visiting the museum of the NWNU
18:30-18:40 Session 12: Closing Remarks

i. F. Koike, Kitasato University
ii. Dong Chenzhong, Northwest Normal University

18:40 – 20:00 Dinner
Adjourn

List of Participants

Name	Affiliation	e-mail address
Goto, Motoshi	National Institute for Fusion Science	goto@LHD.nifs.ac.jp
Burkhard Fricke	Kassel University, Kassel, Germany	fricke@physik.uni-kassel.de
Dong Chenzhong	Northwest Normal University, Lanzhou	dongcz@nwnu.edu.cn
Ichimura, Atsushi	Institute for Space and Aeroneutical Science	ichimura@pub.isas.ac.jp
Iwamae, Atsushi	Kyoto University	iwamae@kues.kyoto-u.ac.jp
Kanai, Yasuyuki	RIKEN	kanai@rarfaxp.riken.go.jp
Kato, Daiji	National Institute for Fusion Science	dkato@nifs.ac.jp
Kato, Takako	National Institute for Fusion Science	takako@nifs.ac.jp
Khajuria, Yugal	Institute for Molecular Science	khajuria@ims.ac.jp
Koike, Fumihiro	Kitasato University	koikef@kitasato-u.ac.jp
Li Jiaming	Academician of Chinese Academy of Sciences, Tsinghua University, Beijing	jmli@cams.tsinghua.edu.cn
Ma Xinwen	Institute of Modern Physics, Chinese Academy of Sciences, Lanzhou	x.ma@impcas.ac.cn
More, Richard	National Institute for Fusion Science	more@nifs.ac.jp
Qu Yizhi	Graduate School of the Chinese Academy of Sciences, Beijing	yzqu@gscas.ac.cn
Sakai, Yasuhiro	Toho University	sakai@ph.sci.toho-u.ac.jp
Sakaue, Hiroyuki	National Institute for Fusion Science	sakaue@nifs.ac.jp
Sakou, Tokuei	Tokyo University	sako@chem.s.u-tokyo.ac.jp
Stephan Fritzsche	Kassel University, Kassel, Germany	s.fritzsche@physik.uni-kassel.de
Suno, Hiroya	Yamaguchi University	suno@yamaguchi-u.ac.jp
Takagi, Hidekazu	Kitasato University	takagi@kitasato-u.ac.jp
Takahashi, Masahiko	Institute for Molecular Science	masahiko@ims.ac.jp
Tanuma, Hajime	Tokyo Metropolitan University	tanuma@phys.metro-u.ac.jp
Wang Jianguo	Institute of Applied Physics and Computational Mathematics, Beijing	wang_jianguo@mail.iapcm.ac.cn
Yamaguti, Tomoko	Tokyo Metropolitan College of Technology	yamaguti@tokyo-tmct.ac.jp
Yan Jun	Institute of Applied Physics and Computational Mathematics, Beijing	yan_jun@mail.iapcm.ac.cn
Yuan, Jianming	National University of Defense Technology, Changsha	

Zhang Shudong	Northwest Normal University, Lanzhou	zhangsd@nwnu.edu.cn
Zhong Zhiping	Graduate School of the Chinese Academy of Sciences	zpzhong@gscas.ac.cn
Zhou Xiaoxin	Northwest Normal University, Lanzhou	zhouxx@nwnu.edu.cn
Zhu Linfan	University of Science and Technology of China, Hefei	lfzhu@ustc.edu.cn